DOCTOR OF PHILOSOPHY IN PHOTONICS

THE INSTITUTE OF PHOTONIC SCIENCES

Discerning between thermal and electronic effects in plasmon-enhanced organic reactions

Ivan Bordacchini

Ph.D. dissertation

Advisor: Prof. Dr. Romain Quidant

July 2020

Abstract

Since the pioneering work of Fujishima and Honda on titanium dioxide, TiO_2, for the electrochemical photolysis of water under ultraviolet (UV) irradiation, semiconductor-based photocatalysis and photovoltaics have become a rapidly growing field of investigation. However, UV light accounts for only 4% of the solar spectrum, whereas the visible light represents 42% of the total solar radiation. Therefore, the scientific community focused their efforts on the optimization and extension of the absorption spectrum of semiconductor-based materials to the visible region of the solar spectrum. Well-established techniques include doping of the semiconductor or the deposition of a different element or substance on the surface of the material.

Since 2004, the deposition of plasmonic nanoparticles (NPs) on semiconductors emerged as a possible solution to generate energetic electrons capable of driving reactions under visible irradiation. Since then, numerous contributions have been published in the field of plasmon-enhanced photocatalysis with relevant applications in water splitting, organic synthesis, and photovoltaics.

In the field of heterogeneous photocatalysis, plasmon-generated energetic electrons were widely accepted as responsible for the observed catalytic effect of plasmonic NPs. Recently, several scientific contributions have questioned the actual mechanism triggering plasmon-enhanced reactions, hypothesising that thermal effects are instead the predominant factor that influences the activity of a plasmonic catalyst.

In this work, we aimed at differentiating between the thermal and electronic effects of plasmonic NPs in a test reaction—the reductive

coupling of nitrobenzene to azobenzene—under irradiation with 532 nm and/or 875 nm lasers. Moreover, we also aimed at developing a methodology that could be easily replicated in other laboratories and used as a benchmark test for plasmon-enhanced reactions run in solution.

We optimized the size and shape of AuNPs plasmonic catalysts to obtain materials with different absorption in the visible and near-infrared (NIR) region to tune the electronic and thermal effects of the catalyst. The activity of the synthesised catalysts for the test reaction was compared with the activity of the Gold World Council reference catalyst type A.

Characterization of the synthesised Au/TiO_2 catalyst with diffuse reflectance measurements evidenced that the presence of small amounts of AuNPs did not modify the band gap position of the support, hence suggesting that, under visible light irradiation, the catalysis occurred on the surface of the AuNPs. The determination of the enthalpy of activation for each step of the reaction showed that the second step of the reaction was strongly influenced by the 532 nm laser irradiation. Indeed, our calculations demonstrated an energy difference between the illuminated and the dark reactions in the first step of reaction of $1.1\ Kcal\ mol^{-1}$ whereas the one for the second step was $5.9\ Kcal\ mol^{-1}$.

We further analysed the results of designed experiments running the test reaction in the presence of two catalysts differing by the shapes of the AuNPs and under different laser sources and irradiances. The results were processed to obtain predictive phenomenological models for the intermediate and the product of the reaction, azoxybenzene and azobenzene, respectively.

The obtained models allowed to confirm that the investigated reaction was triggered by electronic effects and that the contribution of thermal effects, generated by the electron-phonon decay of elongated AuNPs, was not significantly influencing the reaction outcome.

Resumen

A partir del trabajo pionerito de Fujishima y Honda sobre el dióxido de titanio, TiO_2, para la fotólisis electroquímica de agua bajo irradiación ultravioleta (UV), la fotocatálisis basada en semiconductores y la energía fotovoltaica se han convertido en un campo de investigación en rápido crecimiento. Sin embargo, la luz ultravioleta representa solo el 4% del espectro solar, mientras que la luz visible representa el 42% de la radiación solar total. Por lo tanto, la comunidad científica centró sus esfuerzos en la optimización y extensión del espectro de absorción de materiales, basados en semiconductores, a la región visible del espectro solar. Las técnicas establecidas incluyen el dopaje del semiconductor o la deposición de un elemento o sustancia diferente sobre la superficie del material.

Desde 2004, la deposición de nanopartículas plasmónicas (NP) en semiconductores surgió como una posible solución para generar electrones energéticos capaces de impulsar reacciones bajo irradiación visible. Desde entonces, se han publicado numerosas contribuciones en el campo de la fotocatálisis por medio de la excitación de plasmones con aplicaciones relevantes en la disociación de agua, síntesis orgánica y energía fotovoltaica.

En el campo de la fotocatálisis heterogénea, los electrones energéticos generados por plasmón fueron ampliamente aceptados como responsables del efecto catalítico observado de las NP plasmónicas. Recientemente, varias contribuciones científicas han cuestionado el mecanismo real que desencadena las reacciones catalizadas por plasmón, con la hipótesis de que los efectos térmicos son, en cambio, el factor predominante que influye en la actividad de un catalizador plasmónico.

Nuestro objetivo fue diferenciar entre los efectos térmicos y electrónicos de los NP plasmónicos en una reacción de prueba, el acoplamiento reductor de nitrobenceno a azobenceno, bajo irradiación con láseres de 532 nm y/o 875 nm. Además, también nos propusimos desarrollar una metodología que pudiera replicarse fácilmente en otros laboratorios y usarse como prueba de referencia para reacciones en solución donde se explota la excitación de plasmones.

En este trabajo se ha optimizado el tamaño y la forma de las partículas de oro, AuNPs, para obtener catalizadores caracterizados de diferente absorción en la región visible e infrarroja cercana (NIR) para controlar y seleccionar los efectos electrónicos y térmicos del catalizador. La actividad de los catalizadores sintetizados para la reacción de prueba se comparó con la actividad del catalizador de referencia tipo A del Gold World Council.

La caracterización del catalizador de Au/TiO_2 sintetizado con mediciones de reflectancia difusa evidenció que la presencia de pequeñas cantidades de AuNP no modificó la posición de la banda prohibida del soporte, lo que sugiere que, bajo irradiación de luz visible, la catálisis se produjo en la superficie de los AuNP. La determinación de la entalpía de activación para cada paso de la reacción mostró que el segundo paso de la reacción estaba fuertemente influenciado por la irradiación láser de 532 nm. De hecho, nuestros cálculos demostraron una diferencia de energía entre las reacciones iluminadas y oscuras en el primer paso de reacción de $1.1\ Kcal\ mol^{-1}$ mientras que la del segundo paso fue de $5.9\ Kcal\ mol^{-1}$.

Además, se analizaron los resultados de experimentos diseñados explotando principios de estadística y ejecutando la reacción de prueba en presencia de dos catalizadores que se diferencian por las formas de las AuNP y bajo diferentes fuentes de láser. Los resultados se procesaron para obtener modelos fenomenológicos predictivos para el intermedio y el producto de la reacción, azoxibenceno y azobenceno, respectivamente.

Los modelos obtenidos permitieron confirmar que en la reacción investigada los efectos electrónicos son predominantes con respecto a la contribución de los efectos térmicos, generados por interacción electrón-fonón de los AuNP cilíndricos, no influyó significativamente en el resultado de la reacción.

Acknowledgements

I started this life-changing experience about 5 years ago in 2015. When I first arrived in Barcelona, I met Prof. Romain Quidant and Dr. Ignacio De Miguel from which I learnt a lot scientifically and professionally. I am deeply thankful to Prof. Romain Quidant for pushing me to be a better scientist, to be critical and systematic and to work hard. I am grateful also for all the meetings where your suggestions and questions allowed me to go back to the lab with new ideas and solutions to scientific problems. Thanks to your guidance I learnt to not give up even after 101 failed experiments. After all, what really does matter is when you find out that the 102nd experiment work AND it is reproducible. Special thanks to Dr. Ignacio De Miguel tor all the valuable scientific conversations about nanotechnology and surface chemistry and for being a kind and wonderful colleague.

I also am grateful to Prof. Miquel A. Pericas and Dr. Esther Alza and Dr. Mauro Fianchini from ICIQ for providing access to their laboratories and instruments for the characterization of the catalysts as well as all the inspiring scientific conversations that boosted my work. Through the collaboration between my group and the ERTFLOW unit managed by Dr. Esther Alza, I learnt how to work between two very different and physically distant laboratories. I recognize that this is a privilege that not all the Ph.D. students can enjoy and I am glad I collected also this experience.

It is also important to remember that a Ph.D. is not only made of study, experiments and data treatment, it also has its foundation on

transversal skills that can be generally applied in life and work such as being pragmatic, organized and flexible, and to have a wide perspective when facing a problem. Those skills became part of my expertise thanks to all the above mentioned people but also thanks to my colleagues and friends that inspired me and supported me when I needed to achieve my objectives.

Finally, I want to thank my family, Angela, Piero, Sonia, Catia, Giorgio, Enrico, Lorenzo and Valerio for loving and supporting me no matter what.

I want to thank Stella for allowing me to reserve to her a special place in my heart, for all the moments we spent together enjoying the really meaningful things in life like a well done coffee (with milk and ice, no sugar, all in the same glass possibly) and the chirping of the cicadas, the company of good friends, the family.

Also, I wish one day my daughter would read this thesis or at least the abstract and then ask me questions. I will try to answer to all of them aiming to inspire in her curiosity and interest for science and critical thinking.

Of course, all members of my group contributed substantially to the creation of the scientist that now I am therefore I feel the urge to thank all the PNO group: Piergiacomo, Nadine, Arantxa, Adeel, Irene, Bernard, Andrés, Gerard, Alexia, Marc, Helena, Pascal, José, Vanesa, Vincenzo, Esteban, Johann, Pascal, Josep, Paulina, Luis, Victor, Roger, Ozlem, Francesco, Raúl, Laurent, Jordi, and all the friends that made my stay in Barcelona a pleasant and unforgettable experience, Marco P., Sara,

Nicola, Giuseppe, Federica, Tanja, Dragan and Luka, Jacopo, Marco M., Aldo, Emanuele Canu.

Also, I want to thank all the friends that have been far from me since I came here in Barcelona but still, they are cornerstone in my life. Even from distance you meant so much to me, thank you Fabrizio, Abramo, Enrico Maria, Valerio, Giulia. I hope soon we will be able to do many other "zingarate" like the old times.

Contents

List of Figures

List of Tables

Abbreviations

AuNP	gold nanoparticles
AuNR	gold nanorods
BE	binding energy
BET	Brunauer–Emmett–Teller
DoE	design of experiment
IPA	isopropanol
LM	linear model
LME	linear mixed-effect model
NIR	near infrared
NIR	near infrared
pXRD	powder X-ray photoelectron spectroscopy
UV	ultra violet
XPS	X-ray photoelectron spectroscopy

1 Introduction

Modern society strives to achieve the efficient utilization of renewable solar energy for chemical transformations. Since 1969, the pioneering work of Fujishima and Honda[1,2] on titanium dioxide, TiO_2, photocatalysis has boosted the interest on semiconductor-based catalysts. Photocatalytic materials based on semiconductors (e.g., TiO_2, ZnO, Fe_2O_3, CeO_2, Bi_2O_3) have been comprehensively investigated for applications in different fields of heterogeneous photochemistry such as water splitting[3], organic transformations[4], and environmental decontamination[5].

Heterogeneous photocatalysis involves the enhancement of the speed, yield, and/or selectivity of a reaction by irradiating the system, composed by the catalyst and the reagents, with UV or visible light. A catalyst is defined as heterogeneous when its state of aggregation is different from the state of aggregation of the reagents (***Figure 1.1***).

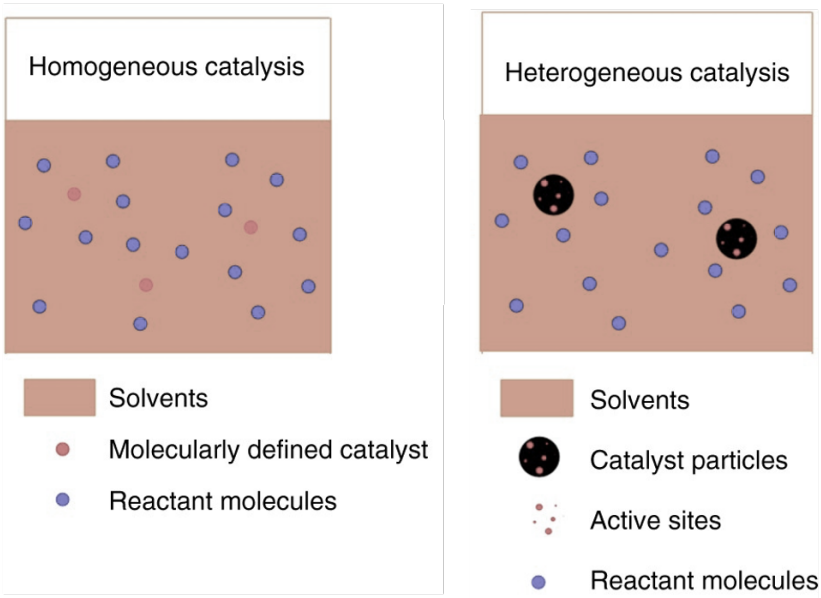

Figure 1.1 Sketch depicting the difference between homogeneous catalysis and heterogeneous catalysis.[6]

A photocatalyst[7] is a substance that can absorb the energy of the incident electromagnetic radiation, ultraviolet, visible, or infrared (IR) and create an excited state that repeatedly interacts with the reactants forming reaction intermediates and products. The photocatalyst must also be able to regenerate itself after each cycle.

Photocatalysis based on semiconductors suffers from limitations due to the band gap energy of the material, usually above 3 eV. This band gap restricts the absorption of the material to the UV region, which accounts for only 4% of the incoming solar radiation, whereas the visible and IR parts[8] account for 42% and 51%, respectively (**Figure 1.2**).

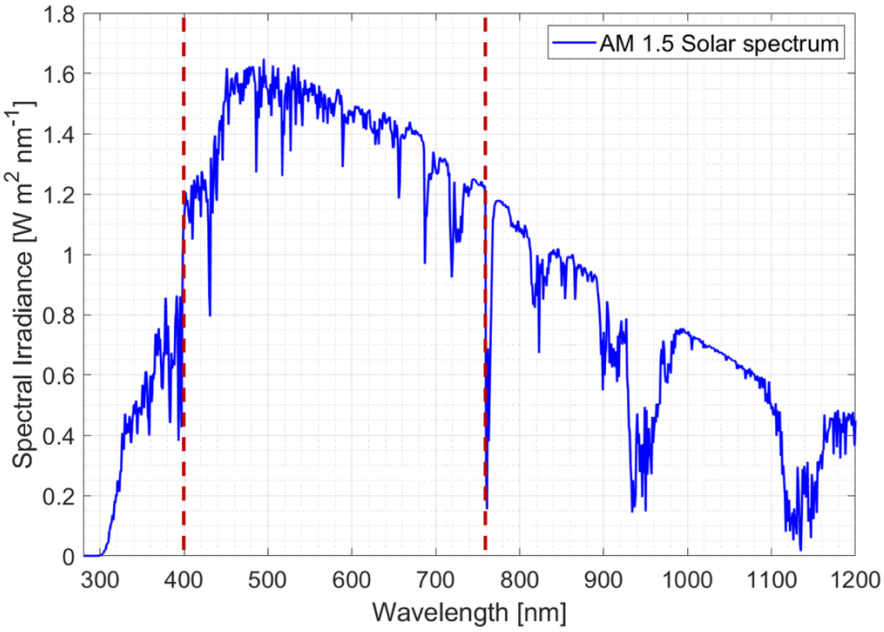

Figure 1.2 Reference solar spectrum irradiance AM 1.5. UV-B and UV-A regions from 290 to 400 nm, visible region from 400 to 760 nm, part of the near-infrared region from 760 nm to 1200 nm. AM: air mass coefficient.

The most widely investigated photocatalyst is TiO_2, owing to its high stability and activity under UV light irradiation. TiO_2 based photocatalysis already found commercial applications, such as wastewater treatment and self-cleaning glasses[9]. Other areas of investigation where TiO_2 is used alone or in association with other substances (e.g., metal nanoparticles) include, the decomposition of volatile organic compounds and NO_x species in air, organic redox reactions, and photovoltaic cells. Globally, TiO_2 has proven to be very promising for the development of sustainable technologies for the future.

On the other hand, running a photocatalytic reaction under visible light irradiation allows applying milder reaction conditions, decreasing

energy consumption, and creating the possibility to exploit a renewable energy source, i.e. sunlight. Besides, engineering a photocatalyst to shift its absorption from UV to visible light permits to fine-tune the selectivity of the catalyst and to obtain partially oxidized[10–12] or reduced[13,14] products not achievable with conventional catalysis[15] (e.g. under high pressure and temperature).

For efficient exploitation of solar light, the extension of the absorption spectrum of a semiconductor (usually limited to the UV region) is desirable. This feature is obtained through the reduction of the band gap of the semiconductor. Most approaches include self-doping by introducing oxygen vacancies[16] into the lattice of the material or doping with other elements[17]. Finally, surface deposition of quantum dots[18,19] and plasmonic nanoparticles (NPs)[14,20–24] emerged recently as alternative methods to extend the visible absorption and the selectivity of the hybrid catalyst. Metal NPs such as copper, silver, and gold[25] show strong tuneable absorption in the UV-Visible range because of localized surface plasmon resonance (LSPR) effects and have demonstrated great potential for applications in photocatalysis under visible light irradiation[26–28].

To the best of our knowledge, the first evidence of plasmon catalysed photoelectrochemical reaction was reported in 2004 and described the visible-light-induced generation of electrons using gold nanoparticles (AuNPs) deposited on TiO_2 electrodes[29].

Since then, there have been numerous contributions to the field of plasmon-enhanced photocatalysis with applications in water splitting[30,31], organic synthesis[28,32–34], and photovoltaics[35]. The widely accepted mechanism of reaction involved the non-thermalized electron transfer from the plasmonic NP to the adsorbed molecule or the semiconductor's

conduction band, leaving little room for a possible role of thermoplasmonic effects.

At the same time, theoretical contributions determined the lifetime and the number[36] of energetic electrons generated in the plasmonic NP under visible light irradiation and provided evidence in favour of the participation of those electrons in photocatalytic processes. Other contributions pointed out that, despite the low efficiency[37] of the electron transfer from plasmonic NPs to TiO_2, it was still possible to exploit the plasmon effect of the NP for solar energy harvesting purposes. Nevertheless, even considering that thermal effects were relevant because of the visible irradiation of plasmonic NPs, those effects alone could not completely account for the enhanced reactivity under visible illumination[38–40]. Finally, Govorov *et al.* considered quantum surface[41] and classically derived dissipative effects in the generation of energetic electrons, thus proving that both thermal and electronic effects contributed to the enhancement of H_2 evolution in their reaction[26].

Recently, a critical review[42–44] of a few contributions in the field of heterogeneous photocatalysis, as well as an analysis of the plasmon decay mechanisms into energetic electrons[45], emphasized the need for more cautious design and analysis of experimental results when aiming at determining the mechanism of activation of plasmonic photocatalysts.

Considering the recent debate on the determination of the mechanism through which plasmonic NPs trigger reactions under visible light irradiation, we envisaged a rational approach to quantify and separate the thermal and electronic contributions of plasmonic NPs in a test reaction.

1.1 Objectives and hypotheses

This thesis proposes a methodology to analyse and understand the mechanism by which plasmonic catalysts influence organic reactions in solution. Given the still open debate on this argument, we felt the need to run a series of experiments able to differentiate between the thermal and electronic effects in plasmonic catalysis. Furthermore, the techniques and instrumentations used in this work were constituted by standard equipment commonly present in any chemistry laboratory or easily implementable (such as laser sources), so that the proposed methodology could be replicated conveniently.

I focused on the study of a catalytic system composed by AuNPs and gold nanorods (AuNR) supported on inorganic oxides, either semiconductors (TiO_2, Fe_2O_3, CeO_2) or SiO_2. The activity of the Au-based catalysts was investigated in the reductive coupling of nitrobenzene to azobenzene[46–51] (**Figure 1.3**) under laser irradiation.

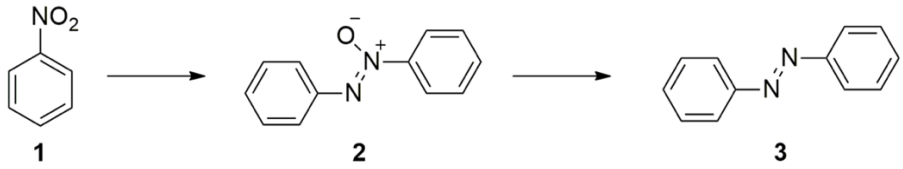

Figure 1.3 Scheme of the test reaction used in this study. Nitrobenzene **1**, azoxybenzene **2**, azobenzene **3**.

As a preliminary objective of this thesis, I focused on optimizing a method to synthesise a AuNP photocatalyst able to enhance the speed

and yield of a specific reaction (i.e. nitrobenzene reduction) under visible laser irradiation. The activity of AuNPs-based catalysts was examined screening particle size, the kind of support and synthetic method. The outcome of the reactions ran with the synthesised catalysts was compared with the results obtained for a commercial catalyst constituted by AuNPs supported on TiO_2 (Gold World Council reference catalyst type A[24,52] purchased from Haruta Gold Inc.). Two different shapes of AuNPs were used in this study, spherical and cylindrical. The former being characterized by small size and a higher number of energetic electrons compared to the latter, commonly used as a source of heat in many fields of investigation. Activation enthalpy for the reaction steps was also determined under irradiation and in the dark for the best performing catalyst.

The hypotheses motivating this work were the following:

- **a.** The reaction is activated by plasmon generated energetic electron-holes.
- **b.** The irradiation with a 532 nm laser on spherical NPs enhances the reaction through electron transfer events.
- **c.** The irradiation with a 785 nm laser on cylindrical NPs contributes to the reaction only through collective thermoplasmonic effects.
- **d.** The contemporary use of the two shapes of NPs and laser sources generates a mixture of effects that trigger the test reaction.

Exploiting principles of design of experiment[53] (DoE), a set of experiments were prepared to rationally explore the influence of different laser sources and catalyst types had on the test reaction. The collected

data constituted a model that allowed to determine the kind of dominant plasmonic effect taking part in the catalytic cycle of the investigated reaction.

1.2 Overview of LSPR for metal nanoparticles

LSPR is a phenomenon that involves the resonant interaction of the electric field of the electromagnetic radiation with the free conduction electrons of a metallic NP. The intensity of the plasmon is maximum at a characteristic frequency (plasmon frequency) that depends on the nature of the metal and the size and shape of the NP and the dielectric constant of the surrounding medium.

The electrons of a metal are considered delocalized in a lattice constituted by positive ions. As a consequence of the irradiation of a metal NP at the plasmon frequency (typically in the UV-Vis region), the conduction electrons collectively oscillate around the fixed ionic lattice. A metal sphere much smaller than the illumination wavelength can be treated as an electromagnetic dipole for which the sphere polarizability[54] is defined by equation (1.1).

$$\alpha = 4\pi r^3 \frac{\varepsilon - \varepsilon_s}{\varepsilon + 2\varepsilon_s} \qquad \text{Eq. (1.1)}$$

Where, r is the radius of the NP, ω is the angular frequency of the electric field, ε and ε_s are respectively, the complex relative permittivity of the metal NP and of the surrounding medium. Assuming the dielectric constant of the surrounding is constant and real, the resonance occurs at a frequency at which $Re[\varepsilon(\omega)] \approx -2\varepsilon_s$.

In the more general case of elongated NPs, the polarizability can be rewritten considering the geometry of an ellipsoid characterized by three semiaxes: $a_1,\ a_2,\ a_3$. For AuNR, a prolate ellipsoid ($a_1 > a_2 = a_3$) sufficiently approximates the geometry of the particle. The polarizability along the principal axes is given by equation (1.2).

$$\alpha_i = 4\,\pi\,a_1\,a_2^2\,\frac{\varepsilon - \varepsilon_s}{3\,\varepsilon_s + 3\,L_i\,(\varepsilon - \varepsilon_s)} \qquad \text{Eq. (1.2)}$$

Where, L_i is a geometrical factor. The consequence of equation (1.2) for the specific case of a AuNR is that the particle would show two resonances due to oscillations along the major and minor axes. The resonance of the major axis can show a significant shift of the plasmon to lower frequencies (near-infrared region).

The absorption and the scattering of the particle can be expressed as a function of the polarizability. Therefore, the absorption and cross-section scattering for a spherical NP are determined by equations (1.3) and (1.4).

$$\sigma_{abs} = kIm(\alpha) \qquad \text{Eq. (1.3)}$$

$$\sigma_{sca} = \frac{k^4}{6\pi}|\alpha|^2 \qquad \text{Eq. (1.4)}$$

Where, $k = 2\pi/\lambda$ is the angular wavenumber. The plasmon peak(s) of metal NPs of Cu, Ag, Au and Al, can be measured conveniently through UV-Visible extinction spectroscopy. For spherical AuNPs smaller than 90 nm the absorption is dominant over the scattering cross section[55]. The results obtained applying the dipolar approximation are strictly valid for small nanoparticles but, in practice, the equations reported above constitute a good approximation for spherical or ellipsoidal NPs with dimension below 100 nm.

Mie theory and numerical methods take into account retardation effects and the radiation damping that contribute to the redshift and broadening of the plasmon for larger and anisotropic NPs[36]. These approaches have been applied to model the optical response of plasmonic NPs in relevant works[55–58]. A complete treatment of such methods goes beyond the scope of this thesis.

Concerning catalysis and energy applications, the physical phenomena that determine the activity of plasmonic catalysts are related to the decay of the plasmon[27]. After the absorption of a photon of appropriate energy, the plasmon initially dephases very fast within 10 fs[59], contributing to the broadening of the plasmon peak (**Figure 1.4 a**).

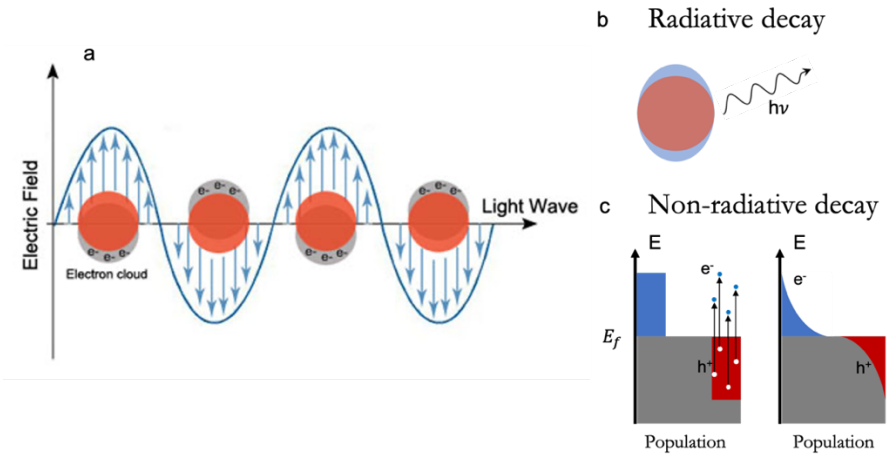

Figure 1.4 Plasmon excitation and damping processes in small metal NPs. **a**. The resonant interaction of the electric field with the free electrons of the metal nanoparticles generates a collective oscillation of the electron cloud. **b**. Radiative decay contributes to the damping of the plasmon oscillation through the near field reemission of light (relevant for relatively big NPs > 50 nm). **c**. Non-radiative decay transfers the absorbed energy of the plasmon to single-electron interband and intraband excitations generating a non-Fermi-Dirac distribution of states. The system then redistributes the energies through electron-electron scattering $\tau_{e-e} = 100fs$. Eventually, the electrons interact with the phonons generating heat (not shown).

Subsequently, the dephased plasmon can decay by following mainly two paths; radiative and non-radiative decay. In radiative decays, elastic reemission generates a local effect called near field enhancement (relevant for big NPs with a size $> 50\,nm$) that consists in an increase of the optical intensity in the surrounding of the NP up to several orders of magnitude higher than the incident light (**Figure 1.4 b**). Non-radiative decay occurs within 100 fs determining a non-thermal Fermi-Dirac distribution of pairs of electrons and holes (electrons are excited up to $E_f + h\nu_P$ where, E_f is the Fermi level of the particle and ν_P is the frequency of the plasmon). Those electron-hole pairs then thermalize through electron-electron scattering to states closer to the Fermi level

(**Figure 1.4 c**). The final event is the transfer of the energy gained by the electrons to the phonons of the NP and then to the medium, generating a temperature increase of the particle and its surrounding. This occurs in a longer timescale, between 100 fs and 10 ps.

This last interaction is always present in plasmonic metal NPs as a direct consequence of the electron excitation[55]. The magnitude of the heating varies depending on the size and shape of the particles[60–62] and is proportional to the intensity of the irradiating light. It can also be optimized according to its intended application. For example, AuNRs have been extensively applied for photothermal cancer therapy *in vitro* and *in vivo*, as well as for photothermal chemistry[44,55]. On the other hand, spherical AuNPs can produce the highest number of energetic electrons when their size is below the mean free path of the electrons (around 40 – 50 nm). Typically, theoretical studies have determined that AuNPs of sizes between 10 and 20 nm ensure the highest number of excited electrons[60]. For practical uses in chemistry, the efficiency of a plasmon photocatalyst must be evaluated considering also the active surface of the particle, the wavelength and intensity of light, and the energy of the molecular orbitals involved in the transformation. For instance, AuNPs of sizes above 20 nm have nearly no catalytic activity[63] although those particles show an absorption cross-section much bigger than smaller NPs (e.g. 5 nm AuNPs).

Thermal effects can be quantified easily using equation (1.5) when the absorption cross-section of the particle is known.

$$Q = \sigma_{abs} I \qquad \text{Eq. (1.5)}$$

Where, Q is the power delivered by the NP to the environment in the form of heat.

The absorption cross-section can be calculated for spherical NPs by using equations (1.1) and (1.3). The temperature increase of a single spherical NP irradiated at the plasmon frequency is given by equation (1.6).

$$\Delta T = Q 4\pi\kappa R \qquad \text{Eq. (1.6)}$$

Where, κ is the thermal conductivity of the medium and R is the radius of the particle.

For other more complex morphologies, the computation of the inner electric field amplitude is necessary to estimate the heat delivered from the particle and it must be performed with numerical methods[55]. Moreover, dealing with arrays or ensembles of NPs in suspension adds an extra layer of complexity. The inter-particle distance plays a determinant role in heating the whole system[64] (NP and the surrounding medium) giving rise to collective effects. For a two-dimensional array of NPs, collective effects can be estimated and predicted by applying equation (1.7).

$$\zeta_2 = \frac{p^2}{3LR} \qquad \text{Eq. (1.7)}$$

Where, ζ_2 is a dimensionless parameter that estimates the ratio $\Delta T_0^s / \Delta T_0^{ext}$ (the temperature variation of the particle positioned at the centre of the system divided by the temperature variation in its surroundings), p is the distance between particles, L is the beam size, and R is the radii of the particles.

For $\zeta_2 \ll 1$, collective effects predominate. This effect is even more dramatic in three-dimensional systems (e.g. NPs colloids).

1.3 Determining the mechanism of plasmonic photocatalyst, an open debate

As mentioned in the previous section, the electronic and thermal effects cannot be completely separated for plasmonic NPs, they are just unavoidable consequences of the decay of the plasmon resonance. Yet, the morphology and the size of the NP can be optimized for maximising either the electron excitation or the heat generation. Indeed, small spherical NPs are preferred for photocatalysis since they can generate electron-hole pairs, thus minimizing the heating effects, and they show bigger active surfaces. On the other hand, relatively big AuNRs are instead exploited for their thermal effects, mainly in photothermal therapy[55]. The photothermal effect of AuNR of lengths ranging from 20

to 65 nm (decorated with small Pd-NPs) has been exploited in Suzuki reactions[65].

In the last few years, the scientific publications focusing on the discrimination between photothermal and electronic effects have increased considerably[66–70], evidencing a growing interest in assessing the nature of the plasmonic photocatalysis.

The time-average number of excited electrons generated during continuous wave irradiation can be determined using equation[71] (1.8).

$$< N_{e^-} >= \frac{\sigma_{abs}\, I\, \tau_{e\text{-}e}}{h\nu} \qquad \text{Eq. (1.8)}$$

Where, σ_{abs} is the absorption cross-section of the NP, I is the irradiance of the incident light, $\tau_{e\text{-}e}$ is the electron-electron scattering timescale, and $h\nu$ is the photon energy.

For a spherical particle of 10 nm[72] ($\sigma_{abs} = 6.1 \times 10^1$ nm^2) under continuous wavelength irradiation with $I = 2 \times 10^3$ W/m^2, typical irradiance used in the experiments reported in this work, and assuming a $\tau_{e\text{-}e}$~50 fs, the time-average number of excited electrons is 1.7×10^{-8}. Notably, under the conditions mentioned above, one particle absorbs approximately 300,000 photons per second, generating an equivalent number of excited electron-hole pairs. Therefore, despite that the short lifetime of electron-hole pairs (**Figure 1.4 c**) does not favour the driving of reactions on the surface of the particle, we cannot exclude the possibility of catalysis via electron transfer to adsorbate molecules.

Therefore, the main disadvantages of plasmon-enhanced photocatalysis via electron-hole pairs are their short lifetime and their time-average number. In the specific case of photocatalysis for organic molecules, to have an efficient electron/hole transfer, the acceptor (donor) must be in contact and interact with the catalyst surface (hence, it must be adsorbed). The energetic levels of the LUMO (lowest unoccupied molecular orbital) and HOMO (highest occupied molecular orbital) must be of appropriate energy to have an electron-hole transfer.

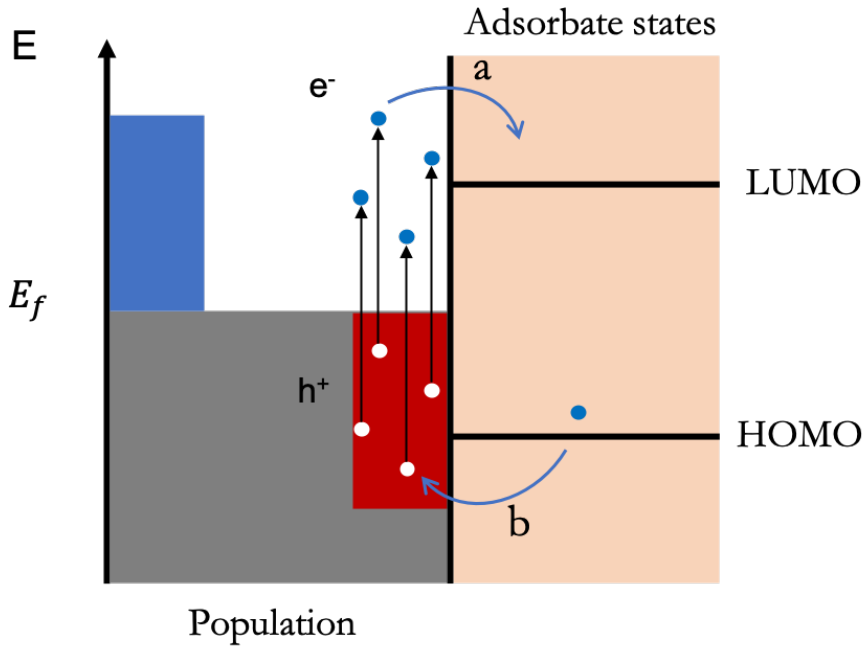

Figure 1.5 Two possible scenarios for single electron transfer in a reaction catalysed by a plasmonic metal catalyst. **a**. The energetic electron is transferred on the LUMO of an adsorbate state of appropriate energy. **b**. An electron occupying the HOMO of the adsorbate is transferred to the plasmon generated hole of the catalyst.
e^-: electron; h^+: hole

The sketch of **Figure 1.5** represents two possible situations in plasmon-driven catalysis. Depending on the energetic levels of the molecular orbitals and on the density of states generated in the catalyst after plasmon excitation, the catalyst may contribute to the reduction (path **a**) or the oxidation (path **b**) of the reactant molecule. Density functional theory calculations can provide additional evidence to sustain a direct or indirect electron transfer to adsorbate molecules[14]. Moreover, an alternative mechanism has also been proposed that consists of the transient electron transfer to adsorbate O_2 molecules in the case of ethylene epoxidation[73]. The electron is first transferred to the oxygen molecule and then is back-transferred to the metal catalyst after depositing vibrational energy, thus weakening the molecular bond and enhancing the dissociation rate.

In the majority of previous reports in the field of plasmonic photocatalysis, the screening of the irradiation power is the most common evidence supporting the photocatalytic mechanism of the catalyst under investigation. The experimenters would demonstrate a proportionality between the rate of the reaction and the rate of the incident photons absorbed by the sample to support the hypothesis of a plasmon driven catalysis. This kind of experiments, if not supported by more evidence, fails to provide information on the mechanism of activation. Indeed, there are limitations to the application of this approach, such as the power range that can be screened. The increase of temperature of a system under irradiation is approximately proportional to the intensity of the light reaching it. Taking into account that the rate of a reaction is usually influenced by temperature following the Eyring law, in order to exclude a thermoplasmonic effect, the range of intensities

should span over several orders of magnitude[74] and not just by a factor of 2 or 3. Again, the extended range of intensities may bring further complications since, under high optical irradiance, collateral reactions and changes in the mechanism might occur. On the other hand, at low irradiances, very sensitive measurements of the reaction rate might be necessary. Consequently, the variation of the illumination power should be accompanied by other experiments, such as the variation of the light beam diameter (applicable for collimated light). This approach can help to understand the mechanism of the catalysis by studying the relationship between the reaction rate and the beam diameter and by comparing two scenarios: varying the diameter through the use of a diaphragm (constant irradiance) or defocusing the incident beam (constant power). Under these experimental conditions, a purely photochemical reaction subjected to constant power would give a constant rate of reaction as a function of the beam diameter, whereas under constant irradiance a quadratic dependency on the beam diameter should be observed. Instead, in a process where thermoplasmonic effects were influencing the catalysis, a linear dependency of the reaction rate under constant power would be expected. Under this condition, the temperature increase is inversely proportional to the beam size (equation 1.6). On the contrary, under constant irradiation, the temperature increase of the catalyst is proportional to the beam size and the rate of the reaction should show a cubic proportionality with the beam diameter. The variation of the beam diameter is applicable only for two-dimensional systems, such as surfaces and optically thick substrates (for which only a superficial interaction of the light with the material can be assumed). In the case of a catalyst suspended in a liquid, the heat diffusion mechanism is more complex[75]. This approach cannot be applied easily since the assumption of heat

diffusion through an infinite medium is not satisfied in the case of a catalyst in a liquid. The system is thermally insulated (air, glass vessel) and accumulation of heat is likely to occur.

Another issue, often underestimated, is the measurement of the temperature variation of the reaction environment due to illumination. In the majority of experiments, the size of the beam is much bigger than the distance between the NP, implying that collective thermal effects predominate, as illustrated in equation (1.7). Thermal camera measurements are suitable whenever the reaction is performed in the gas phase, provided that the instrument is properly calibrated on the substrate and that the reaction chamber is equipped with IR windows. The calibration of the IR camera should be performed experimentally so that an average emissivity of the catalyst can be determined by heating the substrate at specific temperatures.

However, when the reaction is performed in liquids, as in this study, the use of an IR camera is not suitable because the thermal image would measure only the temperature on the surface of the reaction mixture. In this case, the use of a thermocouple (immersed in the reaction mixture) would be more appropriate to accurately measure the temperature of the system. Nonetheless, caution should be applied to ensure that the light does not illuminate directly the thermocouple to avoid direct heating of the probe. Yet, the probe should be placed, if possible, in direct contact with the catalyst to avoid underestimating the temperature. Overall, ignoring collective thermal effects along with an incorrect measurement of the temperature could drive the experimenter to wrong conclusions, as pointed out recently[43,68,76].

In addition, to discriminate between thermal and electronic effects, it is also advisable to study the influence that two different wavelengths could have on the plasmonic catalyst. In this scenario, different rates of reaction enhancement under different wavelengths could be expected for the same plasmonic structure. For example, considering a spherical AuNP supported catalyst whose plasmon absorption is centred around 530 nm and is irradiated by two lasers, one emitting at 532 nm and the other at 785 nm. Energetic electrons would be generated after resonant interaction at the appropriate wavelength, while thermal effects would result from the absorption of light off resonance in the NIR region.

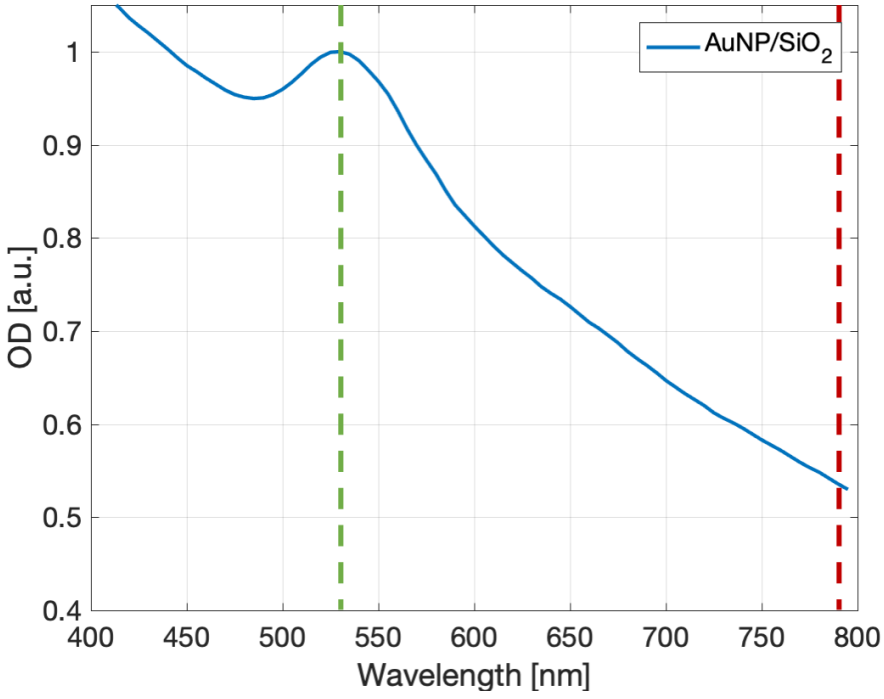

Figure 1.6 Visible spectrum of AuNPs on SiO_2 catalyst. Green dashed lines are placed at a laser irradiation wavelength of 532 nm and red dashed lines at 785 nm.

As illustrated in **Figure 1.6** the catalyst does not have the same absorption at the two wavelengths. Moreover, the accurate measurement of the absorption of the sample can be difficult, especially for scattering media such as a solid suspension in liquids, often requiring diffuse reflectance spectroscopy techniques[77]. However, it is still possible to compare the effect of the two wavelengths of irradiation by varying the optical power of the two sources. Therefore, a plot of the speed of the reaction as a function of the laser power, for a hypothetical first-order reaction that can be influenced also by temperature, could give, as pointed out by Baffou *et al.*[71], one of the two scenarios represented in **Figure 1.7**.

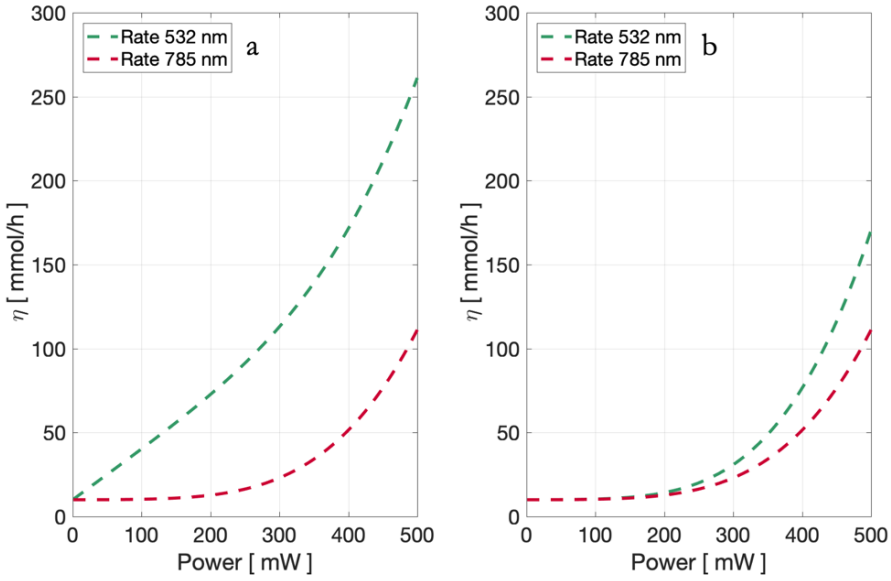

Figure 1.7 Expected rate of reaction as a function of optical power for different wavelengths and depending on the kind of dominant plasmonic effect on the mechanism of the catalysis. **a**. The reaction is affected by both the thermal effect and the electronic effects of the plasmonic catalyst. **b**. The reaction is only affected by thermal effects.

In the first case (**Figure 1.7 a**), the variation of the 532 nm laser is accompanied by a superlinear variation of the reaction rate, particularly evident at high irradiation power, while the influence of the 785 nm laser is exponential and evident at very high intensity. In this case, the mechanism of the reaction corresponds to a mixture of electronic and thermal contributions. The other possibility (**Figure 1.7 b**) is that the reaction is driven purely by thermal effects, thus the rate enhancement would depend only on the temperature increase caused by the irradiation of the catalyst. The different shape of the curves would depend on the different magnitudes of absorption of the catalyst.

In conclusion, when the determination of the mechanism of plasmonic catalysis is required, the control of the temperature of the reaction mixture is of paramount importance. Indeed, in the cases exposed in **Figure 1.7**, being able to keep the system at a constant temperature would affect the shape of the plots. Ideally, the thermal effects of both lasers would be minimized, the curves characterized only by thermal effects (red dashes in **Figure 1.7**) would be instead constant as a function of the optical power, since the rate of reaction would be nearly the same as the one of the dark reaction. However, the reaction rate under 532 nm laser irradiation would be well approximated by a linear fit.

2 Techniques and methods

Here are reported all the techniques and methods applied in this work to optimize the catalyst and understand the mechanism of activation of plasmonic catalysis.

2.1 Test reaction

Nitrobenzene reductive coupling reaction, represented in **Figure 2.1**, was selected to optimize the catalyst synthesis and investigate its interaction with visible light sources. In the first stage, the performances of the synthesised catalysts were investigated using this reaction under laser irradiation with a 532 nm laser. In a second stage, the irradiation conditions were systematically screened to understand the activation mechanism of AuNPs under laser irradiation.

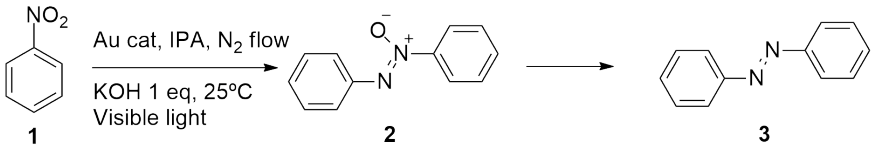

Figure 2.1 Nitrobenzene reductive coupling reaction. **1** nitrobenzene, **2** azoxybenzene, **3** azobenzene.

The main steps involved in the formation of the product are described in **Figure 2.2**. Briefly, isopropanol (IPA) oxidation to acetone allows the

formation of the Au-H species, which are then involved in the initiation of the catalytic cycle. Then, Au-H surface species are formed and react with the N-O bonds of nitrobenzene causing the cleavage of the bond. Finally, the HO-Au species decomposes, forming O_2 and regenerating the Au-H species.

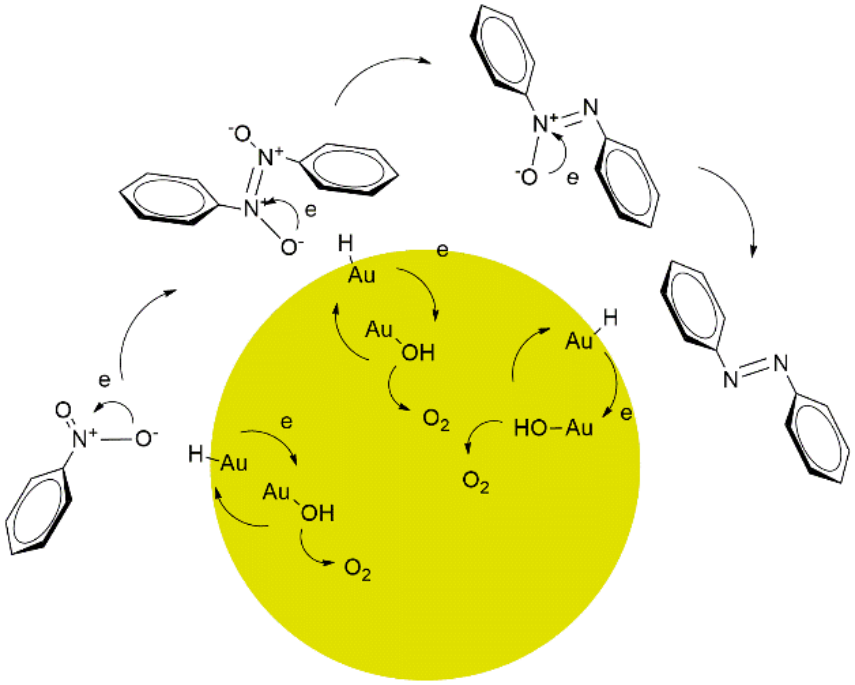

Figure 2.2 Proposed reaction mechanism in the presence of plasmonic gold catalyst reproduced with permission from[78].

The overall redox process is believed to occur only on the surface of the AuNP[78] and this makes the reaction a good candidate to investigate the activation mechanism of plasmonic NPs while minimizing the influence of the support. Therefore, any improvement to the reaction

outcome can be directly related to effects generated by the noble metal nanoparticles.

Azobenzene and its derivatives are widely used as dyes for textile and food, pesticides, molecular switches, drug delivery and drugs, biological makers[49]. Moreover, the industrial synthesis of the abovementioned molecules is based on the formation of diazonium salts, or the use of stoichiometric amounts of reductants such as sodium or magnesium amalgam or H_2. All the above intermediate and reactant are dangerous and explosive. Therefore, it is important to investigate alternative safer and greener procedures to convert nitrobenzene to azobenzene.

2.1.1 Nitrobenzene reduction procedure

The nitrobenzene reductive coupling here described consisted in the reduction and further coupling of two molecules of nitrobenzene to yield azobenzene. Moreover, a stable intermediate, azoxybenzene **2**, was formed (**Figure 2.1**).

The optimized reaction procedure consisted in weighing the required amount of catalyst and placing it in the reaction flask. Subsequently, 1 mL of 0.08 M naphthalene in IPA was added and the suspension was sonicated for at least 30 seconds in an ultrasound bath. Naphthalene was introduced as an internal standard. Then, 1 mL of a freshly prepared 0.1 M KOH solution in IPA was added, followed by 0.1 mmol of reagent **1**. The flask was sealed and connected to a Schlenk line. The atmosphere in the reaction flask was carefully replaced, degassing the solution and introducing nitrogen. A nitrogen stream of 0.5 L/min was established,

flowing nitrogen through a cannula placed in a rubber septum. The reactor was then positioned in the thermostatic bath set at 25 ºC in dark conditions under magnetic stirring at 600 rpm. The temperature was monitored with a thermocouple in direct contact with the reaction mixture. Finally, the light sources were switched on and the reaction was run typically for two hours. The recovered catalyst was centrifuged and washed several times with methanol until no reagents or products were detectable by GC. Eventually, the catalyst was dried in an oven at 110 ºC and was stored in a dark cool place.

2.1.2 Reaction mixture analytical method

The reaction was then monitored, sampling the reaction mixture with a syringe provided of a cannula inserted in the septum, for at least 2 hours. Every sample consisted of 50 μL of reaction mixture and was centrifuged at 18,000 rpm for 20 seconds to remove the catalyst. Then, 40 μL of the supernatant was diluted to 500 μL with toluene, and the mixture was analysed with gas chromatography.

The instrument was an Agilent 6890 gas chromatograph equipped with a BPX5 column (30 m, 0.25 mm, 95% methyl polysilphenylene/siloxane phase, from Trajan®) and a flame ionization detector.

All the injections were performed with an inlet temperature of 300 ºC, a split ratio of 50:1, and constant pressure of 19.98 psi. The temperature ramp was the following: constant temperature for 5 minutes at 120 ºC,

then a temperature gradient of 5 ºC/min up to 300 ºC, which was held for 5 minutes. The detector temperature was 350 ºC.

An internal standard was used to determine the concentration of the three main substances involved in the reaction. The analytical method consists in adding to the reaction mixture a known quantity of an inert substance (naphthalene), and then correct the area of the peaks of analytes with respect to the area of the standard.

In order to ensure the linearity of the detector response for the range of concentrations of the reaction, calibration curves were built for each of the molecules showed in **Figure 2.1**. The calibration curves were determined by mixing different ratios of analytes and internal standard. The concentration of the internal standard was kept constant (0.4 mg/mL) in each sample, while the concentration of the analytes was varied from 0.02 to 0.6 mg/mL to generate the calibration curves showed in **Figure 2.3**.

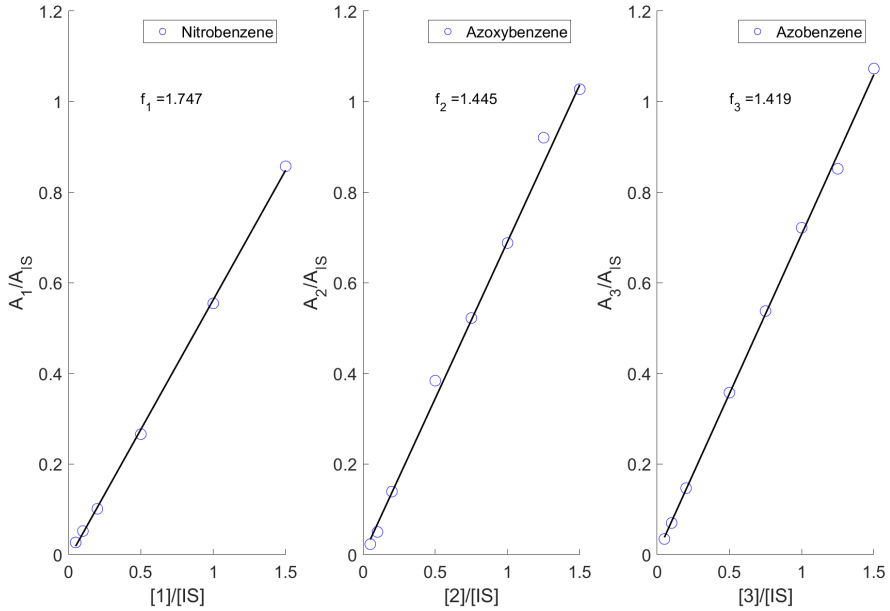

Figure 2.3 Calibration curves and factors for nitrobenzene **1**, azoxybenzene **2**, and azobenzene **3**.

A linear fit of the data gave a factor characteristic of each substance that allowed to correct the area of their GC peaks as represented in **Figure 2.4**.

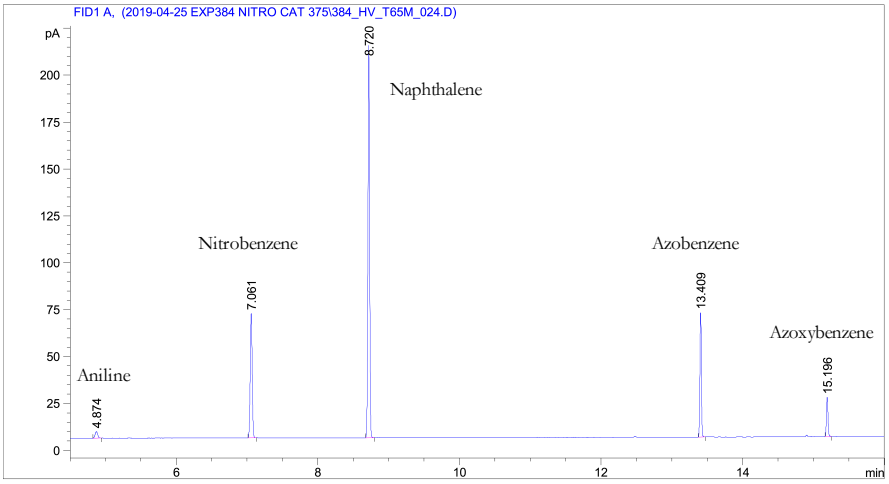

Figure 2.4 Typical GC chromatogram showing the three main components of the test reaction in the presence of naphthalene as the internal standard. Traces of aniline were detected.

With this simple method, I was able to follow the evolution of nitrobenzene, azoxybenzene, and azobenzene by applying equation (2.1).

$$[n] = \frac{A_n * f_n}{MW_n} * \frac{[IS]}{A_{IS}} \qquad \text{Eq. (2.1)}$$

Where n denotes the analyte, A_n is the peak area of the analyte, f_n is the conversion factor, A_{IS} is the area of the internal standard, and MW_n is the molecular weight of the analyte.

2.2 Reaction setup

The reactor consisted of a Schlenk tube provided of a screw cap with a gastight glass window, a lateral neck and a valve as shown in **Figure 2.5**.

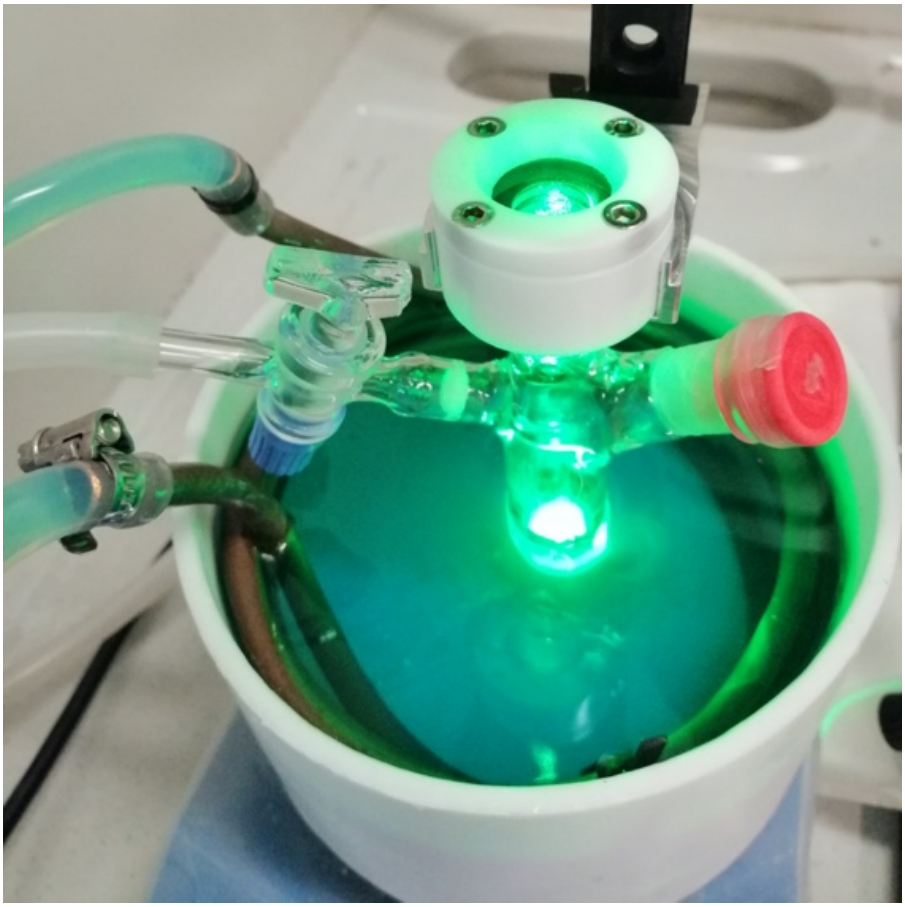

Figure 2.5 Schlenk reactor used to run the reaction.

A variable area flowmeter allowed to control the nitrogen flow (0.5 L/min) during the reaction. The reactor was connected to a Schlenk line

and a needle was introduced in the septum. The nitrogen flow is necessary to keep the reaction under inert atmosphere while stripping the oxygen produced during the reduction of nitrobenzene.

The temperature of the reaction controlled by immersing the reactor in a magnetically stirred ethylene glycol thermostatic bath, as shown in **Figure 2.5**, controlled by a thermal bath circulator (Isotemp R20 from Thermo Fisher Scientific). This equipment allowed to accurately control the reaction temperature from a minimum of -10 °C up to the boiling point of the solvent of reaction, with very low oscillations (± 1 °C) of the reaction temperature. The system was calibrated by irradiating the reaction mixture with both lasers and by varying the chiller temperature setpoint. The calibration curve is represented in **Figure 2.6**.

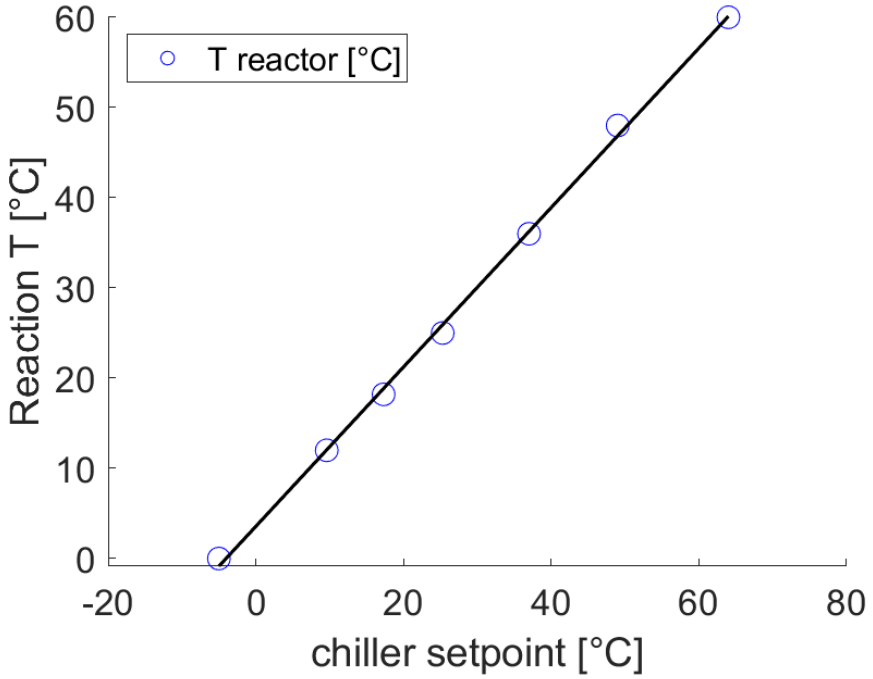

Figure 2.6 Reaction temperature calibration. Reaction conditions: 0.1 mmol of **1**, 0.1 mmol of KOH, and 2mL of IPA. Two lasers were used: laser 1 (532nm and 130 mW) and laser 2 (785 nm 300 mW).

The reaction temperature was measured with a thermocouple immersed in the reaction mixture. Each measurement of the temperature was registered at thermal equilibrium between the thermostatic bath and the reactor. Typically, the equilibrium was reached within 5 minutes after the introduction of the reactor in the thermostatic bath. The difference between the chiller setpoint and the temperature recorded inside the reactor was ascribed to heat losses from the chiller to the tubings and the thermal bath.

2.2.1 Irradiation setup

For the whole study, two laser beams were used as sources of light to trigger the reaction under investigation, **Figure 2.7**.

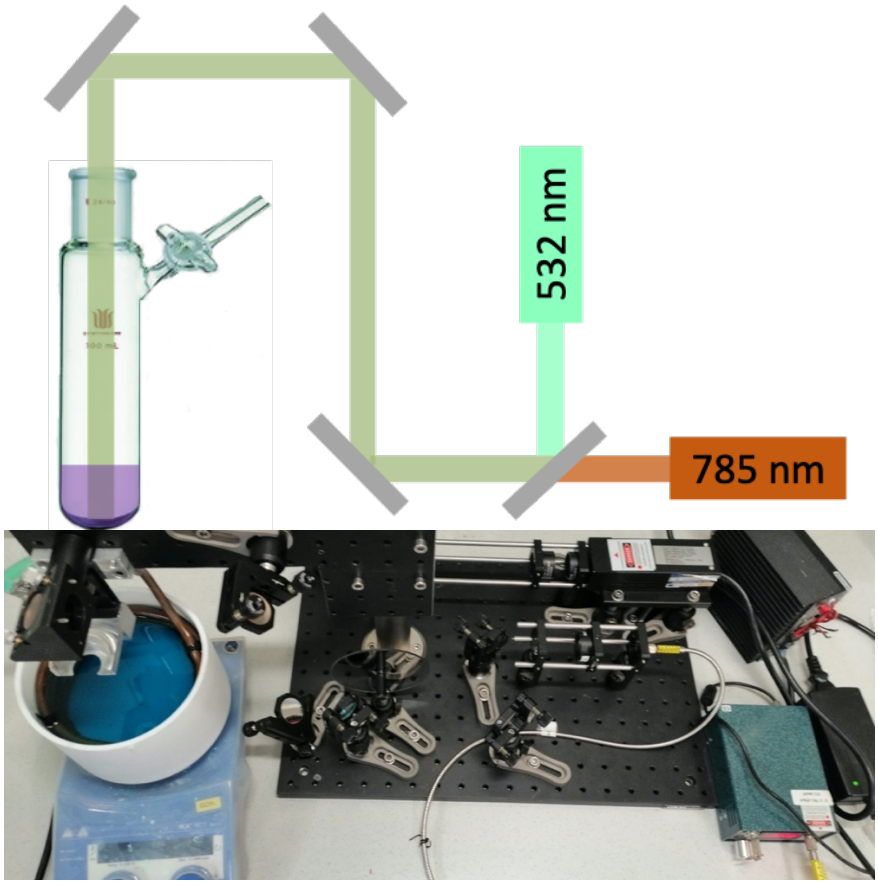

Figure 2.7 Top: irradiation setup sketch. Bottom: top view of the illumination setup used for plasmonic catalysis experiments.

The laser beams (diameter of 9 mm) were aligned coaxially into the reactor. The laser intensities were varied using a neutral density filter, in the case of the green laser, and analogically for the NIR laser. This setup

allowed to vary the irradiance of the two lasers from 0 to $2 * 10^3\ W/m^2$ for the green laser and $4.4 * 10^3\ W/m^2$ for the NIR laser.

2.3 Catalyst characterization

This section describes all the techniques used to identify the main characteristics of the synthesised catalysts.

2.3.1 Inductively coupled plasma – optical emission spectrometry

Inductively coupled plasma optical emission spectroscopy (ICP-OES) was used for preliminary characterization of the candidate catalytic materials, which were synthesised in this work. Samples were analysed through an external service provided by the University of Barcelona. The analysis allowed to determine the % of gold in a sample. Catalysts and colloidal solutions of AuNPs were analysed before and after their use. Moreover, the presence of Cl was also determined in samples taken during the synthesis of the catalyst. Cl ions poison the catalyst, interfering during the synthesis and the use of the AuNP by increasing the average size of the particles[79,80].

2.3.2 X-ray photoelectron spectroscopy

XPS data were obtained from CCITUB service of the University of Barcelona. This technique was used to confirm the oxidation state of gold and to screen the material for traces of contaminants derived from the synthetic procedure.

The data were processed with CasaXPS software as follows. Binding energies (BEs) were corrected by adjusting the position of the C1s peak to 285.0 eV[81].

2.3.3 Powder X-ray diffraction spectroscopy (pXRD)

This technique was used to determine the average bulk composition of the catalyst. It was used to assess the crystalline phase of the support as well as the presence of metallic gold in the catalyst. The measurement was performed by the ERTFLOW group in ICIQ. The powder diffraction system was equipped with a VÅNTEC-1 single-photon counting PSD, a Germanium monochromator and a CuKα-radiation source in transmission geometry. The raw data were processed with MATCH! Software.

2.3.4 Transmission electron microscopy

TEM images were collected through the service provided by the University of Barcelona. The images allowed to determine the size and morphology of the AuNP and the support. This instrument allowed to estimate also the distribution of the nanoparticles on the support surface, as well as the presence of undesired material on the surface. The most common contaminants were salts and surfactant found in the final products due to because of the incomplete removal during the workup of the catalyst.

2.3.5 UV-vis spectra determination

The spectra of the catalysts and colloids were determined using a Synergy H1 Multi-Mode Reader working with a microplate reader of 96 well plates (polystyrene, clear, flat bottom, Nunc MicroWell, Thermo Fisher Scientific). Spectra were measured in transmission registering the optical density (OD) spectrum of visible absorption of aqueous diluted suspensions in Milli-Q water. The typical range of acquisition was from 400 nm to 999 nm in steps of 2 nm. For the studied volume, a cuvette with a 250 μL volume and a 0.69 cm path length was used. Solvent spectrum subtraction was performed for every measurement. Through this technique, the plasmon peak positions of the AuNP and AuNR were monitored and optimized during the synthesis of the catalysts.

Spectra on solids were collected with a Varian CARY 5000 from Agilent equipped with an integrating sphere. The spectra were registered diffuse reflectance and the signal processed using the Kubelka-Munk[82] equation (2.2). These measurements were performed for those samples showing high scattering in solution.

$$F(R_\infty) = \frac{K}{S} = \frac{(1 - R_\infty)^2}{2R_\infty} \qquad \text{Eq. (2.2)}$$

Where $F(R_\infty)$ is the Kubelka-Munk function, K is the absorption coefficient and S is the scattering coefficient, R_∞ is the absolute reflectance assuming an infinitely thick layer. Being the scattering coefficient wavelength independent then the Kubelka-Munk function is proportional to K and it gives a good approximation of the absorption spectra[83,84].

2.4 Thermodynamic measurements

This section describes the procedure through which a group of experiments were designed to quantify the effect of the temperature on the reaction in the dark and under irradiation. For this first set of experiments, the kinetic analysis gave the values of the constant of reaction. The Eyring equation allowed to obtain the values of the activation energies of the dark and irradiated reactions.

2.4.1 Screening of the temperature

Reactions were run in a thermostatic bath set at different temperatures following the calibration line shown in **Figure 2.6** so that the temperature inside the reactor assumed values ranging from 0 to 48 °C. The reactions were run in the dark and under 130 mW laser irradiation at 532 nm for a maximum of 2 hours. The temperature inside the reactor was monitored with a thermocouple. The temperature was constant throughout the duration of the experiment showing variations below 1 °C.

A total of 10 reactions were run for the two conditions of illumination. The dark reactions were screened between 0 and 48 °C and the laser-irradiated ones between 0 and 36 °C, as reported in **Table 2.1**.

Table 2.1 temperature set points for the screening of reaction temperature for the reductive coupling of nitrobenzene.

Light conditions	Reaction T [°C]
Dark	0
	12
	25
	36
	48
130 mW 532 nm	0
	12
	18
	25
	36

The variations in concentration of the intermediate and product of the reaction were followed for up to 2 hours. A quantitative analysis was performed with GC following the procedure reported in Section 2.1.2.

2.4.2 Determination of kinetic constants of the first and second step of the reaction

The collected chromatograms were then processed with the software Matlab® and the concentrations of the components present in the reaction mixture were obtained applying Equation (2.1). Then, fitting the concentration of molecules **1**, **2**, and **3**, as a function of time, using the

equations (2.3-2.4-2.5) describing the kinetics of a consecutive reaction[85,86].

Applying a nonlinear least-square fit method, the kinetic constants for the first and second step of reaction showed in **Figure 2.8** were extrapolated.

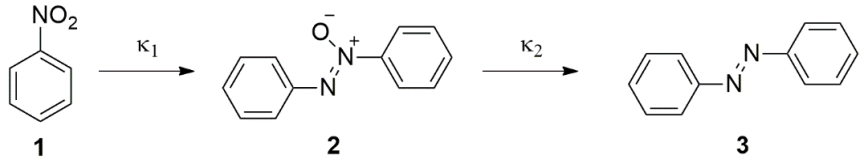

Figure 2.8 Nitrobenzene reductive coupling reaction steps and assignation of kinetic constants.

$$[1]_t = [1]_0\, e^{-k_1 t} \qquad \text{Eq. (2.3)}$$

$$[2]_t = \frac{[1]_0\, k_1}{k_2 - k_1}\ (e^{-k_1 t} - e^{-k_2 t}) \qquad \text{Eq. (2.4)}$$

$$[3]_t = [1]_0 \left\{1 + \frac{1}{k_1 - k_2}[k_2 e^{-k_1 t} - k_1 e^{-k_2 t}]\right\} \qquad \text{Eq. (2.5)}$$

Where k_1 and k_2 are respectively the kinetic constant of the first and second step of the reaction.

2.4.3 Determination of enthalpy of activation using the Eyring equation

As defined by the IUPAC gold book[87] "*the standard enthalpy of activation* $\Delta^{\ddagger}H^{\circ}$ *is the enthalpy change that appears in the thermodynamic form of the rate equation obtained from conventional transition state theory*". Therefore, the enthalpy of activation of an elementary reaction step is the energy difference between the transition state and the ground state of reagents.

The enthalpy of activation was determined by fitting the kinetic constants of the reaction in function of the inverse temperature. Indeed, the Eyring equation (2.6) describes the dependence of the kinetic constant of a reaction and the temperature.

$$k = \frac{k_B T}{h} e^{-\left(\frac{\Delta^{\ddagger}H^{\circ}}{RT} - \frac{\Delta^{\ddagger}S^{\circ}}{R}\right)} \qquad \text{Eq. (2.6)}$$

Where k is the kinetic constant of the elementary reaction, k_B is the Boltzmann, h is the Plank constant, and $\Delta G^{\ddagger}$ is the Gibbs energy of activation.

This equation, written in the linear form showed in equation (2.7), allows determining the enthalpy and entropy of activation for each step of the reaction under investigation simply by plotting the logarithm of the kinetic constant divided by the T as a function of 1/T.

$$\ln\frac{k}{T} = -\frac{\Delta^{\ddagger}H^{\circ}}{RT} + \frac{\Delta^{\ddagger}S^{\circ}}{R} + \ln\left(\frac{k_B}{h}\right) \qquad \text{Eq. (2.7)}$$

The comparison of the enthalpy of activation of the dark and irradiated experiment series allowed to draw preliminary conclusions on the effect of the laser on the kinetics and the yield of the reaction.

2.5 Arrangement of the experiments and data analysis methodology

To extend the understanding of how light affects the reaction through the interaction with plasmonic nanoparticles, a group of experiments was run systematically by applying the design of experiment principles (DoE). Collected data were processed and analysed to generate a model of the yield of reaction, as explained in section 2.5.2. This model aimed to shed light on the mechanism of activation of plasmonic catalysis. Briefly, a DoE was defined from a hypothesis, selecting the dependent variables to be modelled and the independent variables. The independent variables defined the experimental domain constituted by the upper and lower limits of all the variables under investigation.

2.5.1 Design of experiments

The yield of the reaction, expressed as a percentage, for azobenzene **3** and azoxybenzene **2** defined by equation (2.8) were chosen as dependent variables.

$$n\% = \frac{[n]_t}{[n]_{theor}} * 100 \qquad \text{Eq. (2.8)}$$

Where $[n]_t$ is the concentration of **2** or **3** at a certain time of the reaction and $[n]_{theor}$ is the theoretical yield if all the reagent was converted to the intermediate or the product.

The central hypothesis of this study was that the yields of **2** and **3** were strongly dependent on the kind of catalyst and the intensity of the lasers used. Another important hypothesis of this study was that the laser emitting light at 532 nm was affecting more the reaction outcome than the 785 nm laser regardless of the catalyst used.

Importantly, taking into account that the yield of any reaction is affected by time, the latter was also introduced in the group of independent variables of the experimental domain. The main characteristics of the DoE used in this work are summarised in **Table 2.2**.

Table 2.2 Hypothesis and variables limiting the definition for the design of experiment.

Hypothesis	**Depend. var.**	**Independ. var.**	**Exp domain**
*The yield of **3** and **2** depends mainly from 532 nm laser and time.*	Yield **2**% and Yield **3%**	Green Laser	16 – 130 mW
		NIR Laser	20 – 280 mW
		Time	0 – 120 min
		Catalyst type	AuNP or AuNP and AuNR

The other independent variables, such as concentration of the reactants, temperature and stirring rate, were kept constant for all the experiments, following the optimized reaction procedure described in detail in section 2.1.1.

The laser intensities were standardized applying equation (2.9)

$$z = \frac{X - \mu}{\delta\mu} \qquad \text{Eq. (2.9)}$$

Where, X is the variable to be converted, μ is its mean value and $\delta\mu$ is the difference between the maximum value of the variable and the mean value. The standardization of the variables allows comparing the effect of the variables on the system just looking at the magnitude of the values of

the estimated coefficients of the model. Valid only when variables are set as numerical.

The experiments were arranged applying a three-level full factorial design for two variables, generating 3^2 different experiments as shown in **Figure 2.9**. For designed experiments, the proper arrangement of the factor (the independent variable) settings allows determining the influence of the variation of each factor on the response when there is a simultaneous variation of all the other factors[53].

The central experiment was repeated at least 3 times to check for the curvature of the model and to have an estimation of the error.

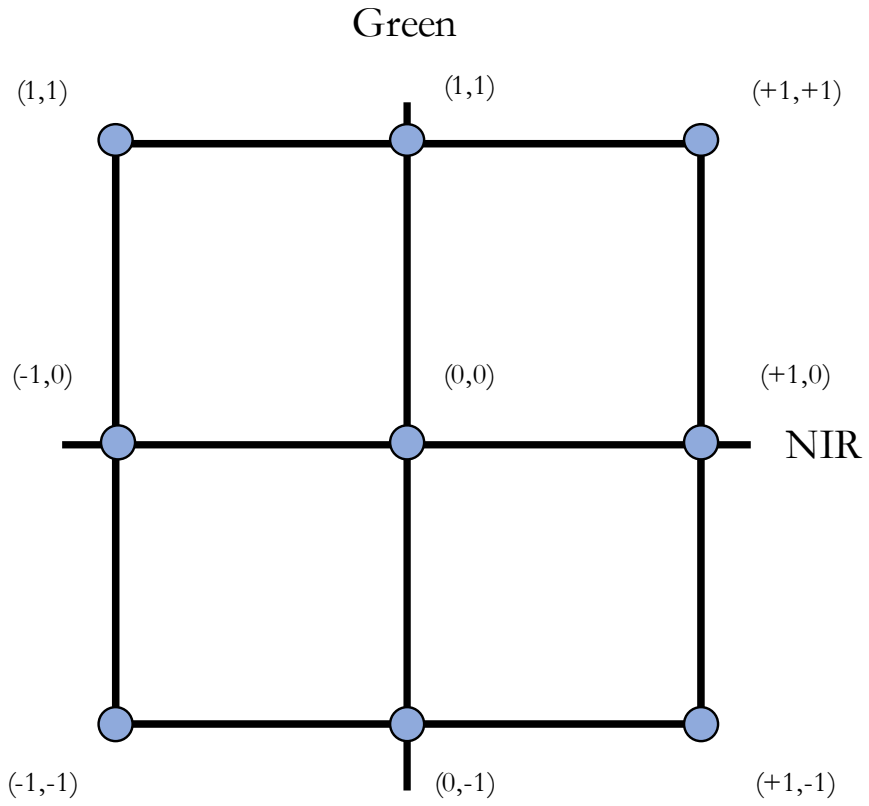

Figure 2.9 Graphical representation of the experimental domain where variables were standardized.

The experiments were performed following a random order as shown in **Table 2.3** to ensure minimization of systematic errors and time-dependent errors[88].

Table 2.3 Random run order and laser intensities for three-level full factorial design. The laser intensities were converted to standardized variables varying from -1 to +1.

Reaction ID	Order	Green [mW]	NIR [mW]	Green STD	NIR STD
1	5	16	28	-1	-1
2	11	16	154	-1	0
3	2	16	280	-1	1
4	1	73	28	0	-1
5	7	73	154	0	0
6	6	73	280	0	1
7	8	130	28	1	-1
8	12	130	154	1	0
9	9	130	280	1	1
10	10	73	154	0	0
11	3	73	154	0	0
12	4	73	154	0	0

Each reaction was monitored during two hours by analysing samples with GC. Typically, samples were collected at 0, 5, 10 ,15, 30, 60, 90, and 120 minutes for each reaction. The workup and analysis of the sample were performed as described in section 2.1.2.

Data were processed using the software Matlab to calculate concentrations and yield of the reaction.

2.5.2 Generalized linear mixed effect models for azoxybenzene and azobenzene yields

Linear models (LM) can be represented in the matrix form by equation (2.10) This approach is widely used for producing response surface models in chemistry.

$$\boldsymbol{y} = \boldsymbol{X\beta} + \boldsymbol{\epsilon} \qquad \text{Eq. (2.10)}$$

where $\boldsymbol{y}$ is the modelled variable vector and $\boldsymbol{X}$ is the model predictors matrix and β is the matrix of the unknown model coefficients, respectively.

The fundamental assumptions of linear models are:

- The linearity of the residuals of the model. The mean value and the standard deviation must be zero, meaning the residuals have a random distribution around zero.
- Absence of collinearity of the independent variables of the model. The variables are not correlated.
- Homoskedasticity; the variance of the data should be approximately equal across the range of the predicted values. This feature is reflected in the absence of pattern in the residual plot.
- Independence is ensured as long as each datum point comes from one and only one experiment.

In the case reported in this work, a simple linear model including also time-series measurements would have violated the independence assumption.

For this reason, a generalized linear mixed effect model[89,90] (GLME) was selected to analyse the data obtained from the designed experiments to assess the effect of laser intensity, time, and type of catalyst exerted on the yield of compounds **2** and **3**. The general equation of such kind of models is represented by equation (2.11)

$$\boldsymbol{\eta = X\beta + Zb} \qquad \text{Eq. (2.11)}$$

The above equation is analogous to equation (2.10) where $\boldsymbol{\eta}$ is a linear predictor of the dependent variable, $\boldsymbol{Z}$ is the design matrix for the random effects and $\boldsymbol{b}$ is a vector of random effects.

The difference between an LME (linear mixed effect) and a GLME lies in that the distribution of the observations $\boldsymbol{y}$, the dependent variable, does not need to be Gaussian. Indeed, one of the assumptions of this approach is that the dependent variable follows a distribution of a known family (binomial, Poisson, gamma, exponential, gaussian, etc.). Moreover, with GLME a link function is defined such that $\boldsymbol{\eta}$ is given by equation (2.12)

$$\boldsymbol{\eta} = g(\boldsymbol{\mu}|\mathbf{b}) \qquad \text{Eq. (2.12)}$$

Where, g is the link function, $\boldsymbol{\mu}|\mathbf{b}$ is the conditional expectation of the observations given **b**, the random effect.

$$E(\boldsymbol{Y}|\boldsymbol{b}) = \mu = g^{-1}(\boldsymbol{X\beta} + \boldsymbol{Zb}) \qquad \text{Eq. (2.13)}$$

The expected mean values μ of the estimator of the dependent variable y, *whose distribution is defined by the random effect variable*, is given by the inverse of the link function of the linear model, equation (2.13). Therefore, when working with GLME we fit the linear model to the link function g, not directly to the data.

For the sake of comprehension, it is necessary to outline the main difference of approach between a LM (Gaussian distribution and no random effects) and a GLME (any probability distribution and random effects). Two datasets are represented in **Figure 2.10**, where each symbol corresponds to a measurement and each colour represents an experiment. If we want to build a model using a linear model, then we are forced to consider only one measurement for each experiment, for instance, the yield at 1 hour of reaction to not break the fundamental assumptions of LM. In this case, we would have 9 points to estimate the coefficients of the model.

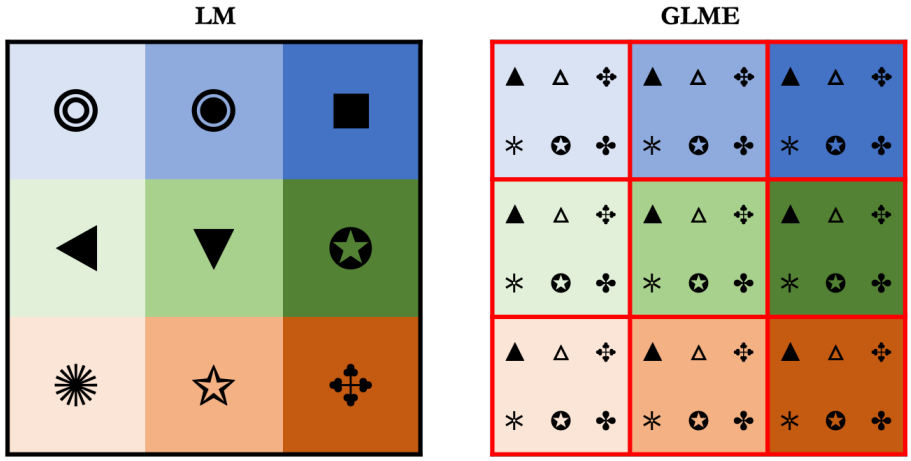

Figure 2.10 Sketch representing the difference between a linear model and a linear mixed effect model. Symbols represent a measurement; colours the single experiment and red lines define the random effect between experiments.

To ensure the independence of data, the GLME can process multiple responses from the same experiment, such as kinetic data, just by introducing random effects within each experiment. The random effect of the GLME is defined by the red borders that include data coming from a single experiment or repetitions. This feature allows manipulating much more data points than a LM allowing to explore the interaction of time with the other variables of the design.

Once the experiments designed in section 0 were run, the concentrations of the components of the reaction and the experimental conditions were processed with the software R-studio. The time and laser intensity variables were converted, when necessary, to standardized variables, as shown in equation (2.9). Models containing factors up to the second degree and mixed terms were considered in this work. To ensure the linearity of the yield for azobenzene, a logarithmic transformation was performed on the dependent variable. Randomization within each

experiment was introduced in the model, as well as within repeated experiments.

2.5.3 Model validation

The selection of the model describing the dependency of the production of **3** and **2** was done following the scheme of **Figure 2.11**. The models were built by adding one factor at a time and by comparing the new model with the previous through the analysis of variance. The ANOVA test produced the Akaike[91] number and p-value for the model. The Akaike number expresses the goodness of the fit.

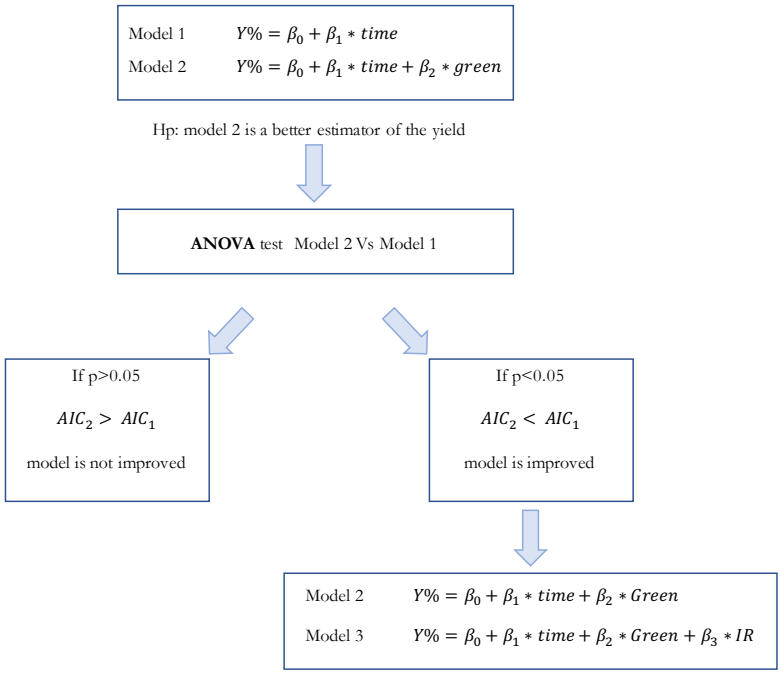

Figure 2.11 Flow diagram showing the strategy applied to select a model. Example of a linear model where no random effects are introduced.

The significance of each factor for a model was evaluated observing the p-values with a significance level of 0.05. The p-value tests the null hypothesis: the coefficient of the factor of the model equals zero. The smaller the p-value the more the factor is statistically significant for describing the dependent variable

Once appropriate models were selected for azobenzene and azoxybenzene, additional validation tests were run. A contrast matrix was built to test the null hypothesis, i.e. two factors have the same effect on the estimated values of the model. In other words, the contrast matrix allows to focus on the effect within the levels of a factor as well as between factors of the model and drive conclusion about which laser intensity or laser type makes a difference for the estimation of the dependent variable respectively.

Additional reactions were run to check the predictivity of the model. Reactions were run at intermediate levels of both lasers. Experimental values of the yields of azobenzene and azoxybenzene were compared with the predicted values.

3 Synthesis and optimization of the plasmonic catalyst

At the beginning of this work, the performance of a standard catalyst for the test reaction was measured. The catalyst composed by AuNP supported on TiO_2 nanoparticles, was purchased from Haruta Gold Inc and used as received (Lot. No. YS0D916A). This catalyst was defined by the World Gold Council as a benchmark catalyst to be used to compare the activity of other catalysts for oxidation and reduction reactions[52].

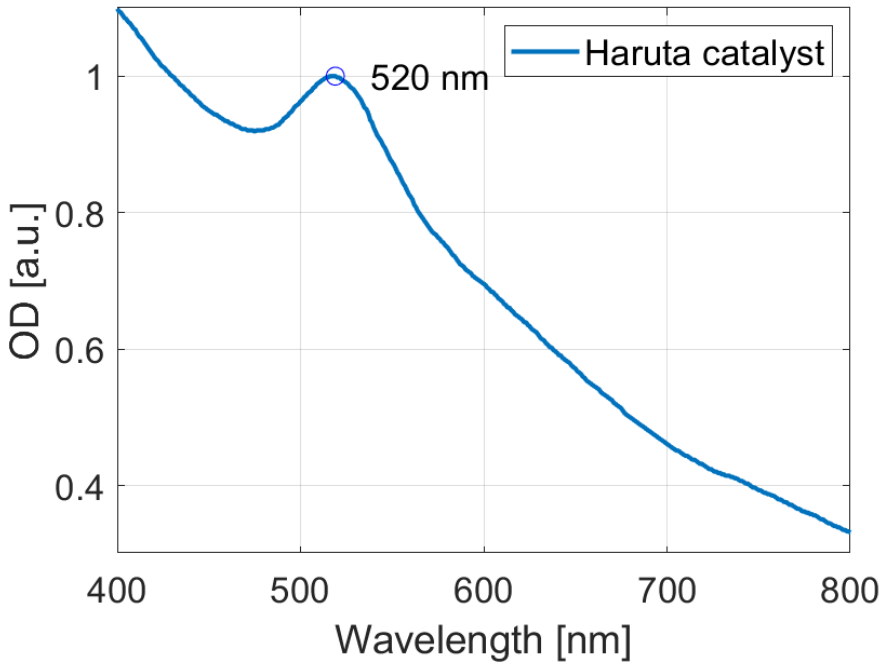

Figure 3.1 Normalized Visible spectra of the Haruta catalyst.

The AuNP size of Haruta catalyst was 4.11 ± 2.2 nm, Au load 0.96%$_W$ and the plasmon peak was centred at 520 nm as shown in **Figure 3.1**.

The catalyst showed very poor activity in the reaction conditions, only traces of the desired reaction product, azobenzene, was detected even after a prolonged time at 40 °C, **Table 3.1**. The catalyst allowed to convert nitrobenzene to azoxybenzene in moderate yield but did not show significant activity under light irradiation.

Table 3.1 Test reaction performed with the Haruta catalyst under dark and under laser irradiation conditions.

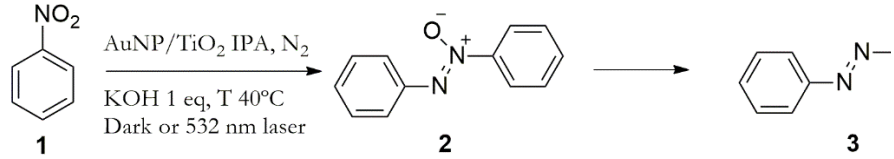

Entry*	I_{532nm} [mW]	Y_2% [mol%]	Y_3% [mol%]	TOF^a [h^{-1}]	Φ^b [mol/ph]
1	0	44.7	2.7	339	0
2	130	47.6	2.6	319	0

* Reaction conditions: temperature 40 °C, catalyst 50 mg, 0.1 mmol nitrobenzene, 0.1 mmol KOH, nitrogen flow. Yield measured at 24 hours.
[a] TOF calculated as the ratio of moles of 3 over the moles of AuNPs over time.
[b] quantum yield, ratio between product molecules and emitted photons.
AuNP: gold nanoparticles. TOF: turnover frequency.

The Haruta catalyst showed very low reactivity and poor yield in our reaction. The effect of light, (entry 2, **Table 3.1**) was negligible if compared with the control reaction, (entry 1, **Table 3.1**).

The turnover frequency was defined by equation (3.1) and (3.2).

$$TOF = \frac{mol_x}{mol_P * t} \qquad \text{Eq. (3.1)}$$

$$mol_P = \frac{N_P}{N_A} \qquad \text{Eq. (3.2)}$$

Where mol_x are the moles of azobenzene **3** or azoxybenzene **2**, t is the time of reaction, and mol_P are the moles of catalyst, defined by equation (3.2) as the ratio of the total number of particles in the reaction N_P over the Avogadro number N_A.

The apparent quantum yield in equation (3.3) was chosen to evaluate the efficiency of the different catalysts synthesised in this work. Considered that the percentage of photons absorbable by an inorganic oxide powder, such as SiO_2 or TiO_2, ranges from 50 to 65%[92], the determination of the actual absorbed light by the catalyst particles in the reaction mixture goes beyond the scope of this work being particularly difficult when dealing with solids dispersed in a liquid because of the high scattering of the media.

$$\Phi = \frac{\Delta n_x}{n_\gamma} \qquad \text{Eq. (3.3)}$$

Where the number of molecules Δn_x is the difference between the number of product or intermediate molecules generated under illumination and in the dark, and n_γ is the number of photons emitted by the laser source during the irradiation time. To be conservative, we assumed that, in our reaction conditions, the light was totally absorbed by the gold nanoparticles.

This preliminary results on the Haruta catalyst stimulated us to improve the performance of supported plasmonic AuNPs by investigating the influence that different synthetic procedures and kind of support could have on the activity of the catalyst[80,93].

Particular focus was directed towards tuning the size of the particles to maximize the absorption of visible light and the amount of plasmon-generated energetic electrons. Moreover, the selection of a support material that could ensure a stable and narrow particle size distribution of AuNPs was also investigated. The results of this investigation are discussed in the following sections.

3.1 Colloidal spherical gold nanoparticles

Gold Chloride trihydrate ($HAuCl_4 \cdot 3\ H_2O$) and sodium citrate were purchased from Merck and used without further purification.

The synthesis of spherical gold nanoparticles was performed by modifying the Frens method[94]. Briefly, 50 mL of a solution of Au(III) chloride hydrate 1.0 mM was refluxed under vigorous stirring. Subsequently, 5 mL of sodium citrate tribasic dihydrate solution 6.8 mM

was rapidly added with a pipette. AuNPs formed within 90 seconds as a result of the redox reaction between Au(III) and sodium citrate. The excess of sodium citrate contributed to the stabilization of the particles through adsorption on the surface. The citrate anions ensured the repulsion between the nanoparticles[95,96].

The obtained colloid was then left under stirring, cooled to room temperature, and stored in a glass flask. Typically, a UV-vis spectrum was acquired at the end of the synthesis to check the position of the plasmon peak. SEM images were acquired to determine the particle size as reported in **Figure 3.2**.

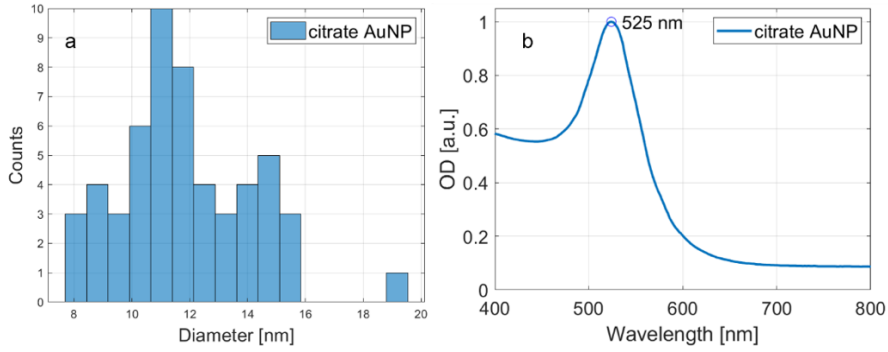

Figure 3.2 a. particle size distribution, and **b.** normalized UV-Vis spectra of citrate stabilized gold nanoparticles (AuNP).

Particle size was measured over more than 100 particles from SEM images. The sample showed a wide distribution with a mean particle size of 11.8 ± 2.3 nm. The synthetic protocol was optimized to obtain a size ranging from 10 to 20 nm. As suggested by Govorov *et al.*[97], particles in that particular range should be characterized by the generation of hot electrons with large energies.

Considering the reduction of $HAuCl_4^-$ as quantitative, the AuNPs concentration in the crude reaction mixture was $1.9 * 10^{-8}\ M$ and their molar extinction coefficient was $1.6 * 10^8\ M^{-1}cm^{-1}$. AuNPs showed a very high absorption at 525 nm.

The first series of experiments focussed on the synthesis of a catalyst constituted by colloidal AuNPs supported on silica particles. The surface of the silica particles was modified with (3-Aminopropyl)trimethoxysilane (APTES). Amine groups are well known for showing an affinity for gold surfaces and are widely used for the formation of self-assembled monolayers, an adhesion of substrates through electrostatic interaction[98,99].

The aminated silicon dioxide particles were synthesised from tetraethoxysilane (TEOS) and functionalized with (3-Aminopropyl)trimethoxysilane (APTES) following an optimized protocol[100,101]. Briefly, in a round bottom flask 55.5 g of ethanol, 13.80 g of Milli-Q water, and 5.93 g of ammonium hydroxide solution 29% were stirred at 40 ºC. Then, 6.15 g of TEOS was diluted in 5 mL of ethanol, preheated to 40 ºC, and added in one-pot to the stirring mixture. After 2.5 h, an additional 4 g of TEOS was added likewise and the reaction mixture was stirred overnight. The solid was then centrifuged and dispersed in ethanol at least 5 times to remove unreacted TEOS and ammonium hydroxide and then processed to functionalize the surface with APTES. The solid was dispersed in 63.12 g ethanol, sonicated for 1 hour, and then heated under stirring at 75 ºC in a two-necked round bottom flask provided with an addition funnel containing a solution of 1 g Milli-Q water, 0.09 g NH_4OH, and 0.354 g APTES. The mixture was stirred for 3 hours and was then cooled down to room temperature and

left stirring to provide nanoparticles with a narrow particle size distribution and mean value of 240 ± 8 nm, (**Figure 3.3** b). Finally, the suspension was centrifuged and washed in ethanol several times and then stored in 50 mL water.

To obtain a high number of gold particles per silica particles, the AuNP nominal load on the support was 7 $\%_w$. The procedure consisted in slowly adding the AuNPs to a 0.5 mg/mL suspension of the support under stirring. The resulting material was filtered and washed with water. The recovered solid was dried in an oven at 110 ºC.

The dilution of AuNPs and the presence of amine functional groups on the surface of the silica particles displaced the citrate molecules and allowed the deposition of AuNPs on the surface.

The supported AuNP catalyst (AuNP/SiO_2) was characterized with SEM microscopy and UV-visible spectroscopy. AuNPs showed a plasmon peak centred at 530 nm. The small red shift in the spectrum of the final product was due to the high refractive index of silica.

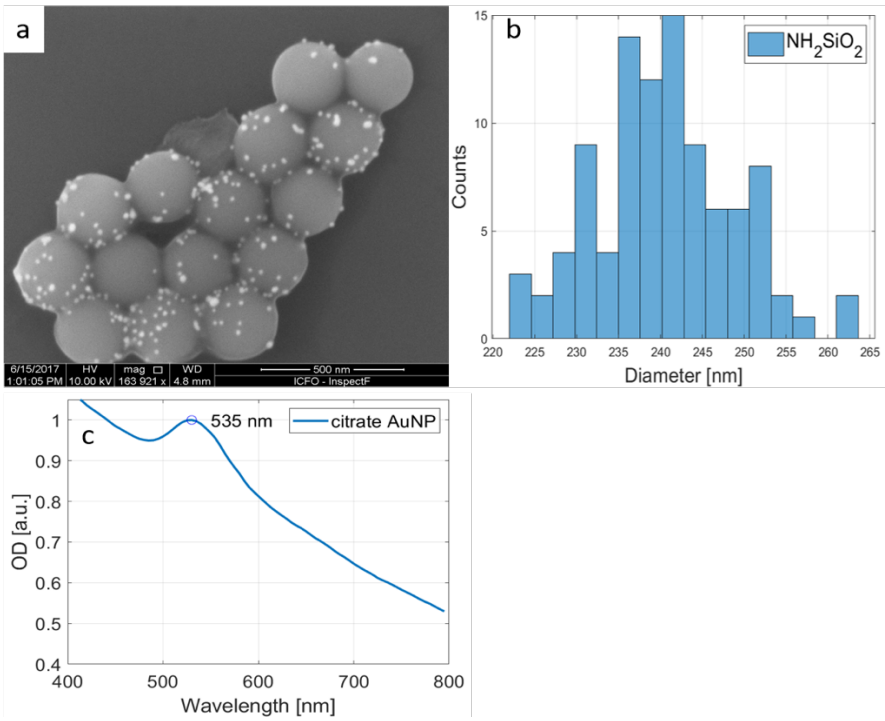

Figure 3.3 a. SEM image and **b.** particle size distribution of synthesised SiO_2. **c.** Normalized UV-Vis spectrum of AuNP/SiO_2 catalyst.

The actual gold load was measured with ICP-OES and provided a value of 5.60 $\%_w$.

The AuNP/SiO_2 catalyst was tested for the reduction of nitrobenzene under dark and under irradiation with 532 nm laser at 130 mW. The results are reported in **Table 3.2**.

Table 3.2 Catalytic test for AuNP/SiO_2.

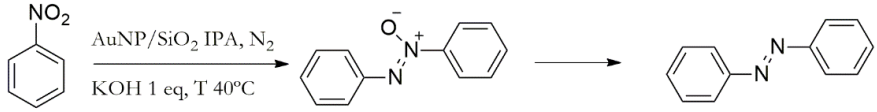

1 2 3

Entry*	I_{532} [mW]	Y_2% [mol%]	TOF[a] $10^4[h^{-1}]$	Φ^b $10^{-4}[mol/ph]$
3*	0	28.6	2.6	0
4*	130	32.3	2.9	4.5

*Conditions: 0.3 mmol of 1, 0.3 mmol of KOH, 30 mg AuNP/SiO_2 corresponding to 8 μmol Au, 2 ml isopropanol, 0.05 mmol naphthalene, N_2 flow, laser intensity 130 mW, T = 40 °C, yield registered at 2 hours with GC and internal standard.
[a] TOF calculated as the ratio in moles of 2 over AuNPs over time.
[b] Quantum yield, ratio between product molecules and emitted photons.
AuNP: gold nanoparticles. TOF: turnover frequency.

The laser-irradiated reaction showed an 3.7% increase in the production of azoxybenzene **2** after two hours. However, the desired product of reaction, **3**, could not be detected, not even after prolonging the reaction time to 24 hours. Control reactions containing only the support and only the reactants yielded no conversion.

The catalyst was recovered and analysed after 2 hours of reaction with SEM and UV-Vis spectroscopy, **Figure 3.4**.

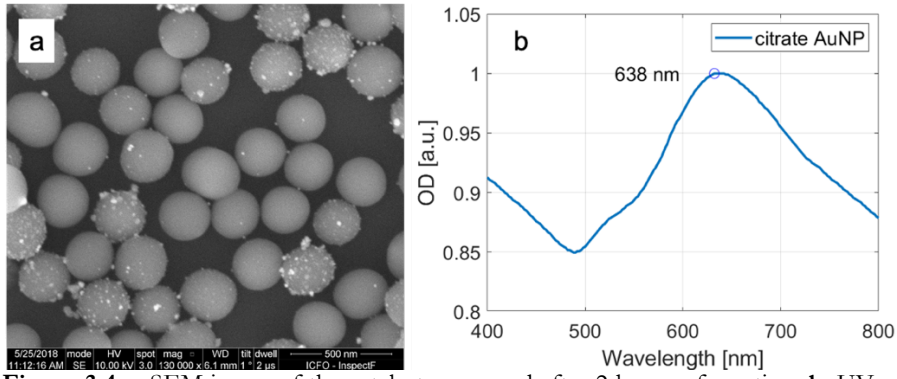

Figure 3.4 a. SEM image of the catalyst recovered after 2 hours of reaction. **b**. UV-Vis spectra of the recovered catalyst. The peak at 638 nm indicates aggregation of the AuNP.

The catalyst showed poor resistance to the reaction conditions because of the presence of KOH. The strong base partially dissolved the acidic SiO_2 particles causing the detachment of AuNPs, which eventually aggregated and lost their catalytic activity. As a consequence, a red shift of the plasmon peak was observed, which contributed to lower the intensity of absorption at the irradiation wavelength of 532 nm.

Considering those preliminary results, the synthesis of spherical AuNPs was oriented towards the *in situ* generation of nanoparticles that could form a final material with a higher stability[80,102]. The stability problem related to the AuNP/SiO_2 catalyst could not be solved either by changing the synthetic method. Although the in-situ approach afforded smaller AuNPs, the stability of the catalyst was still poor in the reaction conditions.

To improve the performance of plasmonic catalysts under laser light irradiation, two methods were investigated to generate AuNPs on the surface of selected metal oxide supports (TiO_2, Fe_2O_3, and CeO_2). The first relied on the reduction with sodium borohydride ($NaBH_4$) of a

chloroauric acid solution in the presence of the metal oxide support. The second method applied was a modification of the Haruta method[93,103,104].

3.2 Deposition-precipitation method, in-situ gold reduction

$NaBH_4$, $HAuCl_4 \cdot 3\ H_2O$, titanium dioxide, and iron(III) oxide were purchased from Merck, cerium(IV) dioxide was purchased from STREM CHEMICALS, and titanium dioxide aeroxide P25 was purchased from EVONIK. All the chemicals were used without further purification.

The deposition-precipitation method was used to deposit gold on different supports and to obtain a set of particle sizes spanning from 20 nm to 3.1 nm. The reduction of the Au(III) precursor was performed either by adding $NaBH_4$ to the reaction mixture or through thermal decomposition of the Au(III) species adsorbed on the support.

3.2.1 Reduction in solution with $NaBH_4$

The typical procedure consisted in dissolving 40.8 mg of $HAuCl_4 \cdot 3\ H_2O$ in 26 mL Milli-Q water in a three-necked round bottom flask. The pH was then slowly raised to pH = 8 with NaOH 0.1 M and the solution was left stirring for 1.5 hours at a temperature of 70 °C. The pH was monitored and kept at the desired value during all the process. Subsequently, 1 g of metal oxide powder was mortar-crushed and slowly

added to the solution under vigorous stirring. Finally, 2 mg of $NaBH_4$ dissolved in 50 mL Milli-Q water was prepared and added with a dropping funnel connected to one of the necks of the round bottom flask over 30 minutes. The reaction mixture was left stirring 1 hour at 70 °C and was then cooled down naturally to room temperature and stirred overnight. The resulting solid was vacuum filtered with a Buchner funnel provided with a 0.2 μm membrane filter and was washed with water until the filtrate reached a neutral pH and was negative on a test for Cl^- ions (performed with a $AgNO_3$ solution).

The material was then collected in a crystallization dish and was dried under open-air at 80 °C overnight. Then, it was calcined in a furnace under open-air at 350 °C for 3 to 4 hours with a ramp of 10 °C/min, except for catalyst 322 (entry11-12) that was just dried at 110 °C. All materials were stored in a dark cool place in a vial.

With this procedure, four catalysts, characterized by different AuNP sizes and kind of support were synthesised (**Table 3.3**).

The catalytic tests were performed reproducing the same conditions used for the Haruta catalyst experiments. A comparison between their performance and the one from the Haruta catalysts is reported in **Table 3.3**. The TOF was calculated applying equation (3.1); through this value, the activities of the different catalysts were compared considering the moles of AuNPs instead of the moles of Au. The size of the metal nanoparticles and, consequently, their molecular weight, varied significantly between each catalyst. The quantum yield was calculated with equation (3.3) to estimate the effect that light, compared to dark conditions, had on the reaction.

Table 3.3 Catalytic test for the study of the effect of the support and AuNP

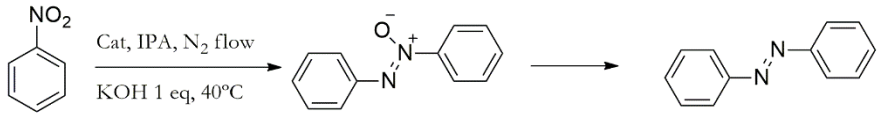

1 2 3

Entry*	AuNP[a] [nm]	Supp.	I_{532} [mW]	Y_2 [mol%]	Y_3 [mol%]	TOF^b [h^{-1}]	ϕ^c 10^{-4} [mol/ph]
1[d]	4.11	TiO_2	0	44,7	2,7	339	0
2[d]	4.11	TiO_2	130	47,6	2,6	319	0
5[e]	5.4	Fe_2O_3	0	18,5	0	0	0
6[e]	5.4	Fe_2O_3	130	26,7	0,4	15	0.04
7	3.86	CeO_2	0	23,8	2,5	14	0
8	3.86	CeO_2	130	50	5,8	66	0.33
9	6.5	1-TiO_2[g]	0	50,5	0,9	23	0
10[f]	6.5	1-TiO_2[g]	130	56,7	5,6	412	0.63
11	6.7	2-TiO_2[g]	0	75.7	17.3	583	0
12	6.7	2-TiO_2[g]	130	63.7	30	1204	1.33

*Conditions: 0.1 mmol of 1, 0.1 mmol KOH, 3 μmol Au, 2mL isopropanol, 0.05 mmol naphthalene, N_2 flow, laser intensity 130 mW, T = 40 °C. The yields of azoxybenzene 2 and azobenzene 3 were registered at 24 hours with GC by using an internal standard.
[a] Size of the particles obtained by measuring over 100 AuNP in TEM or SEM images.
[b] TOF calculated as the ratio in moles of product 3 over AuNP over time.
[c] Quantum yield, ratio between the number of product molecules and emitted photons.
[d] Haruta catalyst 2 hours of reaction.
[e] 8 μmol Au.
[f] 18 hours of reaction.
[g]. TiO_2 Anatase phase from Merck, the number refers to the batch of catalyst.
AuNP: gold nanoparticles. GC: gas chromatography. SEM: scanning electron microscopy. TEM: transmission electron microscopy.

All the reactions were run by introducing the same amount of gold, except for entries 5 and 6, where the amount needed to observe any reactivity of the AuNP/Fe_2O_3 catalyst was 160% more than the quantity

used in the rest of the experiments. In this case, only traces of the product of reaction, **3**, were detected. Entries 7 and 8 show that, for the AuNP/CeO_2 catalyst, the TOF was still very low if compared with the results of the Haruta catalyst (entries 1 and 2). Because of the yield difference between the dark and irradiated reactions, the quantum yield was $0.33 * 10^{-4}$. The use of TiO_2 anatase phase in entries 9 to 12 displayed the best performance. Even if the active surface of the catalyst used in entry 9 was smaller than the surface of the Haruta catalyst (greater mean particle size), the former performed better under irradiation. Indeed, the dark reaction in entry 9 yielded only 0.9% of azobenzene **3** while under irradiation was registered a 5.6 % yield (entry 10). Entries 11 and 12 are the results obtained with 2-Au/TiO_2 for which the highest TOF and ϕ were obtained.

Considering the results obtained with these different supports, a further investigation on the kind of TiO_2 support and the AuNP particle size was undertaken. The objective of this investigation was to determine which oxide between TiO_2 anatase or TiO_2 P25 could constitute the best catalyst and which particle size could give the highest quantum efficiency.

3.2.2 Thermal decomposition of gold(III) precursor to gold(0)

Two batches of AuNP/TiO_2 were synthesised using the deposition-precipitation method choosing titanium dioxide P25 from EVONIK as support. This material is constituted by a mixture of 80% anatase and 20% rutile. This method allowed to obtain two catalysts named 4-

AuNP/TiO_2 and 5-AuNP/TiO_2 with the smallest particle size amongst all the synthesised catalysts.

The Haruta method was optimized to obtain the catalyst that showed the highest activity under 532 nm laser irradiation. Therefore, this section describes the optimization of the synthesis of catalysts composed by AuNPs on TiO_2. The supports used were TiO_2 nanopowders purchased from Merck or EVONIK.

The typical synthetic procedure for the production of 1 g of catalyst consisted in dissolving 32.5 mg of $HAuCl_4 \cdot 3\ H_2O$ in 250 mL Milli-Q water under stirring at 70 °C. Then, 1 g of the TiO_2 supported nanoparticles were slowly added and the pH was raised and maintained with NaOH 0.1 M at a fixed value ranging from 7 to 8. The suspension was then stirred for 2 hours at 1100 rpm. The suspension was then left to cool down to room temperature and then immediately vacuum filtered on a Buchner funnel provided with a 0.2 μm membrane filter. The cake was washed with water until the filtrate reached a neutral pH and was negative on a test for Cl^- ions (performed with $AgNO_3$ solution). The material obtained was collected in a crystallization beaker and dried in an oven at 80 °C overnight. Finally, the partially dry material was placed in a furnace and calcined in air at 350 °C for 3 to 4 hours with a ramp of 10 °C/min to reduce the Au(III) precursor species to Au(0)[105]. The catalyst obtained was left to cool down to room temperature and was mortar crushed and stored in a dark cool place in a glass vial.

The obtained catalysts were tested in the reductive coupling reaction of nitrobenzene. The results are reported in **Table 3.4**.

Table 3.4 Effect of the kind of TiO_2 support and AuNP size.

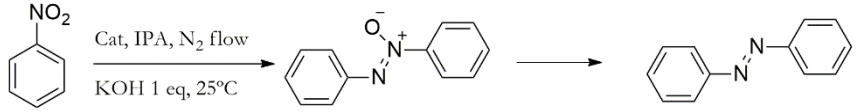

1 2 3

Entry*	Size[a] [nm]	Supp.	I_{532nm} [nm]	Y_2% [mol%]	Y_3% [mol%]	TOF^b [h^{-1}]	ϕ^c 10^{-3} [mol/ph]
13	3.1	4-TiO_2[e]	0	54,1	11,5	17031	0
14	3.1	4-TiO_2[e]	130	52.0	27,7	37301	3.9
15	3.5	5-TiO_2[e]	0	58.5	4	17353	0
16	3.5	5-TiO_2[e]	130	57.9	13.0	27445	2.2
17[d]	20	3-TiO_2[f]	0	42,2	59,6	15775	0
18[d]	20	3-TiO_2[f]	130	57,4	50,7	13425	0

*Conditions: 0.1 mmol of 1, 0.1 mmol KOH, 3 μmol Au, 2 mL isopropanol, 0.05 mmol naphthalene, N_2 flow, laser intensity 130 mW, T = 25 °C. The yields of azoxybenzene 2 and azobenzene 3 were registered at 1 hour with GC by using an internal standard.

[a] Size of the particles obtained by measuring over 100 AuNP in TEM or SEM images.

[b] TOF calculated as the ratio in moles of product 3 over AuNP over time.

[c] Quantum yield, ratio between the number of product molecules and emitted photons.

[d] 7 μmol Au, 72 h of reaction, T=40 °C.

[e] TiO_2 P25 from EVONIK.

[f] TiO_2 anatase from MERK.

AuNP: gold nanoparticles. GC: gas chromatography. SEM: scanning electron microscopy. TEM: transmission electron microscopy.

From the data reported in **Table 3.4**, the TOF as well as the ϕ are one order of magnitude higher than the values reported in **Table 3.3**. Both catalyst 4 and 5-AuNP/TiO_2 showed a high activity under illumination and were able to fully convert the reactant to the product within 2 hours. On the other hand, the dark reactions (entries 13 and 15) reached a maximum yield of 75% and 55% respectively after 24 hours. Catalyst 4-AuNP/TiO_2 was the most efficient catalyst under 532 nm laser irradiation, (entry 14). It can be noticed that a 13% increase of the particle size decreased by 43% the value of ϕ (compare entries 14 and 16).

Catalyst 3-AuNP/TiO_2 was synthesised with the method described in Section 3.2.1 and calcined at a higher temperature (500 °C for 4 hours) to cause the sintering[106] of the AuNP into bigger ones with an average size of 20 nm. Entries 17 and 18 show the results of the experiments with 3-AuNP/TiO_2; the catalyst was still able to convert **1** to the product of reaction **3** at the cost of longer reaction time (72 h). Importantly, the positive effect of the laser irradiation was not observed for this catalyst.

The characterization of the best performing catalyst, 4-AuNP/TiO_2 included the acquisition of its DR spectrum, TEM images, ICP-OES measurement of Au content, BET (Brunauer–Emmett–Teller) surface area, XPS, pXRD. The results are reported hereafter.

3.3 Characterization of catalyst 4-AuNP/TiO_2

Catalyst 4-AuNP/TiO_2 showed a gold load of 1.16 $\%_W$, TEM inspection revealed well dispersed and narrowly distributed AuNPs of average particle size 3.1 ± 0.8 nm. This was the smallest particle size achieved in this study (**Figure 3.5**).

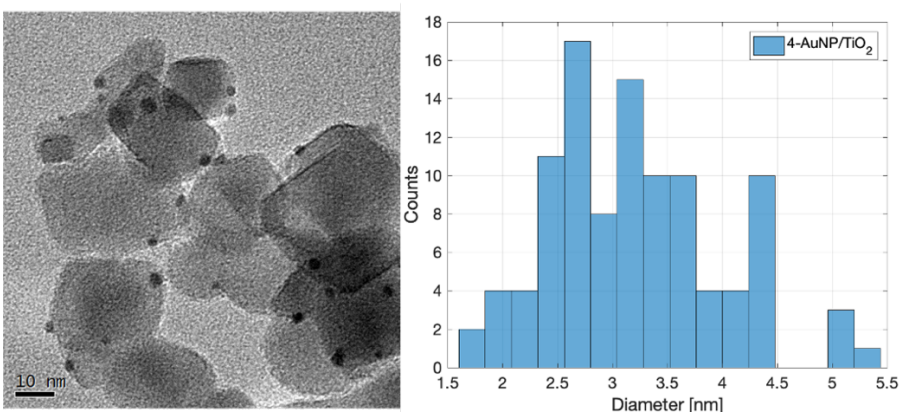

Figure 3.5 a. TEM image of catalyst 4-AuNP/TiO_2 **b**. Size distribution of AuNP on the TiO_2 surface over more than 100 nanoparticles.

The DR spectrum was acquired by registering the diffuse reflectance of the catalyst after being transformed into a tablet through the use of a hydraulic press. The tablet was placed in a spectrometer provided with an integration sphere and a reflectance spectrum was acquired. A matt Teflon reference was used to provide a nominal 100% reflectance measurement.

For crystalline solids with an indirect band gap, such as TiO_2, the dependence of the absorption coefficient K on the frequency $\mu\nu$ can be approximated as shown in equation (3.4)[83,107,108].

$$\mathrm{k}h\nu = \mathrm{A}(h\nu - E_g)^2 \qquad \text{Eq. (3.4)}$$

Where, k is the absorption coefficient, $h\nu$ is the energy of the photon A is a constant and E_g is the band gap energy of the semiconductor.

The band gap of the material E_g can be obtained by extrapolating to zero a linear fit to a plot of $(khv)^{1/2}$ against hv.

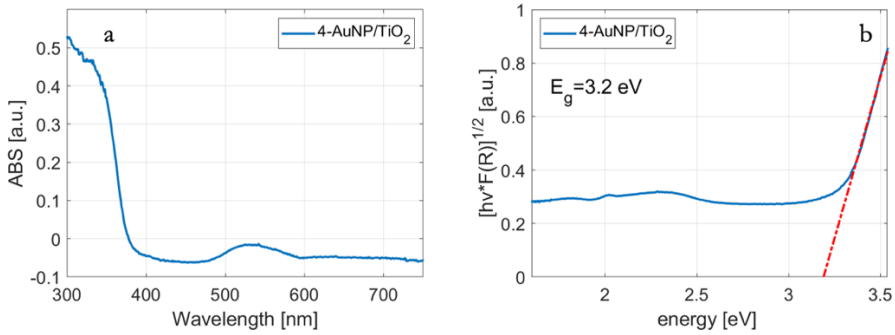

Figure 3.6 Optical properties of catalyst 4-Au/TiO_2. **a.** Absorption spectrum obtained from diffuse reflectance measurements applying the Kubelka-Munk equation. **b.** Kubelka function plot giving a band gap of 3.2 eV.

Applying the Kubelka-Munk equation (3.2) a signal proportional to the absorption spectra of the material was obtained (**Figure 3.6**-a). Absorption of small AuNP at 515 nm was evident in the sample along with the strong absorption of the support above 380 nm in the UV region. The band gap of the catalyst was extrapolated from the Kubelka function plot combining Eq. (2.2) and Eq. (3.4) into Eq. (3.5) to give the spectra shown in **Figure 3.6**-b.

$$(\mathrm{F}(\mathrm{R}_\infty) * \mathrm{h}\nu)^{\frac{1}{2}} = h\nu - E_g \qquad \text{Eq. (3.5)}$$

A band gap of 3.2 eV, the exact same value as the TiO_2 EVONIK P25[109] used for the synthesis of catalyst 4-AuNP/TiO_2 indicated that the

presence of the AuNPs did not influence significantly the position of the conduction and valence bands of the material.

BET surface area determination was performed by the CCiTUB service of the University of Barcelona. The measurement reported in **Table 3.5** showed that the specific surface of the final material had a reduction of 5.2 %.

Table 3.5 BET results for catalyst 4-AuNP/TiO_2 and TiO_2 support.

Sample	BET $[m^2 g^{-1}]$
TiO_2 P25	51.8153 m2/g
4-AuNP/TiO_2	49.1203 m2/g

The little variation between the surface area of catalyst 4-Au/TiO_2 and the support confirmed that the synthetic method was robust and that the material did not aggregate or changed its phase composition during the thermal treatment.

The XPS measurement of the catalyst confirmed the presence of gold in metallic state characterized by the peaks of Au 4f at 84 and 87.8 eV (**Figure 3.7**).

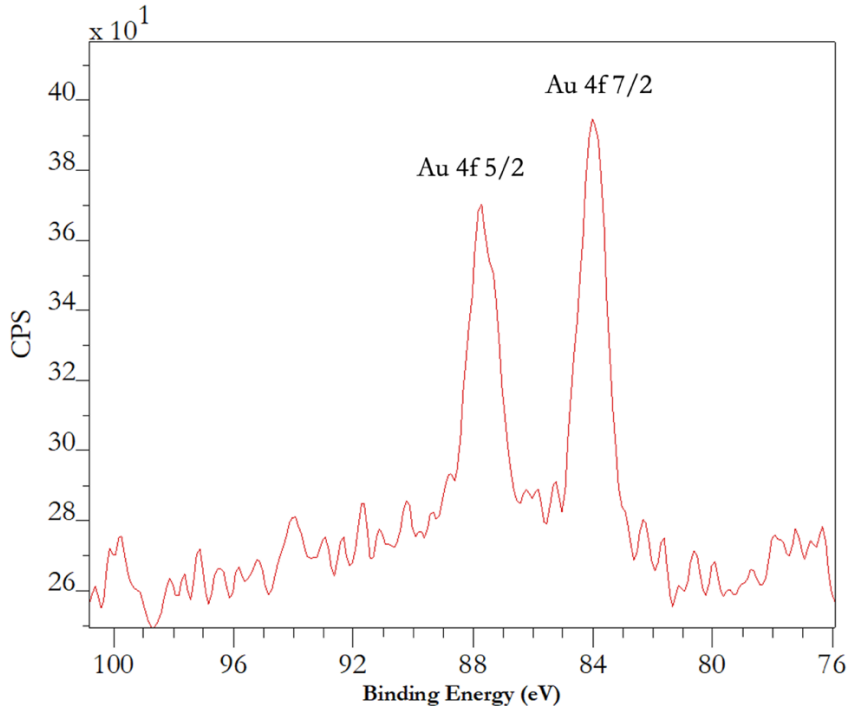

Figure 3.7 High-resolution XPS spectrum showing the Au 4f peaks.

The survey spectrum of the catalyst did not evidence contaminants, such as chlorine ions or organic molecules, in the catalyst.

The pXRD spectrum was processed with MATCH! software as shown in **Figure 3.8**.

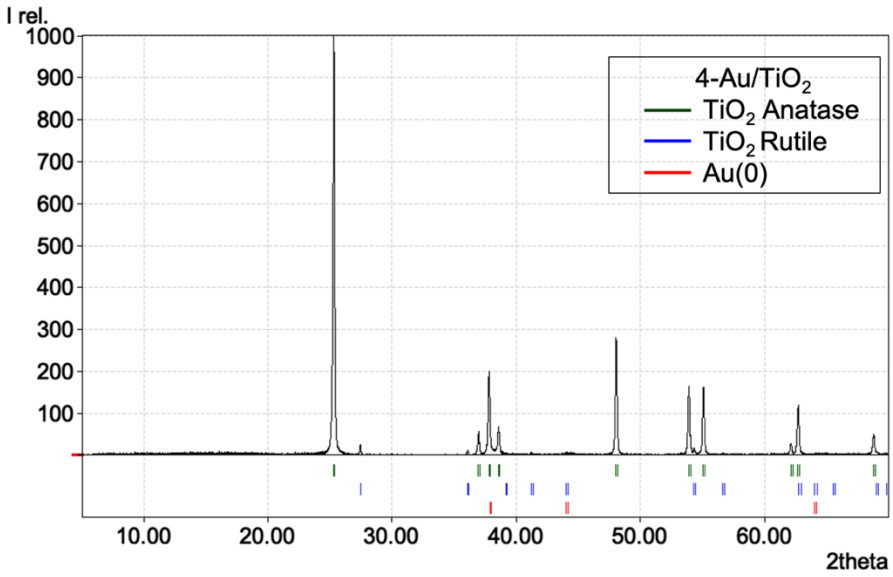

Figure 3.8 pXRD spectra of catalyst 4-Au/TiO_2 showing the presence of Au in the metallic state, as well as the crystalline phase of anatase and rutile TiO_2.

The pXRD data demonstrated that the thermal treatment of the catalyst did not modify the crystalline phase of the supporting material, as expected when thermal processes are run at temperatures below 600 °C[110,111].

3.4 Gold nanorods containing catalysts

Gold nanorods (AuNR) are anisotropic nanoparticles and are known for their heat generation when irradiated at the plasmon frequency in the visible and infrared region[44,65,112]

AuNRs were prepared in our group according to the procedure by Al-Sayed *et al.*[113] in-house. AuNRs were further processed to exchange the cetyltrimethylammonium bromide (CTAB) capping agent for the much softer and stabilizing sodium citrate, as described by Wei *et al.*[114]. The water colloid was obtained with an extinction coefficient of $2.6 * 10^9\ M^{-1}cm^{-1}$ and plasmon absorption centred at 716 nm.

To the best of our knowledge, there is no method to efficiently synthesise AuNRs directly on the surface of a support. This is due to the extreme sensitivity of the final shape of the particles to the presence of contaminants in solution and suspension[115,116].

Therefore, a simple method to deposit AuNR colloids on supports was developed. The method consisted in centrifuging several times 300 mL of the citrate-stabilized colloid (0.4 mg/mL of metallic gold) to decrease the sodium citrate concentration below 0.7 mM. Subsequently, the destabilized AuNRs were sonicated, 300 mL Milli-Q water was added to the colloid, and the mixture was then slowly added to a vigorously stirred suspension of the support TiO_2 or previously synthesised AuNP/TiO_2 catalyst (600 mL 1 mg/mL). This mixture was left stirring overnight and the suspension was vacuum filtered with a Buchner funnel provided with a 0.2 μm membrane filter connected to an Erlenmeyer flask and washed with 1.5 L Milli-Q water to remove the capping agent. The solid was then dried in an oven at 110 ºC overnight and was then cooled down to room temperature and mortar crushed.

This type of catalyst was designed with the aim of understanding if the thermoplasmonic effect generated by AuNRs could influence the

outcome of the reaction. The data collected in **Table 3.3** proves that the reaction is influenced by temperature.

We wanted to verify whether AuNRs resonating with a NIR laser emitting at 785 nm could trigger the reaction as efficiently as the 4-AuNP/TiO_2 catalyst or eventually act synergistically with the spherical AuNP catalyst.

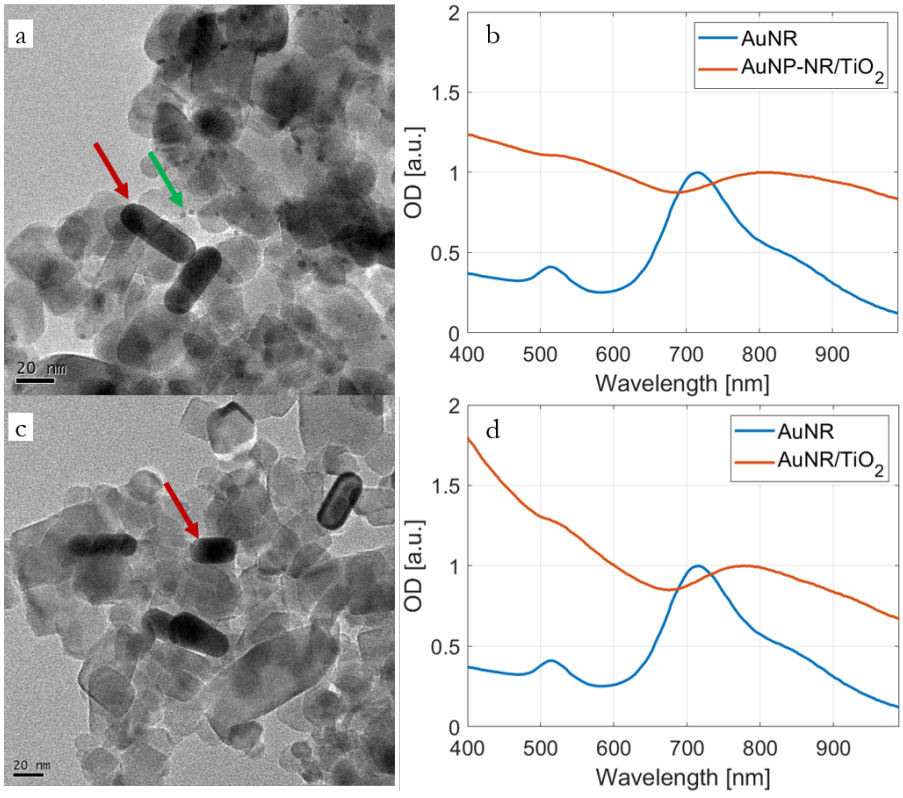

Figure 3.9 TEM images and visible spectra of AuNRs containing catalysts. **a.** TEM image of sample AuNP-NR/TiO_2 where two different kinds of nanoparticles were deposited on the support surface. **b.** Spectra of the starting material AuNR colloid and AuNP-NR/TiO_2 catalyst showing a red shift of the longitudinal plasmon. **c.** TEM image of sample AuNR/TiO_2 showing the presence of only cylindrical nanoparticles. **d.** Spectra of the starting material AuNR colloid and AuNR/TiO_2 catalyst showing a red shift of the longitudinal plasmon.

The average particle size was measured with 100 particles, resulting in cylindrical particles of 15 nm diameter and 45 nm length. The deposition process, along with the change in the refractive index in the surrounding of the AuNR[117], caused a red shift of the plasmon absorption peak from 716 nm (starting material) to 804 nm $(\Delta_\lambda = 88\,nm)$ for AuNP-NR/TiO_2 catalyst and $(\Delta_\lambda = 62\,nm)$ for AuNR/TiO_2.

The ICP-OES analysis gave a gold load of 10.7 $\%_W$ for the AuNR/TiO_2 catalyst containing only gold nanorods and 11.9$\%_W$ for AuNP-NR/TiO_2 characterized by the presence of spherical and cylindrical AuNPs on the surface of the support.

The capability of AuNRs to convert the 785 nm laser beam energy into thermal energy was tested by monitoring the temperature rise in the reactor during 5 hours of a suspension containing 10 mg AuNR/TiO_2 in 2mL IPA under irradiation at 320 mW.

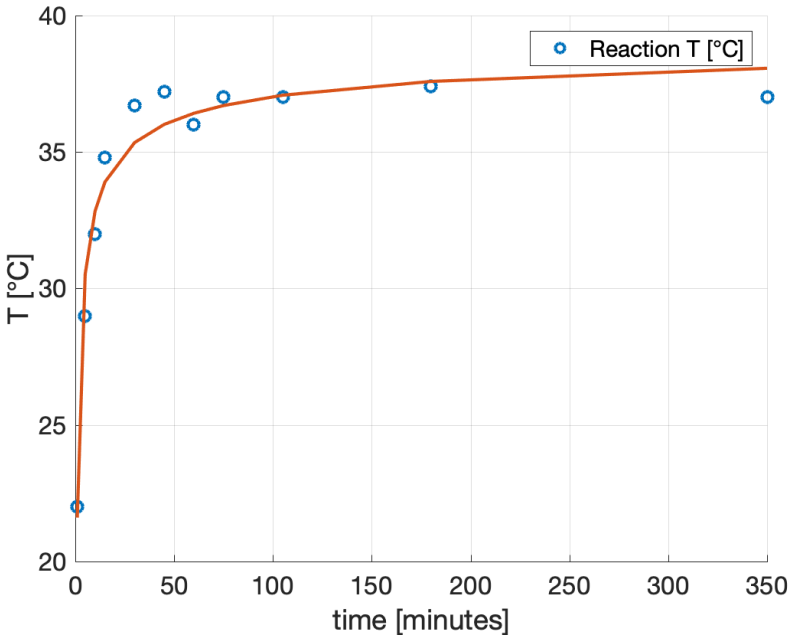

Figure 3.10 Temperature as a function of time for 10 mg AuNR/TiO_2 catalyst in 2 mL IPA under 785 nm laser irradiation at 320 mW. The temperature was monitored with a thermocouple placed inside the reactor. The reactor was positioned on the stirrer at room temperature, without a thermal bath.

Figure 3.10 shows that, in this conditions (without external cooling), the temperature rapidly increased within the first 30 minutes of irradiation to reach a stable value of 37 °C from the first hour on.

Few reactions were run screening different intensities for the 785 nm laser (from 30 to 280 mW) and increasing the amount of AuNR/TiO_2 catalyst to 50 mg. On average, a 5 % yield was registered, after 24 h of reaction, showing no correlation to the IR laser intensity.

When catalyst 4-AuNP-NR/TiO_2, synthesised from catalyst 4-AuNP/TiO_2, was used the yield of the reaction dropped compared to the

reactions run with the latter catalyst. However, a temperature increase of 15 °C was registered.

When inspecting catalyst 4-AuNP-NR/TiO_2 with TEM, an increase of the mean particle size from 3.1 to 3.6 nm was noticed. The activity of AuNPs strongly depends on the particle size[118,119]. In this case, the deposition procedure of AuNRs had a negative impact on the particle size distribution of the hemispherical NPs and, consequently, on the reactivity of the composite catalyst.

A group of reactions were run in the same conditions as for experiment 14 of Table 3.4, except for the introduction of a second laser source emitting light at 785 nm and the use of AuNR/TiO_2 as an additive to 4-AuNP/TiO_2 catalyst. The two different kinds of particles were characterized by different particle sizes and positions of the plasmon absorption. Thus, AuNPs absorb the 532 nm laser light while the AuNRs absorb mainly the 785 nm laser. Results are reported in **Table 3.6**.

Table 3.6 Study of the effect of AuNR/TiO_2 on the catalysis of 4-AuNR/TiO_2

Entry*	I_{532} [mW]	I_{785} [mW]	$Y_3\%$[a] [mol%]	TOF[b] $[10^4 h^{-1}]$	ϕ[c] $[10^{-3}]$
18	0	0	17.8	2.22	0
19	130	0	19.0	2.38	1.8
20	0	130	17	2.14	0
21	65	28	21	2.63	2.8
22	130	147	23.9	2.99	1.2
23	16	280	19	2.38	0.54

*Conditions: 0.1 mmol of **1**, 0.1 mmol KOH, 50 mg 4-Au/TiO_2, 10 mg AuNR/TiO_2, 2mL isopropanol, 0.05 mmol naphthalene, N_2 flow, variable laser intensity, T = 25 °C

[a] Yield of azobenzene registered at 1 hour with GC using an internal standard.

[b] TOF calculated as the ratio in moles of azobenzene **3** over AuNP over time.

[c] Quantum yield, ratio between the number of product molecules and total emitted photons considering both lasers.

AuNP: gold nanoparticles. GC: gas chromatography. TOF: turnover frequency.

An obvious effect of the 532 nm laser was observed in entry 19, resulting in a higher yield than entry 18 and 20. Irradiating the reaction with only the IR laser (entry 20) did not produce any yield enhancement compared to the dark reaction (entry 18). Combinations of different intensities for the green and infrared lasers suggested that the reaction was influenced by different magnitudes of the two lasers. Indeed, for the reaction described in entry 23, irradiating with the NIR laser at a high intensity of 280 mW resulted in the same yield as in entry 19. Furthermore, the quantum yield was just 30% of the value obtained for entry 19 indicating that the effect of the IR laser on the reaction was much smaller than the one of the green laser. The use of intermediate intensity values for both lasers in entries 21 and 22 allowed to reach higher yields. Concerning the quantum yield, the highest value was reached for laser intensities of 65 and 28 mW for green and IR lasers respectively (entry

21). Irradiating the reaction with higher intensities on both lasers did not increase the quantum yield (entry 22).

3.5 Enthalpy of activation quantifies the effect of light irradiation

Further investigation was warranted to quantify the influence of the irradiation with the 532 nm laser on AuNPs. Two groups of experiments were designed by using a fixed amount of 4-Au/TiO_2 catalyst. In a first set of reactions, the temperature was varied, within the limits imposed by the solvent used, in the dark. Then, the same experiments were run under irradiation with the 532 nm laser at a fixed intensity of 130 mW. The temperature was set at the desired setpoint (0 – 48 °C) throughout the duration of each experiment by submerging the reactor in a thermostatic bath. A thermocouple immersed in the reactor was used to monitor the temperature.

The reaction was characterized by the transformation of nitrobenzene **1** into an intermediate, azoxybenzene **2**, that was subsequently reduced to azobenzene **3**. Reactions of this kind are defined as a consecutive reaction. Typically, the variation of the concentrations of **1**, **2**, and **3** are shown in **Figure 3.11**.

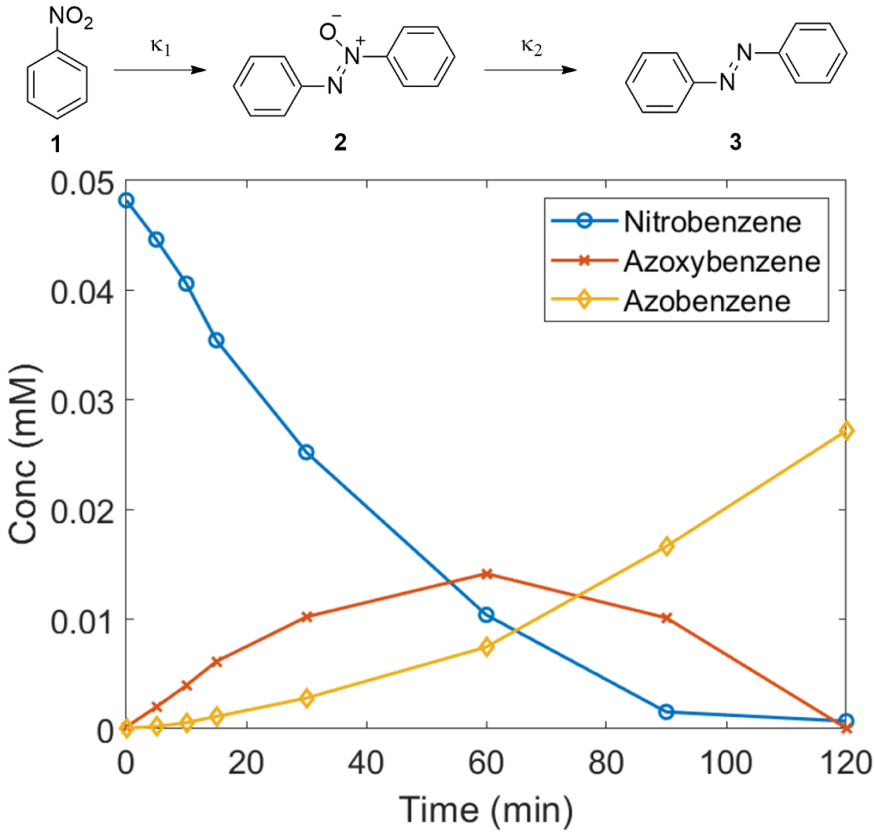

Figure 3.11 Typical evolution of the reaction mixture concentrations of nitrobenzene **1**, azoxybenzene **2**, and azobenzene **3** as a function of time. Reaction conditions: 0.1 mmol **1**, 0.1 mmol KOH, 2 mL IPA, 600 rpm, T=25 °C.

The concentration of all the components of the reaction can be analytically defined as a function of time by the kinetic equations of consecutive reactions[85] (Eq. 3.6-3.8).

$$[1]_t = [1]_0 \, e^{-k_1 t} \qquad \text{Eq. (3.6)}$$

$$[2]_t = \frac{[1]_0\, k_1}{k_2 - k_1}\ (e^{-k_1 t} - e^{-k_2 t}) \qquad \text{Eq. (3.7)}$$

$$[3]_t = [1]_0 \left\{1 + \frac{1}{k_1 - k_2}[k_2 e^{-k_1 t} - k_1 e^{-k_2 t}]\right\} \qquad \text{Eq. (3.8)}$$

Where, k_1 and k_2 are the kinetic constants of the first and second step of the reaction respectively.

The above kinetic equations were used to fit, in Matlab environment, the concentrations as a function of time, hence determining the kinetic constants of each step of the reaction. The results of the experiments are reported in **Table 3.7**.

Table 3.7 Kinetic analysis experiments.

	EXP	T [°C]	k_1 $[min^{-1}]$	k_2 $[min^{-1}]$	Y_3 [mol %]
Dark*	24	0	0.0006	0.0007	0.5
	25	12	0.0038	0.0028	9
	26	25	0.0074	0.0043	27.2
	27	36	0.0444	0.0466	92.7[a]
	28	48	0.1840	0.0946	95.8[b]
532nm 130mW*	29	0	0.0008	0.0026	1.5
	30	12	0.0025	0.0035	4.5
	31	18	0.0049	0.0050	19.4
	32	25	0.0138	0.0097	96.2
	33	36	0.0416	0.0387	95.2[c]

Reaction conditions: 0.3 mmol of **1, 0.3 mmol KOH, 50 mg 4-AuNP/TiO_2, 2 mL isopropanol, 0.05 mmol naphthalene, N_2 flow. Yield determined with GC and internal standard after 2 hours unless otherwise indicated.*

[a] Measured after 60 minutes.

[b] Measured after 15 minutes.

[c] Measured after 45 minutes.

The production of azobenzene **3**, as well as the values of the kinetic constants of reaction, increased proportionally with temperature. Moreover, the effect of the laser irradiation increased sensibly the speed and the yield of the reaction. Entry 29 displayed a 3-fold increase in the yield compared with entry 24. Likewise, in entry 32 the yield was increased 3.5 times with respect to entry 26. Finally, entry 33 provided the same yield of azobenzene **3** as entry 27 but in a shorter time.

The increase of the kinetic constants as a function of temperature and laser irradiation is represented in **Figure 3.12**.

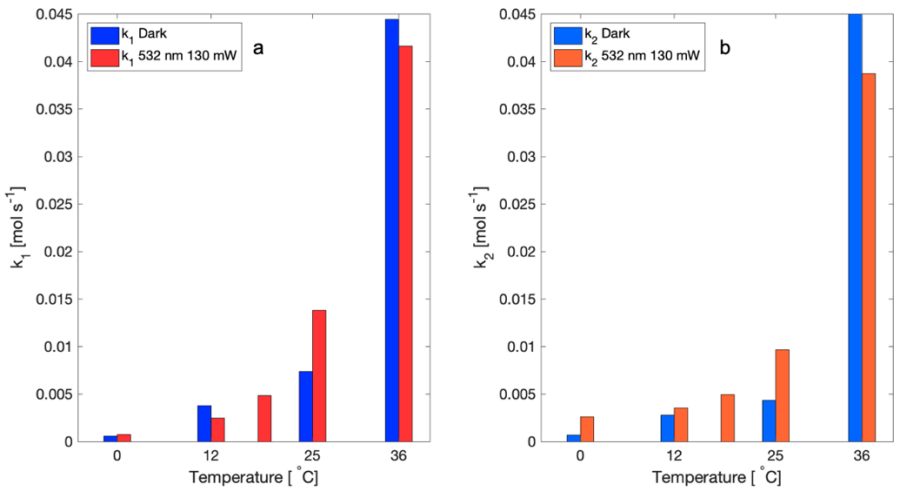

Figure 3.12 Bar plots of the kinetic constants of the reactions of **Table 3.7** as a function of temperature and irradiation conditions. **a**. First step kinetic constants for dark and irradiated reactions. **b**. Second step kinetic constants for dark and irradiated reactions.

The conversion of nitrobenzene **1** to azoxybenzene **2** was not significantly affected by the laser irradiation; the values of the kinetic constants for the irradiated reaction were roughly the same or even lower than the values of the dark reaction (**Figure 3.12 a**). On the other hand, the second step of the reaction was strongly influenced by the irradiation. For example, at 0 °C there was a 3.7-fold increase in the kinetic constant of the irradiated reaction with respect to the one for the dark reaction. All reactions ran under light illumination were characterized by higher values of the kinetic constants compared with the dark experiments at the same temperature, except for the experiment ran at 36 °C (**Figure 3.12 b**).

By applying the transition state theory for each step of the reaction[120], the variation of the kinetic constant of the reaction can be described as a function of temperature, as postulated in the Eyring equation[121] (Eq. 3.9).

$$k_n = \frac{k_B T}{h} e\left(-\frac{\Delta H_n^{\circ\ddagger}}{RT}\right) e\left(\frac{\Delta S_n^{\circ\ddagger}}{R}\right) \qquad \text{Eq. (3.9)}$$

Where k_n is the kinetic constant of an elementary step of the reaction, T is the absolute temperature, h and k_B are the Plank and the Boltzmann constants, respectively, R is the universal constant of gases, $\Delta H_n^{\circ\ddagger}$ and $\Delta S_n^{\circ\ddagger}$ are the enthalpy and entropy of activation for the nth step of reaction.

Plotting the Eyring equation in the linear form given by Eq. (3.10), allowed to obtain the well-known Eyring plots and determine the enthalpy and entropy of activation of the reaction for each step.

$$ln\left(\frac{k_n}{T}\right) = ln\left(\frac{k_B}{h}\right) - \frac{\Delta H_n^{\circ\ddagger}}{RT} + \frac{\Delta S_n^{\circ\ddagger}}{R} \qquad \text{Eq. (3.10)}$$

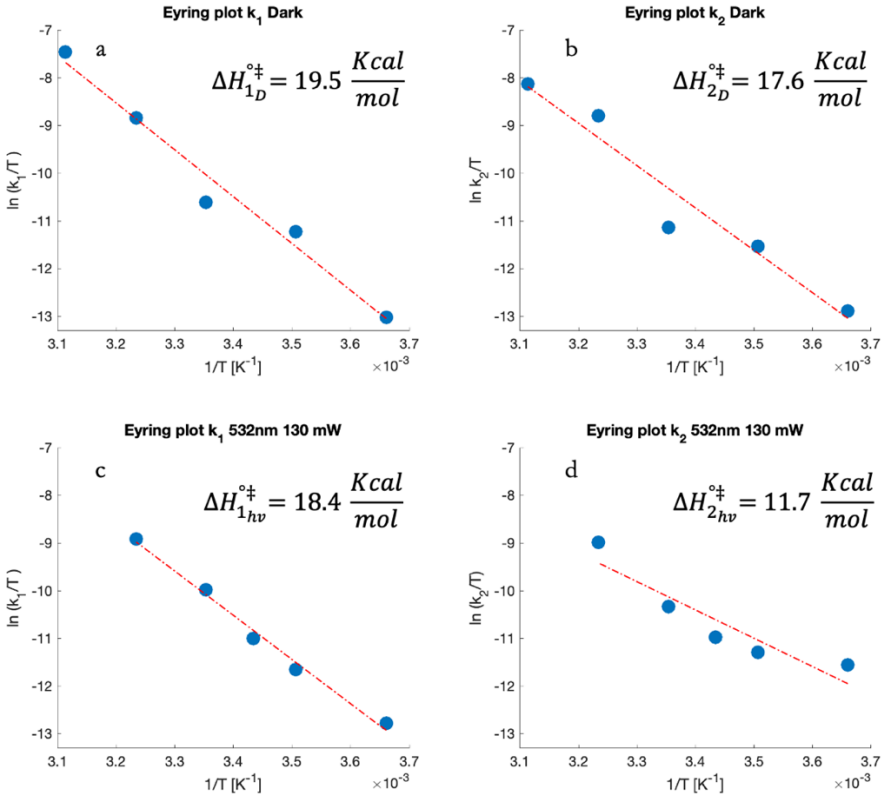

Figure 3.13 Eyring plots for the two steps of reaction and enthalpy of activation. **a.** First kinetic constant for the dark reaction. **b**. Second kinetic constant for the dark reaction. **c**. First kinetic constant for the reactions irradiated with 532 nm laser at 130 mW **d**. Second kinetic constant for the reactions irradiated with 532 nm laser at 130 mW.

The enthalpy of activation of the first step of the reaction diminished of only $1.1\ Kcal\ mol^{-1}$ applying the laser irradiation (**Figure 3.13 a** and **c**). Interestingly, the second step of the reaction resulted to be much more influenced by the light irradiation, since there was an enthalpy difference of $5.9\ Kcal\ mol^{-1}$.

Moreover, the entropies of activation were extrapolated from the linear fits giving values close to zero for both steps of the reaction and regardless of the illumination conditions.

3.6 Conclusions

The results reported in this section evidenced the catalyst AuNP/SiO_2 under laser-illuminated could convert up to 32.8 % of nitrobenzene to the intermediate azoxybenzene providing the first evidence of the role of laser light on the reaction. Besides, SiO_2 is a dielectric material where AuNPs are electrically insulated, thus confirming that the oxidation of IPA and the reduction of the nitrobenzene are steps that occur on the surface of the AuNPs[28].

The poor stability of SiO_2 as support stimulated us to screen different supports for the synthesis of the catalyst. The best choice for improving the performance of the material for the reduction reaction was TiO_2 P25 from EVONIK. Alternative supports to TiO_2, such as iron and cerium oxides, were investigated as well but did not show higher reactivities than TiO_2. Moreover, when considering the quantum yield, only TiO_2-based catalysts showed a substantial difference between dark and irradiated conditions.

The best performing catalyst was catalyst 4-Au/TiO_2. The material characterized by the smallest particle size amongst all the synthesized catalysts in this work allowed to run the reaction at significantly lower temperatures and a lower ratio of catalyst over reagent than reported in

the literature[50,78,122]. Moreover, it was possible to reach full conversion to azobenzene within 2 hours of irradiation at 130 mW with 532 nm laser.

The band gap value of 3.2 eV obtained from diffuse reflectance measurements of catalyst 4-Au/TiO_2 did not show any shift from the value of the TiO_2 P25 support. This means that the superior performance of the catalyst obtained with TiO_2 depended mainly on the possibility to access a smaller size of AuNPs[63,123].

The activation enthalpy and entropy for the two steps of the reaction were determined by combining the kinetic laws of consecutive reactions and the Eyring equation. The data analysis showed that the green laser irradiation of the AuNP/TiO_2 catalyst affected the two steps of the reaction differently. In the second step of the reaction, the enthalpy of activation dropped $5.9\ Kcal\ mol^{-1}$ when irradiated at 130 mW with a 532 nm laser light compared with the reaction ran in the dark. In our experiment, the difference of enthalpy of activation registered for the second step of the nitrobenzene reduction coupling reaction was $3.9\ Kcal\ mol^{-1}$ higher than the reported activation energy difference for the overall reaction[50].

The entropic factor of the reaction was close to zero, regardless of the illumination and for both steps of the reaction, indicating that the reaction occurred on the surface of the catalyst[124].

This study allowed to quantify the contribution of the laser irradiation of the investigated system but could not assess the mechanism through which the plasmonic NP activate the reagents. In the next chapter, we describe a detailed experimental procedure and data analysis performed

to build a model able to determine the contribution of the plasmon-generated energetic electrons to the reaction product.

The synthesis of AuNR/TiO_2 and AuNP-NR/TiO_2 catalysts allowed to assess some preliminary aspects of the way gold NPs catalyses the reaction. The reaction was greatly slowed down (5% yield in 24 hours) in the presence of AuNR/TiO_2 alone, although the thermal effect of this material was evident. The decreased reactivity was related to the much smaller active surface for this material compared with the AuNP/TiO_2 catalysts.

AuNR structures were mainly absorbing the 785 nm laser and emitting heat to the surrounding and, when added as additives to the catalyst 4-AuNP/TiO_2, demonstrated to be able to generate a positive contribution to the outcome of the reaction.

These initial results encouraged us to investigate more in-depth the effect that temperature had on the reaction and to run more experiments to understand to which extent the interaction of each one of the lasers used in this work would influence the Au-based catalysts.

4. Modelling the yield of azobenzene and azoxybenzene

This section analyses the results of experiments designed to evaluate the nitrobenzene reductive coupling and proposes models to rationalize the effect that visible light had on the reaction outcome. The reactions were run screening the intensities of two laser sources (emitting monochromatic light at 532 nm and 785 nm, respectively) and varying the kind of Au-based catalyst.

The methodology followed in this section can be summarized in the step by step procedure described below:

1. Determine the family of distribution to which the response variables (in our case, the yield of azobenzene and azoxybenzene) belong.
2. Define the link function of the model and the linear predictors.
3. Build the model adding one factor at a time, starting from intercept and random factors.
4. Run an analysis of variance (ANOVA) test to select the model that best estimates the variables.
5. Run inference tools, such as contrast matrix and model predictions.

The first step is crucial to define which model would better describe the dependent variable. For example, a normally distributed response variable falls into the linear model (LM) and linear mixed effects (LME) models. All the other distributions are better described by the generalized linear model (GLM) and generalized linear mixed effects (GLME)

models. As explained in Section 3.5.2, the choice of the link function is conditioned by the dependent variable's family of distribution.

The data were processed in R-Studio environment to test the following null hypotheses:

Hp. 1.

a. The intensity of the 532 nm laser has no effect on the yield of azobenzene.
b. There is no statistically significant difference on the yield of azobenzene between the two catalyst types (only AuNPs or a mixture of AuNPs and AuNRs) when varying the intensity of the 532 nm laser.

Hp. 2.

a. The 785 nm laser has no effect on the yield of azobenzene.
b. There is no statistically significant difference on the yield of azobenzene between the two catalyst types (only AuNPs or a mixture of AuNPs and AuNRs) when varying the intensity of the 785 nm laser.

Hp. 3.

a. The intensity of the 532 nm laser has no effect on the yield of azoxybenzene.
b. There is no statistically significant difference on the yield of azoxybenzene between the two catalyst types (only AuNPs or a mixture of AuNPs and AuNRs) when varying the intensity of the 532 nm laser.

Hp. 4.

a. The 785 nm laser has no effect on the yield of azoxybenzene.

b. There is no statistically significant difference on the yield of azoxybenzene between the two catalyst types (only AuNPs or a mixture of AuNPs and AuNRs) when varying the intensity of the 785 nm laser.

4.1 Analysis of the dependent variables

The yields of azobenzene and azoxybenzene were measured in 49 experiments (including repeated experiments) performed with variable intensities for the two lasers emitting at 532 and 785 nm, respectively. As reported in Table 3.3 of Section 3.5.1, two sets of experiments were run. The two groups differed by the use of 50 mg 4-AuNP/TiO_2 catalyst in one case and the use of 50 mg 4-AuNP/TiO_2 and 10 mg AuNR/TiO_2 in the other. The dataset was enlarged with the addition of data from dark experiments and from experiments where the irradiation was limited to only one of the two lasers at a 130 mW intensity. These conditions were applied to both catalytic systems. Considering the kinetic data of each experiment, the total number of observations was 322.

The dependent variables under investigation were characterized by continuous positive numbers. This suggested that, in the case of the non-normal distribution of the variable, the probability density distribution of the random effects could be approximated by a gamma distribution[90]. To check for this possibility, the probability density function of the yield of azobenzene and yield of azoxybenzene were analysed. The results are represented in **Figure 4.1**.

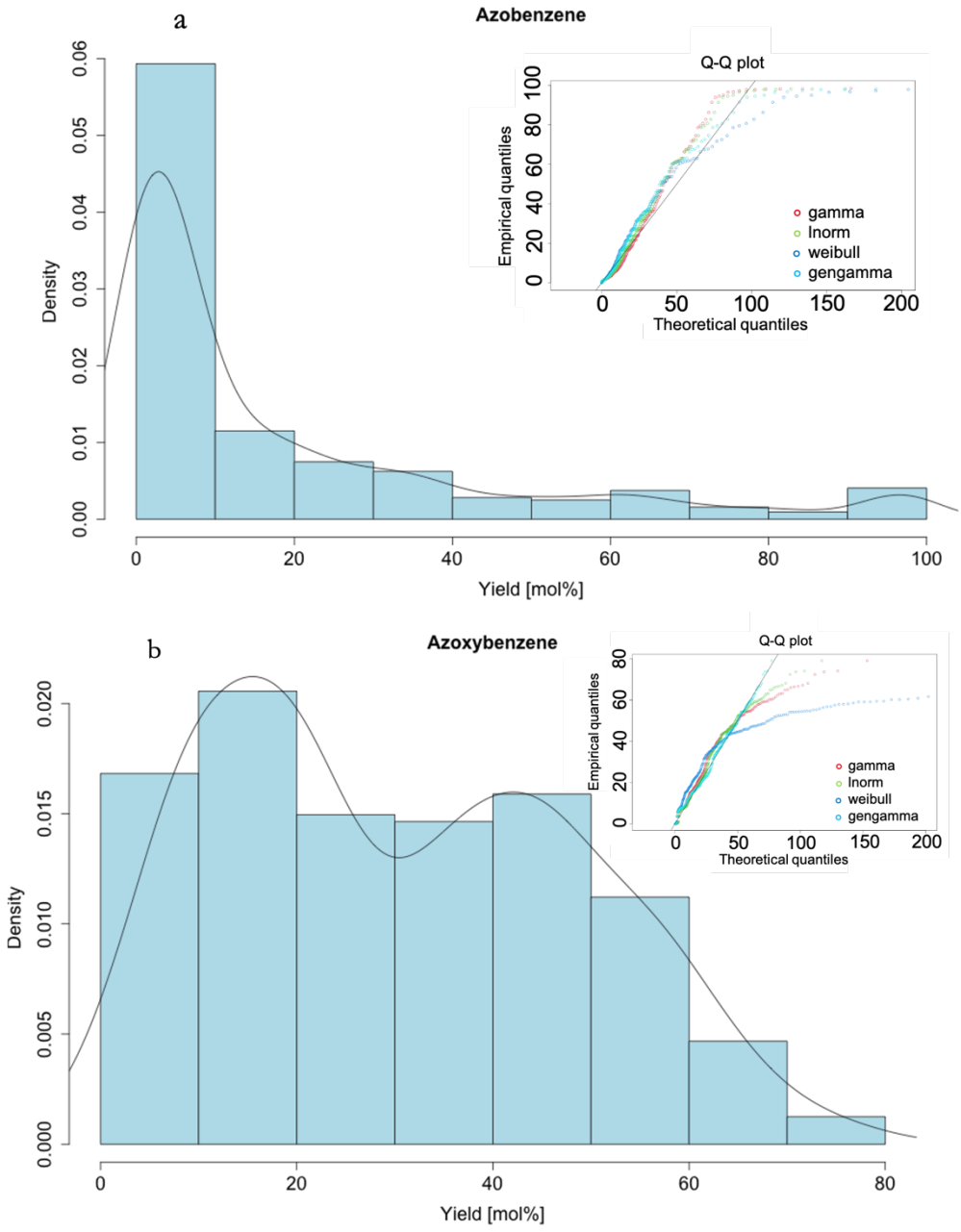

Figure 4.1 Probability density distribution plots of the dependent variables. The inset shows the Q-Q plot of the real data distribution as a function of commonly known distributions. **a**. yield of azobenzene distribution. **b**. yield of azoxybenzene distribution.

The histograms of **Figure 4.1** describe the distribution of the dependent variables from all the experimental observations (azobenzene and azoxybenzene). In both cases, the data are left limited, skewed, and non-normally distributed. The density distribution of the dependent variable determines which kind of linear model is more appropriate to fit the data. The quantile–quantile plots in the insets indicate that the gamma distribution family is the most appropriate to model both variables.

4.2 Linear predictors and link function

The most commonly used link function for gamma distributed random effects is the logarithm function reported in equation (4.1).

$$\boldsymbol{\eta} = \log(\boldsymbol{\mu}) \qquad \text{Eq. (4.1)}$$

Where, μ is the mean value of the estimated dependent variable and η is the linear predictor of the variable.

The linear predictors were expressed according to the hypotheses highlighted in section 4 as a linear combination of unknown parameters. For example, assuming that all the hypotheses of Section 4 were true, then the linear predictor equation of the model would be equal to equation (4.2).

$$\boldsymbol{\eta} = \boldsymbol{X}\begin{bmatrix} \beta_0 \\ \beta_t \\ \beta_G \\ \beta_{IR} \\ \beta_{G*t} \\ \beta_{IR*t} \\ \beta_{CAT} \\ \beta_{Cat*G} \\ \beta_{Cat*IR} \end{bmatrix} + \boldsymbol{Z}\begin{bmatrix} b_{EXP} \\ b_{CAT} \end{bmatrix} \qquad \text{Eq. (4.2)}$$

Where $\boldsymbol{X}$ is a matrix 322×9 of the experiments multiplying the 9×1 column vector $\boldsymbol{\beta}$ containing all the estimators needed to satisfy the initial hypotheses. Every element of the vector estimates an effect of the independent variables: β_0 gives the intercept, β_t the effect of time, β_G and β_{IR} the green and infrared laser intensities, respectively, β_{G*t} and β_{IR*t}, are the interaction terms for the laser intensity of each laser with time, and β_{CAT}, β_{Cat*G}, β_{Cat*IR} are the effects of the catalyst type and the interaction terms between the catalyst and the green and IR lasers, respectively. Finally, $\boldsymbol{Z}$ is a 322×2 matrix for the estimation of the random intercepts b_{EXP} and b_{CAT} within experiments and between catalyst types, respectively.

4.3 Model optimization

Each model was fitted with a maximum likelihood estimation based on adaptive Gauss-Hermite quadrature over 6 points[125]. Following a

bottom-up strategy, starting with a model constituted by the intercept and random effects, the models were built by increasing the number of factors. Each model was then evaluated by observing the P-values for a z-test for each factor at a level of significance of 0.05 ($\alpha = 0.05$). A P-value < 0.05 meant that the null hypothesis–i.e. the factor was not influencing the estimation of the dependent variable–was false. The model selection was performed through additional ANOVA statistical tests.

4.3.1 Models for azobenzene

Fitting of the data started by adding the standardized variable time, obtained by applying equation (3.9) of Section 3.5.1, to the intercept and the random effects of the catalyst type and experiment number, as described by model equation (4.3).

$$\eta_{AZO} \sim 1 + Time + (1|CAT) + (1|EXP) \qquad \text{Eq. (4.3)}$$

Where, η_{AZO} is the linear predictor for the azobenzene yield%.

The $Time$ variable gave a very low P-value, indicating that the variable was necessary to define the model. Regarding the random variables, only the experiment grouping, defined in the equation by the $(1|EXP)$ term, resulted in a non-zero variance of the estimated random effect. Therefore,

the random variable for the catalyst type was omitted from the following model equations.

Models in which the laser intensities were set as categorical variables (on four levels each: No IR, IR 1, IR 2, IR 3, and No Green, Green 1, Green 2, Green 3) fitted better the dependent variables than models in which the laser intensities were set as numerical variables; the former provided better predictions for the dependent variables. The levels for the dark reactions constituted the reference level for the estimation of the intercept of the model.

The effect of the 532 nm laser was investigated, resulting in the model equation (4.4). This model corresponded to testing Hp. 1 **a**.

$$\eta_{AZO} \sim 1 + Time + Green + (1|EXP) \qquad \text{Eq. (4.4)}$$

Where, $Green$ is the categorical variable with 4 levels for the 532 nm laser intensity.

The P-values for the new variable confirmed that the green laser was playing a role in determining the yield of the reaction, as shown in **Table 4.1**.

Table 4.1 Summary for the model (4.4).

Estimator	Estimate	Std. Error	z value	$P\ (>\|z\|)$
(Intercept)	2.2329	0.1644	13.586	<2E-16
Time	1.9567	0.0928	21.094	<2E-16
Green 1	0.2918	0.2161	1.350	0.177
Green 2	0.5247	0.1870	2.806	0.0050
Green 3	0.4902	0.1830	2.678	0.0074

The output generated by the regression software reported in **Table 4.1** contained the estimates of the coefficients of the model equation (4.4), the standard error in estimating the coefficients, and the z value, i.e. the estimate of the coefficient divided by its standard error. The software returned the probability for a z-test at a level of significance of 0.05.

The effect of the green laser was statistically significant only when the reactions were run at the highest levels, i.e. 2 and 3. When level Green 1 was used, there was no difference in the yield of azobenzene from the reactions ran in dark conditions or irradiated only with the 785 nm laser. The ANOVA tests further confirmed that the introduction of the new factor produced a model characterized by a higher accuracy in describing the dependent variable than model (4.3). A very low P-value and Akaike information criterion (AIC) numbers were registered for models (4.3) ($P < 2e-16$ and $AIC_{6.3} = 1761$) and (4.4) ($P < 2e-16$ and $AIC_{6.3} = 154$).

To test Hp. 2 **a**, a factor for the IR laser intensity levels was added to the model as well, as shown in equation (4.5).

$$\eta_{AZO} \sim 1 + Time + Green + IR + (1|EXP) \qquad \text{Eq. (4.5)}$$

Where the factor IR was set as a categorical variable constituted by 4 levels (0, 28, 154, 280 mW).

The model summary evidenced that only the intermediate level was suspected of being significant (IR level 2, corresponding to 150 mW, P-value = 0.0981). Moreover, the introduction of the new factor decreased the significance of all of the levels of the other lasers. As a consequence, the ANOVA between models (4.4) and (4.5) resulted in a worsening of the explanatory power of the model. The AIC number of the new model was higher than the one of the previous model, and the P-value for the model was equal to 0.161. These two values confirmed the null hypothesis (the two models were equally explaining the dependent variable). Therefore, model (4.4) was more appropriate to describe the variation in the azobenzene yield.

To check Hp. 1 **b** and 2 **b**, interaction terms were added to the model affording model equations (4.6) and (4.7), respectively.

$$\eta_{AZO} \sim 1 + Time + Green + Green * CAT + (1|EXP) \qquad \text{Eq. (4.6)}$$

$$\eta_{AZO} \sim 1 + Time + Green + IR * CAT + (1|EXP) \qquad \text{Eq. (4.7)}$$

In both cases, the addition of interaction terms did not produce better models. The irradiation of different types of catalyst did not influence significantly the reaction outcome, as was confirmed by higher AIC

numbers than the ones provided by model (4.4), particularly in the case of model (4.7), and very high P-values for the interaction terms.

Finally, the addition of a quadratic term for the time factor produced model equation (4.8).

$$\eta_{AZO} \sim 1 + Time + Time^2 + Green + (1|EXP) \quad \text{Eq. (4.8)}$$

The model reported above was chosen as the best model capable of describing the dependent variable. The statistics of the fixed effects are reported in **Table 4.2**.

Table 4.2 Summary for the model defined in model (4.8) and ANOVA of models (4.8) and (4.4)

Estimator	Estimate	Std. Error	z value	P (> |z|)
(Intercept)	2.7743	0.1859	14.926	<2E-16
Time	1.9561	0.0792	24.204	<2E-16
Time²	-1.0587	0.1596	-6.633	3.3E-11
Green 1	0.2921	0.2112	1.383	0.1667
Green 2	0.5551	0.1864	2.979	0.0029
Green 3	0.4915	0.1815	2.708	0.0069
ANOVA	**AIC**	**P (> |z|)**		
Eq. (4.4)	153.55			
Eq. (4.8)	110.33	1.76E-11		

AIC: Akaike number. ANOVA: analysis of variance.

The results in **Table 4.2** showed that the addition of the squared factor for the time of reaction provided a model for which the significance of the new factor was very high. The significance of the other factors did not change greatly from the values reported in **Table 4.1** for model (4.4). Indeed, the ANOVA between models (4.8) and (4.4) gave a great difference of AIC numbers and, therefore, a very small P-value for the extended model (4.8).

Finally, the candidate model (4.8) was again tested for the hypothesis of Section 4, modifying its equation by adding terms for the kind of catalyst, the IR laser intensity, and the interactions between catalyst type and lasers. Each one of the new factors was added one at a time. The models were evaluated considering P-values and ANOVA testing as described above. The obtained models did not show any improvement in the quality of the model, i.e. higher AIC numbers and P-values>0.05 for the new term. Hence, model (4.8) was selected as the best model for representing the yield of azobenzene.

4.3.2 Models for azoxybenzene

The same strategy described in Section 4.3.1 was applied for the selection of the model for the yield of azoxybenzene. The fitting of the model started from the same reasonable assumption made before, that is, the dependent variable has a strong dependence on time and its random effects are distributed only within the experiment run. The initial model was then described by equation (4.9).

$$\eta_{AZX} \sim 1 + Time + (1|EXP) \quad \text{Eq. (4.9)}$$

Where, η_{AZX} is the linear predictor for the azoxybenzene yield%.

This model was then compared with two more complex models containing the 532 nm [model (4.10)] and the 785 nm laser intensity levels [model (4.11)].

$$\eta_{AZX} \sim 1 + Time + Green + (1|EXP) \quad \text{Eq. (4.10)}$$

$$\eta_{AZX} \sim 1 + Time + IR + (1|EXP) \quad \text{Eq. (4.11)}$$

In both cases, the new estimators for both lasers showed very high P-values. The ANOVA between models (4.10) and (4.9) and models (4.11) and (4.9) evidenced that both lasers did not influence significantly the conversion of nitrobenzene to azoxybenzene.

As for azobenzene, the interaction effects of the catalyst type with the laser light were also investigated for the two lasers with models (4.12) and (4.13).

$$\eta_{AZX} \sim 1 + Time + Green * CAT + (1|EXP) \quad \text{Eq. (4.12)}$$

$$\eta_{AZX} \sim 1 + Time + IR * CAT + (1|EXP) \quad \text{Eq. (4.13)}$$

The resulting high P-values and AIC numbers clearly showed that the introduction of the interaction terms was not statistically significant.

Finally, the addition of a quadratic term for the $Time$ variable afforded model (4.14).

$$\eta_{AZX} \sim 1 + Time + Time^2 + (1|EXP) \qquad \text{Eq. (4.14)}$$

Results of the P-values for the model above and the ANOVA test are reported in **Table 4.3**.

Table 4.3 Summary for the model defined in equation (4.14) and ANOVA of models (4.14) and (4.9).

Estimator	Estimate	Std. Error	z value	P (> |z|)
(Intercept)	4.1324	0.1120	36.885	< 2E-16
Time	0.4664	0.0792	5.892	3.81E-09
Time^2	-1.2158	0.1577	-7.711	1.25E-14
ANOVA	**AIC**	**P** (> |z|)		
Eq. (4.9)	201.40			
Eq. (4.14)	142.71	6.684E-15		

AIC: Akaike number.

The introduction of squared terms greatly enhanced the quality of the model for the azoxybenzene yield when compared with the reduced model of Eq. (4.9). The equation that best described the dependent variable was Eq. (4.14). Surprisingly, there were no statistically significant

effects for both lasers nor their interaction terms with the catalyst type.

4.4 Conclusions

Equations (4.8) and (4.14) were the most accurate estimators for the yield of azobenzene and azoxybenzene, respectively. Predictions of the dependent variable were calculated by transforming the model estimator equations to their respective inverse link function. **Figure 4.2** shows the fitted data along with the model predictions for the azobenzene yield.

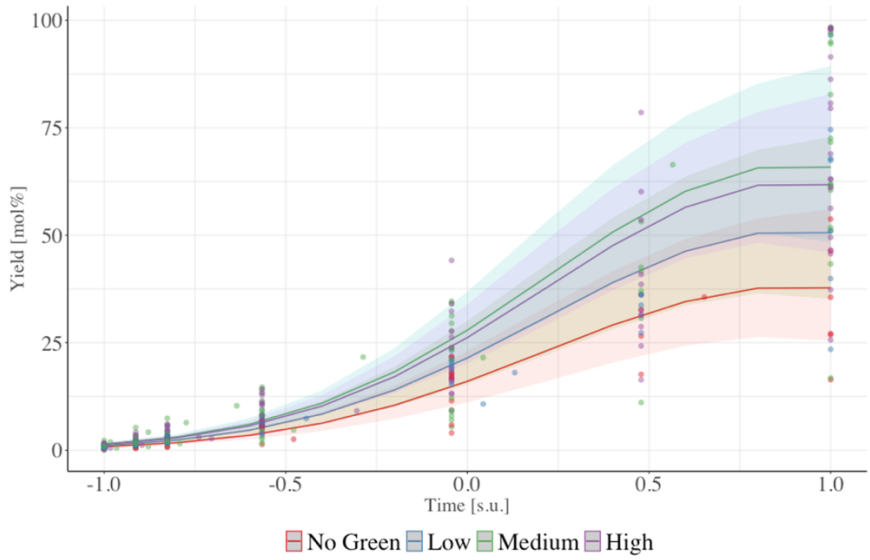

Figure 4.2 Azobenzene model plot as a function of time (s.u.=standardized units between 5 and 120 min) and laser level intensity (No Green=0 mW, Low=16 mW, Medium=73 mW, High=130 mW). Dots represent the experimental data coloured according to the 532 nm laser intensity. Shaded areas correspond to the 95% confidence intervals of the predicted yield.

The model for the yield of azobenzene showed a substantial difference in the reaction outcome only as a function of the green laser intensity. Increasing the 532 nm laser intensity from 0 to medium (73 mW) and high levels (130 mW) had the same effect on the reaction outcome, evidencing that a saturation effect was reached at higher intensities than 73 mW. A contrast matrix for the green laser variable was used to check for differences between the levels of the variable; its results are reported in **Table 4.4**.

Table 4.4 Contrast matrix for the 4 levels of green laser intensity applied to model equation (4.8).

Entry	Hypothesis	Estimate	Std. Error	z value	P (> |z|)
1	**Gr 1 = No Gr**	0.2921	0.2112	1.383	0.5038
2	**Gr 2 = No Gr**	0.5551	0.1864	2.979	0.0146
3	**Gr 3 = No Gr**	0.4915	0.1815	2.708	0.0333
4	**Gr 2 = Gr 1**	0.2630	0.1713	1.536	0.4097
5	**Gr 3 = Gr 1**	0.1994	0.1660	1.201	0.6202
6	**Gr 3 = Gr 2**	0.0637	0.1330	0.479	0.9629

AIC: Akaike number. Gr: Green.

The contrast matrix was intended to check the null hypothesis stating that each couple of levels of the 532 nm laser exert the same effect on the yield of the reaction. As shown by the P-values reported in **Table 4.4**, the hypothesis was rejected only for entry 2 and 3. In other words, the contrast matrix confirmed that there was a substantial difference between the results of the reactions run at level 2 or 3 compared to the results collected from reactions run at level 0 of the green laser light. Moreover,

there was no difference between levels 2 and 3, suggesting that the maximum efficiency of the catalyst was reached when approaching to intensity values close to level 2.

Interestingly, the effect of the IR laser levels could not be included in the models, returning no statistically significant P-values. No effect was evidenced by the 785 nm laser neither for reactions run with only the 4-AuNP/TiO_2 nor for ones containing an addition of AuNR/TiO_2 catalyst. This result confirmed that only the 532 nm laser was able to trigger the studied reaction. The thermal effects of AuNRs due to the absorption of the 785 nm laser light could not produce any statistically significant effect. If any, the thermal effects of the AuNRs were negligible with respect to the effect of the 532 nm laser on the 4-AuNP/TiO_2 catalyst.

From the analysis of the collected data, we could infer that the mechanism through which the plasmonic nanoparticles were activating the reagents was due to electronic effects. The resonant absorption of the 532 nm laser light (medium and high levels) generated enough energetic carriers, electrons and holes, that were transferred to the adsorbed molecules of IPA and nitrobenzene, respectively, which, in turn, activated the production of azobenzene.

Only the laser emitting light at 532 nm was able to trigger the reaction. Despite the 785 nm laser intensity was varied over a broader range (16 to 130 mW for the green laser and 28 to 280 mW for the IR), the effect of the IR laser could not be observed in the analysed data set. This led us to conclude that the thermal effects generated by the excitation of the AuNRs plasmon irradiated with the 785 nm laser were not influencing the reaction outcome significantly.

Figure 4.3 shows the plotted data set and the fitted model (4.14) curves for azoxybenzene yield.

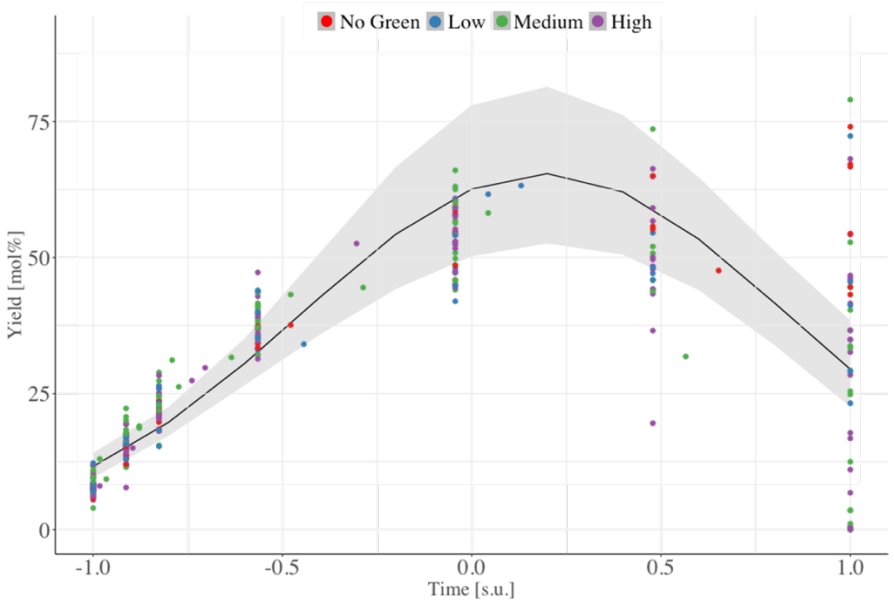

Figure 4.3 Azoxybenzene model plot as a function of time (s.u.=standardized units between 5 and 120 min). Dots represent the experimental data coloured according to the 532 nm laser intensity. Shaded areas correspond to the 95% confidence intervals of the predicted yield. No Green=0 mW, Low=16 mW, Medium=73 mW, High=130 mW.

The selected model did not contain any factor accounting for the laser intensity. The variation of the azoxybenzene was dependent only on the time of reaction. The yield for experiments in the absence of green laser irradiation (red dots in **Figure 4.3**) showed a range at 120 minutes of reaction (value equal to 1 in the abscissa) oscillating between 45% and 75%, while for all the other experiments yields were distributed mainly from around 50% to 0%. The evaluation of an alternative model containing an interaction term of green laser with time, defined by β_{G*t}, generated an alternative model. In this model, differences were evident

only between the 0 level green experimental points; the rest of the experiments were characterized by very similar estimated coefficients. This model was rejected because it did not pass the ANOVA test.

Three experiments were run varying the intensity of the two lasers to assess the predictive value and robustness of the models. The results for the azobenzene yield are reported in **Figure 4.4**.

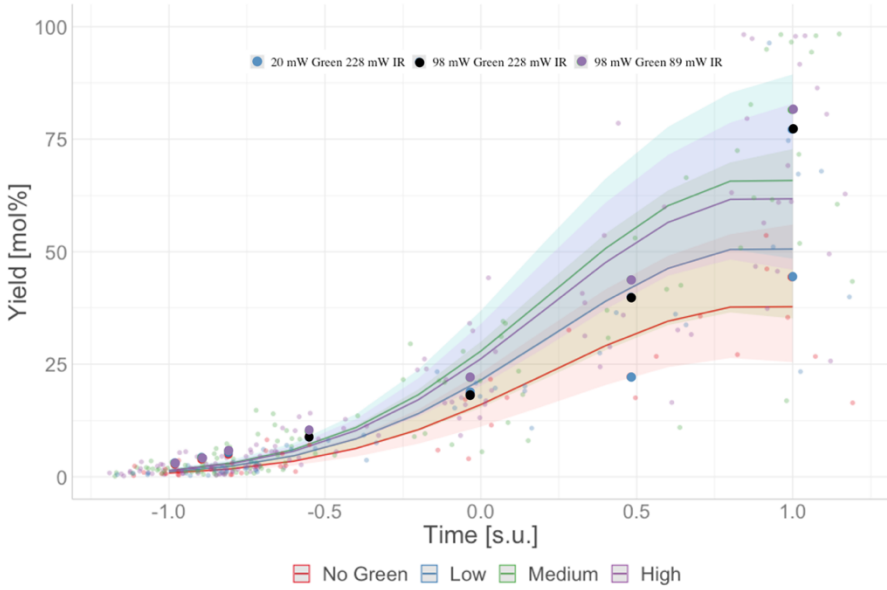

Figure 4.4 Plot of predictions for the yield of azobenzene as a function of time (s.u.=standardized units between 5 and 120 min) and 532 nm laser intensity. Shaded areas correspond to the 95% confidence intervals.

The experiment, ran at intensities of 20 mW (green laser) and 228 mW (IR laser), showed a final yield within the 95% confidence interval (95% CI) of the model predictions for no green and low intensity (blue dots). The other two experiments, ran at 98 mW (green laser) and 89-228 mW

(IR laser), gave similar results, both lying within the 95% CI defined by the medium and high intensities.

Results for the model validation experiments concerning the azoxybenzene yield are reported in **Figure 4.5**.

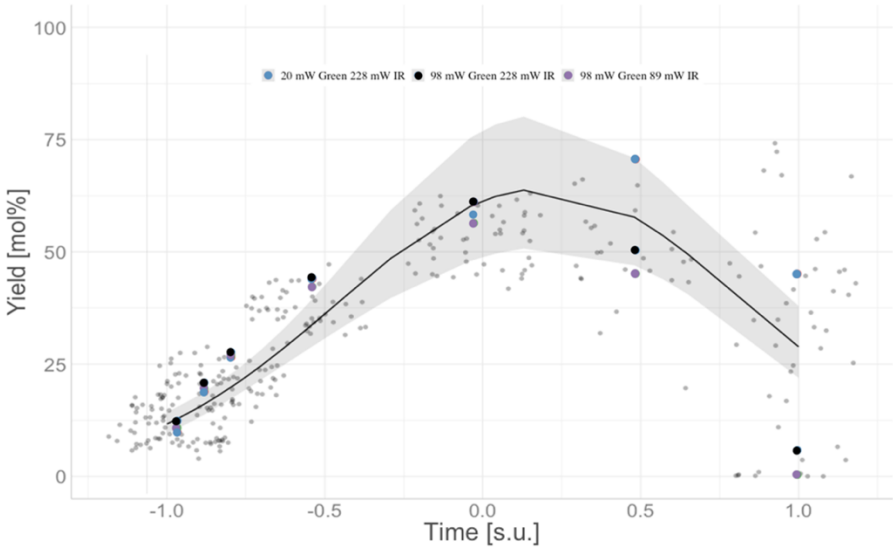

Figure 4.5 Plot of predictions for the yield of azoxybenzene as a function of time (s.u.=standardized units between 5 and 120 min) and 532 nm laser intensity. Shaded areas correspond to 95% confidence intervals.

Nearly all experimental points fell within the 95% CI of the model predictions, except for the highest time values (120 minutes) for which the variability of the data was higher.

The experiments confirmed that the laser irradiation affected only the second step of the reaction while the first step was not affected by the irradiation of the laser.

In conclusion, the modelling of the collected experimental data allowed to build two models describing the dependence of the yield of

azobenzene and azoxybenzene as a function of time and laser intensities. The design of the experimental conditions allowed to achieve some important considerations on the mechanism of the reaction. The lack of statistical difference between the 4-AuNP/TiO_2 catalyst and the mixture of 4-AuNP/TiO_2 with AuNR/TiO_2, as well as the absence of any effect of the IR laser, gave a strong indication that the mechanism of activation of the reaction involved the transfer of electrons generated from the hemispherical metal NP (upon excitation of the plasmon by the 532 nm laser) to the absorbed molecules of the reactants.

5 Conclusions and future work

This thesis was motivated by the debate in the scientific community about the actual mechanism behind plasmonic catalysis. We centred our efforts on the discrimination between the collective thermal effects and electronic effects of plasmon catalysis. Thermal effects have been demonstrated to contribute to the enhancement of this catalysis. Nevertheless, it is fundamental to understand which one of those two effects predominates in the catalytic process. A heterogeneous photocatalytic reaction, occurring through a photoinduced charge transfer step, allows accessing novel reactivity and selectivity compared to conventional heating[126]. The use of visible and solar light sources represents economic and environmental advantages, encouraging the investigation in the field of heterogeneous photocatalysis for industrial applications[127]. However, this field is still at the research stage with very few commercial applications.

Herein, we have investigated the catalysis of plasmonic AuNPs supported on different substrates. AuNPs were chosen because of their high stability and the availability of protocols to afford different shapes and sizes of NPs. The possibility to synthesise particles characterized by dominant thermal effects, such as AuNRs, was a fundamental point of this work. The nitrobenzene reductive coupling reaction was selected as a model reaction to test the initial hypotheses. Previous works have evidenced that the reaction occurs only on the surface of AuNPs through direct photocatalysis[28] and that the reaction is partially enhanced by

conventional heating. Therefore, we considered the selected reaction a good candidate to test the mechanism of activation of plasmonic catalysts.

We initially demonstrated, by using plasmonic AuNPs under laser light irradiation, that the rate of the test reaction was inversely proportional to the size of the metal NPs. Catalyst 4-Au/TiO_2 was the best performing catalyst with a mean particle size of 3.1 ± 0.8 nm. The most effective method to synthesise the active and stable plasmonic catalyst was the modified Haruta method reported in Section 3.

The DR spectra of the catalyst 4-Au/TiO_2, as well as the fact that the Au/SiO_2 was active for the reaction under investigation, confirmed that the reaction occurred only on the surface of the AuNPs. If an interaction between the substrate and the AuNPs was necessary for the catalysis, we would have registered no reactivity for the silica-based catalyst. The absence of any shift in the band-gap energy of the support was proven through the extrapolation from the Kubelka-Munk function plot of **Figure 3.6**.

By applying the Eyring equation, we obtained the enthalpy of activation for each step of the reaction. The second step was strongly influenced by the irradiation wi

th the 532 nm laser source, whereas the first step was only weakly influenced by this laser irradiation. To the best of our knowledge, the difference of enthalpy of activation between the illuminated and dark reaction was the highest ever reported. Indeed, the difference of activation energy[128] reported by Ke *et al.*[50] for the global reaction was about $1.6\ Kcal\ mol^{-1}$. With our work we found that the difference of activation energy for the second step was $5.9\ Kcal\ mol^{-1}$, confirming

that the synthetized catalyst was highly active under monochromatic light irradiation.

The present work was intended to furnish a rational approach for the investigation of the reaction mechanisms of plasmon-enhanced reactions in liquid phase. The concept was that, provided that the temperature of reaction could be precisely controlled and measured[42,71], plasmonic effects, such as energetic electron generation and thermal effects, could be separated and quantified.

The use of a systematic approach for arranging the experiments based on statistics tools, described in section 2, allowed to minimize the number of experiments while maintaining high reliability of the estimated coefficients of the model.

The two models for the yield of azobenzene and azoxybenzene evidenced how the effect of the NIR laser on the AuNRs was negligible compared to the effect of the green laser on the AuNPs. Interestingly, the effect of laser irradiation was relevant only for the second step of the reaction, as expected considering the preliminary results reported in section 3.

5.2 Future work

Extending the knowledge of the influence of laser irradiance on the rate of the reaction is considered to be an issue of primary importance.

As was pointed out in section 4, the plateau reached by the yield of azobenzene (**Figure 4.2**) at medium and high intensities for the 532 nm

laser suggests that a second set of experiments could be designed screening the laser power at lower intensities. A reasonable range for the optimization of the laser intensity could go from 0 to 70 mW.

Moreover, this prospective study could delve into how the green and NIR laser intensities affect the activity of a catalyst containing both AuNPs and AuNRs supported on a surface of TiO_2. This study would aim to understand whether the proximity or even the contact of AuNRs with AuNPs could be beneficial for the catalytic process. We envision that electronic effects, such as electron transfer from AuNRs to smaller NPs[31,129], could be relevant for the catalysis of the reaction when the geometry of the catalyst is properly designed. If this hypothesis was confirmed, we would expect a significant influence of the 785 nm laser irradiation on the new catalyst.

The data collection can also be improved through the implementation of a transmission dip probe[130] in the reactor setup, which would measure the spectra of the crude reaction mixture in the NIR region. Constant monitoring of the spectra of the components of the reaction mixture would allow obtaining more kinetics data points and a better precision on the concentration measurements.

The exploration of the scope of the reaction, by using substituted nitrobenzene derivatives, could give further insight into the electronic nature of the catalytic cycle. Electronic effects of substituents on the reactant molecule can vary sensibly the energetic levels of the HOMO and LUMO of the molecule, thus influencing the electron transfer efficiency[131] from the plasmonic AuNPs.

The design of a flow chemistry device is another important possible development for a plasmonic photocatalysis system. Continuous flow chemistry is a promising new technology that has created room for investigation as well as applications in industry and it is particularly advantageous for heterogeneous catalysis[132,133]. A continuous flow reactor allows to improve heat and mass transfer, increases the activity of the catalyst, and the possibility to access preparative scale and enhanced safety because of the reduced dimensions of the reactive section of the system compared with batch processes[134]. Moreover, the use of an immobilized heterogeneous catalyst in a continuous flow reactor allows collecting the product of reaction without the need for the separation of solid material easing also the recyclability of the catalyst.

Concerning heterogeneous photocatalysis, this technology results beneficial for the exploitation of the illumination source. Indeed, the illuminated area can be increased dramatically if compared with a reaction run in batch conditions, where the light usually reaches the sample only from one surface of the reactor.

To the best of our knowledge, the application of flow chemistry in the field of plasmonics is limited to a few examples related only to the synthesis of colloidal solution of plasmonic NPs[135,136]. Yet, the development of a flow heterogeneous photochemistry device presents multidisciplinary issues to address. A tentative roadmap should necessitate the understanding of the minimum irradiance required to observe photocatalysis for the test reaction in batch conditions. Subsequently, a 532 nm led array would be built to provide the correct irradiance for the flow reactor.

In the case of a packed bed reactor the size of the tubings strongly influences the transmittance of light through the reaction mixture. Therefore, the screening of the tubings sizes would be studied carefully for optimizing the performances of the continuous flow reactor. Importantly, the design of the catalyst should take into account the particle size of the support material (e.g. TiO_2 P25 from EVONIK) that should be of micrometric size to avoid clogging of the system and the increase of the pressure inside the packed bed reactor. A valid alternative is constituted by VP AEROPERL® P 25/20, which primary particle size is 20 μm. The synthesis of the catalyst with the new support material would guarantee the same surface interaction between the TiO_2 and the AuNPs but would improve the flow behavior of the catalyst.

Alternatively, the reactor can be designed in a 2D fashion exploiting a glass reactor. The catalyst can be covalently grafted on the glass surface in two consecutive steps. First, the TiO_2 would be covalently bound to the internal surface of the reactor trough sol-gel technology[135]. Finally, the AuNPs can be synthesised in situ on the TiO_2 surface modifying the deposition-precipitation method reported in Section 3.2.

The development of a continuous flow plasmonic photoreactor would allow the superior exploitation of the catalyst activity and the optimal utilisation of the light source as opposed to batch processes. Importantly, it could offer the opportunity to apply plasmonic catalysis for lab-scale preparations and, eventually, industrial applications.

1. Fujishima, A., Honda, K. & Kikuchi, S. Photosensitized Electrolytic Oxidation on Semiconducting n-Type TiO2 Electrode. *J. Soc. Chem. Ind. Japan* **72**, 108–113 (1969).

2. Fujishima, A. & Honda, K. Electrochemical Photolysis of Water at a Semiconductor Electrode. *Nature* **238**, 37–38 (1972).

3. Ma, Y. *et al.* Titanium dioxide-based nanomaterials for photocatalytic fuel generations. *Chem. Rev.* **114**, 9987–10043 (2014).

4. Lang, X., Chen, X. & Zhao, J. Heterogeneous visible light photocatalysis for selective organic transformations. *Chem. Soc. Rev.* **43**, 473–486 (2014).

5. Fox, M. A. & Dulay, M. T. Heterogeneous Photocatalysis. *Chem. Rev.* **93**, 341–357 (1993).

6. Zhang, Y. *et al.* Synthesis of a molecularly defined single-active site heterogeneous catalyst for selective oxidation of N-heterocycles. *Nat. Commun.* **9**, 1465 (2018).

7. photocatalyst. in *IUPAC Compendium of Chemical Terminology* (IUPAC). doi:10.1351/goldbook.PT07446.

8. Reference Solar Spectral Irradiance: Air Mass 1.5. *http//rredc.Nrel.Gov/solar/spectra/am1.5/, accessed May 23, 2020*.

9. Mills, A. & Lee, S.-K. A web-based overview of semiconductor photochemistry-based current commercial applications. *J.*

Photochem. Photobiol. A Chem. **152**, 233–247 (2002).

10. Li, B., Zhang, B., Nie, S., Shao, L. & Hu, L. Optimization of plasmon-induced photocatalysis in electrospun Au/CeO 2 hybrid nanofibers for selective oxidation of benzyl alcohol. *J. Catal.* **348**, 256–264 (2017).

11. Hallett-Tapley, G. L. *et al.* Plasmon-mediated catalytic oxidation of sec-phenethyl and benzyl alcohols. *J. Phys. Chem. C* **115**, 10784–10790 (2011).

12. Kimura, K., Naya, S. I., Jin-Nouchi, Y. & Tada, H. TiO 2 crystal form-dependence of the Au/TiO 2 plasmon photocatalyst's activity. *J. Phys. Chem. C* **116**, 7111–7117 (2012).

13. Ren, X. *et al.* Recent advances in surface plasmon-driven catalytic reactions. *RSC Adv.* **7**, 31189–31203 (2017).

14. Zhang, Y. *et al.* Surface-Plasmon-Driven Hot Electron Photochemistry. *Chem. Rev.* **118**, 2927–2954 (2018).

15. Grirrane, A., Corma, A. & Garcia, H. Gold-Catalyzed Synthesis of Aromatic Azo Compounds from Anilines and Nitroaromatics. *Science (80-.).* **322**, 1661–1664 (2008).

16. Djerdj, I. *et al.* Oxygen Self-Doping in Hollandite-Type Vanadium Oxyhydroxide Nanorods. *J. Am. Chem. Soc.* **130**, 11364–11375 (2008).

17. Zhang, J. *et al.* Heterovalent doping in colloidal semiconductor nanocrystals: Cation-exchange-enabled new accesses to tuning

dopant luminescence and electronic impurities. *J. Phys. Chem. Lett.* **8**, 4943–4953 (2017).

18. Zhang, J. *et al.* Fabrication of carbon quantum dots/TiO2/Fe2O3 composites and enhancement of photocatalytic activity under visible light. *Chem. Phys. Lett.* **730**, 391–398 (2019).

19. Yu, X. *et al.* Plasmon-resonance-enhanced visible-light photocatalytic activity of Ag quantum dots/TiO 2 microspheres for methyl orange degradation. *Solid State Sci.* **80**, 1–5 (2018).

20. Zhang, Z., Wang, Z., Cao, S. W. & Xue, C. Au/Pt nanoparticle-decorated TiO2 nanofibers with plasmon-enhanced photocatalytic activities for solar-to-fuel conversion. *J. Phys. Chem. C* **117**, 25939–25947 (2013).

21. Clavero, C. Plasmon-induced hot-electron generation at nanoparticle/metal-oxide interfaces for photovoltaic and photocatalytic devices. *Nat. Photonics* **8**, 95–103 (2014).

22. Tada, H. Size, shape and interface controls in the gold nanoparticle-based plasmonic photocatalysts for solar-to-chemical transformations. *Dalt. Trans.* 2–7 (2019) doi:10.1039/C9DT00891H.

23. Hou, W. & Cronin, S. B. A review of surface plasmon resonance-enhanced photocatalysis. *Adv. Funct. Mater.* **23**, 1612–1619 (2013).

24. Primo, A., Corma, A. & García, H. Titania supported gold nanoparticles as photocatalyst. *Phys. Chem. Chem. Phys.* **13**, 886–910 (2011).

25. Zhen Ma, S. D. *Heterogeneous Gold Catalysts and Catalysis*. (Royal Society of Chemistry, 2014). doi:10.1039/9781782621645.

26. Rej, S. *et al.* Determining Plasmonic Hot Electrons and Photothermal Effects during H2 Evolution with TiN–Pt Nanohybrids. *ACS Catal.* 5261–5271 (2020) doi:10.1021/acscatal.0c00343.

27. Baffou, G. & Quidant, R. Nanoplasmonics for chemistry. *Chem. Soc. Rev.* **43**, 3898–907 (2014).

28. Wu, X., Jaatinen, E., Sarina, S. & Zhu, H. Y. Direct photocatalysis of supported metal nanostructures for organic synthesis. *J. Phys. D. Appl. Phys.* **50**, 283001 (2017).

29. Tian, Y. & Tatsuma, T. Plasmon-induced photoelectrochemistry at metal nanoparticles supported on nanoporous TiO2. *Chem. Commun.* **10**, 1810–1811 (2004).

30. Linic, S., Christopher, P. & Ingram, D. B. Plasmonic-metal nanostructures for efficient conversion of solar to chemical energy. *Nat. Mater.* **10**, 911–921 (2011).

31. Mubeen, S. *et al.* An autonomous photosynthetic device in which all charge carriers derive from surface plasmons. *Nat.*

Nanotechnol. **8**, 247–51 (2013).

32. Stratakis, M. & Garcia, H. Catalysis by supported gold nanoparticles: Beyond aerobic oxidative processes. *Chem. Rev.* **112**, 4469–4506 (2012).

33. Seemala, B. *et al.* Plasmon-Mediated Catalytic O2 Dissociation on Ag Nanostructures: Hot Electrons or Near Fields? *ACS Energy Lett.* **4**, 1803–1809 (2019).

34. Christopher, P., Xin, H. & Linic, S. Visible-light-enhanced catalytic oxidation reactions on plasmonic silver nanostructures. *Nat. Chem.* **3**, 467–472 (2011).

35. Cushing, S. K. *et al.* Tunable Nonthermal Distribution of Hot Electrons in a Semiconductor Injected from a Plasmonic Gold Nanostructure. *ACS Nano* **12**, 7117–7126 (2018).

36. Liu, J. G., Zhang, H., Link, S. & Nordlander, P. Relaxation of Plasmon-Induced Hot Carriers. *ACS Photonics* **5**, 2584–2595 (2018).

37. Smith, J. G., Faucheaux, J. A. & Jain, P. K. Plasmon resonances for solar energy harvesting: A mechanistic outlook. *Nano Today* **10**, 67–80 (2015).

38. Mukherjee, S. *et al.* Hot-electron-induced dissociation of H2 on gold nanoparticles supported on SiO2. *J. Am. Chem. Soc.* **136**, 64–67 (2014).

39. Sarina, S. *et al.* Viable photocatalysts under solar-spectrum

irradiation: Nonplasmonic metal nanoparticles. *Angew. Chemie - Int. Ed.* **53**, 2935–2940 (2014).

40. Mukherjee, S. *et al.* Hot electrons do the impossible: Plasmon-induced dissociation of H 2 on Au. *Nano Lett.* **13**, 240–247 (2013).

41. Chang, L. *et al.* Electronic Structure of the Plasmons in Metal Nanocrystals: Fundamental Limitations for the Energy Efficiency of Hot Electron Generation. *ACS Energy Lett.* **4**, 2552–2568 (2019).

42. Dubi, Y., Un, I. W. & Sivan, Y. Thermal effects - an alternative mechanism for plasmon-assisted photo-catalysis. *Chem. Sci.* **11**, 5017–5027 (2020).

43. Dubi, Y. & Sivan, Y. “Hot” electrons in metallic nanostructures non-thermal carriers or heating? *Light Sci. Appl.* **8**, 89 (2019).

44. Qiu, J. & Wei, W. D. Surface Plasmon-Mediated Photothermal Chemistry. *J. Phys. Chem. C* **118**, 20735–20749 (2014).

45. Khurgin, J. B. Fundamental limits of hot carrier injection from metal in nanoplasmonics. *Nanophotonics* **9**, 453–471 (2020).

46. Chaiseeda, K., Nishimura, S. & Ebitani, K. Gold Nanoparticles Supported on Alumina as a Catalyst for Surface Plasmon-Enhanced Selective Reductions of Nitrobenzene. *ACS Omega* **2**, 7066–7070 (2017).

47. Zhao, J. *et al.* Comparing the Contribution of Visible-Light

Irradiation, Gold Nanoparticles, and Titania Supports in Photocatalytic Nitroaromatic Coupling and Aromatic Alcohol Oxidation. *Part. Part. Syst. Charact.* **33**, 628–634 (2016).

48. Guo, X., Hao, C., Jin, G., Zhu, H.-Y. & Guo, X.-Y. Copper Nanoparticles on Graphene Support: An Efficient Photocatalyst for Coupling of Nitroaromatics in Visible Light. *Angew. Chemie Int. Ed.* **53**, 1973–1977 (2014).

49. Merino, E. Synthesis of azobenzenes: the coloured pieces of molecular materials. *Chem. Soc. Rev.* **40**, 3835 (2011).

50. Ke, X. *et al.* Selective reductions using visible light photocatalysts of supported gold nanoparticles. *Green Chem.* **15**, 236–244 (2013).

51. Zhu, H., Ke, X., Yang, X., Sarina, S. & Liu, H. Reduction of nitroaromatic compounds on supported gold nanoparticles by visible and ultraviolet light. *Angew. Chem. Int. Ed. Engl.* **49**, 9657–9661 (2010).

52. Richard, H. Gold reference catalysts now available as international standard. *World Gold Council* https://www.gold.org/news-and-events/press-releases/gold-reference-catalysts-now-available-international-standard (accessed 2020-02-03).

53. Emptage, M. R. & Carlson, R. *Design and Optimization in Organic SynthesisExperimental Design and Chemical Synthesis*.

Technometrics vol. 39 (1997).

54. Bohren, C. F. & Huffman, D. R. *Absorption and Scattering of Light by Small Particles*. (Wiley, 1998). doi:10.1002/9783527618156.

55. Baffou, G. & Quidant, R. Thermo-plasmonics: using metallic nanostructures as nano-sources of heat. *Laser Photon. Rev.* **7**, 171–187 (2013).

56. Myroshnychenko, V. *et al.* Modelling the optical response of gold nanoparticles. *Chem. Soc. Rev.* **37**, 1792–1805 (2008).

57. Link, S. & El-Sayed, M. A. Shape and size dependence of radiative, non-radiative and photothermal properties of gold nanocrystals. *Int. Rev. Phys. Chem.* **19**, 409–453 (2000).

58. Baffou, G. & Rigneault, H. Femtosecond-pulsed optical heating of gold nanoparticles. *Phys. Rev. B* **84**, 035415 (2011).

59. Maier, S. A. *Plasmonics: Fundamentals and Applications*. (Springer US, 2007). doi:10.1007/0-387-37825-1.

60. Govorov, A. O. & Richardson, H. H. Generating heat with metal nanoparticles. *Nano Today* **2**, 30–38 (2007).

61. Baffou, G. *Thermoplasmonics*. *Climate Change 2013 - The Physical Science Basis* vol. 53 (Cambridge University Press, 2017).

62. Baffou, G., Quidant, R. & García De Abajo, F. J. Nanoscale

control of optical heating in complex plasmonic systems. *ACS Nano* **4**, 709–716 (2010).

63. Haruta, M. Size- and support-dependency in the catalysis of gold. *Catal. Today* **36**, 153–166 (1997).

64. Baffou, G. *et al.* Photoinduced Heating of Nanoparticle Arrays. *ACS Nano* **7**, 6478–6488 (2013).

65. Wang, F. *et al.* Plasmonic Harvesting of Light Energy for Suzuki Coupling Reactions Plasmonic Harvesting of Light Energy for Suzuki Coupling Re- actions. (2013) doi:10.1021/ja310501y.

66. Yu, Y., Sundaresan, V. & Willets, K. A. Hot Carriers versus Thermal Effects: Resolving the Enhancement Mechanisms for Plasmon-Mediated Photoelectrochemical Reactions. *J. Phys. Chem. C* **122**, 5040–5048 (2018).

67. Keller, E. L. & Frontiera, R. R. Ultrafast Nanoscale Raman Thermometry Proves Heating Is Not a Primary Mechanism for Plasmon-Driven Photocatalysis. *ACS Nano* **12**, 5848–5855 (2018).

68. Zhang, X. *et al.* Plasmon-Enhanced Catalysis: Distinguishing Thermal and Non-Thermal Effects. *Nano Lett.* acs.nanolett.7b04776 (2018) doi:10.1021/acs.nanolett.7b04776.

69. Li, X., Everitt, H. O. & Liu, J. Confirming nonthermal plasmonic effects enhance CO2 methanation on Rh/TiO2 catalysts. *Nano*

Res. **12**, 1906–1911 (2019).

70. Jain, P. K. Taking the Heat Off of Plasmonic Chemistry. *J. Phys. Chem. C* **123**, 24347–24351 (2019).

71. Baffou, G., Bordacchini, I., Baldi, A. & Quidant, R. Simple experimental procedures to distinguish photothermal from hot-carrier processes in plasmonics. *Light Sci. Appl.* **9**, (2020).

72. Jain, P. K., Lee, K. S., El-Sayed, I. H. & El-Sayed, M. A. Calculated Absorption and Scattering Properties of Gold Nanoparticles of Different Size, Shape, and Composition: Applications in Biological Imaging and Biomedicine. *J. Phys. Chem. B* **110**, 7238–7248 (2006).

73. Christopher, P., Xin, H., Marimuthu, A. & Linic, S. Singular characteristics and unique chemical bond activation mechanisms of photocatalytic reactions on plasmonic nanostructures. *Nat. Mater.* **11**, 1044–50 (2012).

74. Sivan, Y., Un, I. W. & Dubi, Y. Thermal effects - an alternative mechanism for plasmonic-assisted photo-catalysis. 1–9 (2019).

75. Kamarudheen, R., Castellanos, G. W., Kamp, L. P. J., Clercx, H. J. H. & Baldi, A. Quantifying Photothermal and Hot Charge Carrier Effects in Plasmon-Driven Nanoparticle Syntheses. *ACS Nano* **12**, 8447–8455 (2018).

76. Zhou, L. *et al.* Response to Comment on “Quantifying hot carrier and thermal contributions in plasmonic photocatalysis”.

Science (80-.). **364**, eaaw9545 (2019).

77. Weckhuysen, B. M. & Schoonheydt, R. A. Recent progress in diffuse reflectance spectroscopy of supported metal oxide catalysts. *Catal. Today* **49**, 441–451 (1999).

78. Zhu, H., Ke, X., Yang, X., Sarina, S. & Liu, H. Reduction of Nitroaromatic Compounds on Supported Gold Nanoparticles by Visible and Ultraviolet Light. *Angew. Chemie Int. Ed.* **49**, 9657–9661 (2010).

79. Moreau, F. & Bond, G. C. Preparation and reactivation of Au/TiO2 catalysts. *Catal. Today* **122**, 260–265 (2007).

80. Ma, Z. & Dai, S. CHAPTER 1. Stabilizing Gold Nanoparticles by Solid Supports. in 1–26 (The Royal Society of Chemistry, 2014). doi:10.1039/9781782621645-00001.

81. Woodruff, P. *Modern Techniques of Surface Science*. (Cambridge University Press, 2016). doi:10.1017/CBO9781139149716.

82. Kubelka, P. New contributions to the optics of intensely light-scattering materials. *J. Opt. Soc. Am.* **38**, 448–457 (1948).

83. Köferstein, R., Jäger, L. & Ebbinghaus, S. G. Magnetic and optical investigations on LaFeO3 powders with different particle sizes and corresponding ceramics. *Solid State Ionics* **249**–**250**, 1–5 (2013).

84. Tauc, J. Optical properties and electronic structure of

amorphous Ge and Si. *Mater. Res. Bull.* **3**, 37–46 (1968).

85. Ball, D. W. Kinetics of consecutive reactions: First reaction, first-order; second reaction, zeroth-order. *J. Chem. Educ.* **75**, 917–919 (1998).

86. Connors, A. K. *Chemical kinetics: The study of reaction rates in solution*. *Inorganica Chimica Acta* vol. 180 (1990).

87. McNaught, A. D., Wilkinson, A. *IUPAC Compendium of Chemical Terminology*. (IUPAC, 2009). doi:10.1351/goldbook.

88. Emptage, M. R. & Carlson, R. Design and Optimization in Organic Synthesis. *Technometrics* **39**, 231 (1997).

89. Gałecki, A. & Burzykowski, T. *Linear Mixed-Effects Models Using R*. *Design* vol. 102 (Springer New York, 2013).

90. Frey, B. B. Generalized Linear Mixed Models. in *The SAGE Encyclopedia of Educational Research, Measurement, and Evaluation* (SAGE Publications, Inc., 2018). doi:10.4135/9781506326139.n286.

91. Akaike, H. A new look at the statistical model identification. *IEEE Trans. Automat. Contr.* **19**, 716–723 (1974).

92. Serpone, N. Relative photonic efficiencies and quantum yields in heterogeneous photocatalysis. *J. Photochem. Photobiol. A Chem.* **104**, 1–12 (1997).

93. Haruta, M. When Gold Is Not Noble: Catalysis by Nanoparticles.

Chem. Rec. **3**, 75–87 (2003).

94. Frens, G. Controlled Nucleation for the Regulation of the Particle Size in Monodisperse Gold Suspensions. *Nat. Phys. Sci.* **241**, 20–22 (1973).

95. Of, N., Of, I., With, L. & Model, P. *Fundamentals and Applications of Nano Silicon in Plasmonics and Fullerines*. (2018). doi:10.1016/B978-0-323-48057-4/00008-6.

96. Stevenson, P. C., Turkevich, J. & Hillier. a Study of the Nucleation and Growth Processes I N the Synthesis of. *Discuss. Faraday. Soc.* **11**, 55–75 (1951).

97. Govorov, A. O., Zhang, H. & Gun'Ko, Y. K. Theory of photoinjection of hot plasmonic carriers from metal nanostructures into semiconductors and surface molecules. *J. Phys. Chem. C* **117**, 16616–16631 (2013).

98. Westcott, S. L., Oldenburg, S. J., Lee, T. R. & Halas, N. J. Formation and Adsorption of Clusters of Gold Nanoparticles onto Functionalized Silica Nanoparticle Surfaces. *Langmuir* **14**, 5396–5401 (1998).

99. Stewart, M. E. *et al.* Nanostructured Plasmonic Sensors. *Chem. Rev.* **108**, 494–521 (2008).

100. Lu, H. T. Synthesis and Characterization of Amino Functionalized. **75**, 311–318 (2013).

101. Stöber, W., Fink, A. & Bohn, E. Controlled growth of

monodisperse silica spheres in the micron size range. *J. Colloid Interface Sci.* **26**, 62–69 (1968).

102. Yuan, Y., Asakura, K., Wan, H., Tsai, K. & Iwasawa, Y. Supported Gold Catalysts Derived from Gold Complexes and As-Precipitated Metal Hydroxides, Highly Active for Low-Temperature CO Oxidation. *Chem. Lett.* **25**, 755–756 (1996).

103. Ishida, T., Takamura, R., Takei, T., Akita, T. & Haruta, M. Support effects of metal oxides on gold-catalyzed one-pot N-alkylation of amine with alcohol. *Appl. Catal. A Gen.* **413**–**414**, 261–266 (2012).

104. Haruta, M., Yamada, N., Kobayashi, T. & Iijima, S. Gold catalysts prepared by coprecipitation for low-temperature oxidation of hydrogen and of carbon monoxide. *J. Catal.* **115**, 301–309 (1989).

105. Otto, K., Oja Acik, I., Krunks, M., Tõnsuaadu, K. & Mere, A. Thermal decomposition study of HAuCl4·3H2O and AgNO3 as precursors for plasmonic metal nanoparticles. *J. Therm. Anal. Calorim.* **118**, 1065–1072 (2014).

106. Cao, A., Lu, R. & Veser, G. Stabilizing metal nanoparticles for heterogeneous catalysis. *Phys. Chem. Chem. Phys.* **12**, 13499 (2010).

107. Murphy, A. B. Band-gap determination from diffuse reflectance measurements of semiconductor films, and application to

photoelectrochemical water-splitting. *Sol. Energy Mater. Sol. Cells* **91**, 1326–1337 (2007).

108. Schevciw, O. & White, W. B. The optical absorption edge of rare earth sesquisulfides and alkaline earth - rare earth sulfides. *Mater. Res. Bull.* **18**, 1059–1068 (1983).

109. Melcher, J., Feroz, S. & Bahnemann, D. Comparing photocatalytic activities of commercially available iron-doped and iron-undoped aeroxide TiO2 P25 powders. *J. Mater. Sci.* **52**, 6341–6348 (2017).

110. Eiden-Assmann, S., Widoniak, J. & Maret, G. Synthesis and characterization of hollow and non-hollow monodisperse colloidal TiO2particles. *J. Dispers. Sci. Technol.* **25**, 535–545 (2004).

111. Bagheri, S., Muhd Julkapli, N. & Bee Abd Hamid, S. Titanium dioxide as a catalyst support in heterogeneous catalysis. *Sci. World J.* **2014**, (2014).

112. Baffou, G., Polleux, J., Rigneault, H. & Monneret, S. Super-heating and micro-bubble generation around plasmonic nanoparticles under cw illumination. *J. Phys. Chem. C* **118**, 4890–4898 (2014).

113. Nikoobakht, B. & El-Sayed, M. a. Preparation and growth mechanism of gold nanorods (NRs) using seed-mediated growth method. *Chem. Mater.* **15**, 1957–1962 (2003).

114. Mehtala, J. G. *et al.* Citrate-stabilized gold nanorods. *Langmuir* **30**, 13727–13730 (2014).

115. Concentrations, R. A " Tips and Tricks " Practical Guide to the Synthesis of Gold Nanorods. (2015) doi:10.1021/acs.jpclett.5b02123.

116. Pérez-Juste, J., Pastoriza-Santos, I., Liz-Marzán, L. M. & Mulvaney, P. Gold nanorods: Synthesis, characterization and applications. *Coord. Chem. Rev.* **249**, 1870–1901 (2005).

117. Link, S. & El-Sayed, M. A. Size and temperature dependence of the plasmon absorption of colloidal gold nanoparticles. *J. Phys. Chem. B* **103**, 4212–4217 (1999).

118. Laoufi, I. *et al.* Size and Catalytic Activity of Supported Gold Nanoparticles: An in Operando Study during CO Oxidation. *J. Phys. Chem. C* **115**, 4673–4679 (2011).

119. Haruta, M. *et al.* Low-Temperature Oxidation of CO over Gold Supported on TiO2, α-Fe2O3, and Co3O4. *J. Catal.* **144**, 175–192 (1993).

120. Chorkendorff, I. & Niemantsverdriet, J. W. *Concepts of Modern Catalysis and Kinetics*. (Wiley, 2003). doi:10.1002/3527602658.

121. Roduner, E. Understanding catalysis. *Chem. Soc. Rev.* **43**, 8226–8239 (2014).

122. Liu, Q. *et al.* Plasmon-enhanced and controllable synthesis of azobenzene and hydrazobenzene using Au/TiO2 composite.

Appl. Surf. Sci. **500**, 144214 (2020).

123. Hughes, M. D. *et al.* Tunable gold catalysts for selective hydrocarbon oxidation under mild conditions. *Nature* **437**, 1132–1135 (2005).

124. Schaleger, L. L. & Long, F. A. Entropies of Activation and Mechanisms of Reactions in Solution. in *Advances in Physical Organic Chemistry* vol. 1 1–33 (1963).

125. Kabaila, P. & Ranathunga, N. On Adaptive Gauss-Hermite Quadrature for Estimation in GLMM's. in *Statistics and Data Science* (ed. Nguyen, H.) 130–139 (Springer Singapore, 2019).

126. Friedmann, D., Hakki, A., Kim, H., Choi, W. & Bahnemann, D. Heterogeneous photocatalytic organic synthesis: State-of-the-art and future perspectives. *Green Chem.* **18**, 5391–5411 (2016).

127. Palmisano, G., Augugliaro, V., Pagliaro, M. & Palmisano, L. Photocatalysis: a promising route for 21st century organic chemistry. *Chem. Commun.* 3425 (2007) doi:10.1039/b700395c.

128. The relationship between the apparent activation energy and the enthalpy of activation, for a bimolecular reaction, is given by $Ea = \Delta H + 2RT$.

129. Ma, X. C., Dai, Y., Yu, L. & Huang, B. B. Energy transfer in plasmonic photocatalytic composites. *Light Sci. Appl.* **5**, (2016).

130. Transmission dip probe. https://www.avantes.com/products/fiber-optics/item/253-transmission-dip-probe.

131. Tahir, M. H., Mubashir, T., Shah, T.-U.-H. & Mahmood, A. Impact of electron-withdrawing and electron-donating substituents on the electrochemical and charge transport properties of indacenodithiophene-based small molecule acceptors for organic solar cells. *J. Phys. Org. Chem.* **32**, e3909 (2019).

132. Plutschack, M. B., Pieber, B., Gilmore, K. & Seeberger, P. H. The Hitchhiker's Guide to Flow Chemistry â¥. *Chem. Rev.* **117**, 11796–11893 (2017).

133. Cambié, D., Bottecchia, C., Straathof, N. J. W., Hessel, V. & Noël, T. Applications of Continuous-Flow Photochemistry in Organic Synthesis, Material Science, and Water Treatment. *Chem. Rev.* **116**, 10276–10341 (2016).

134. Loubière, K., Oelgemöller, M., Aillet, T., Dechy-Cabaret, O. & Prat, L. Continuous-flow photochemistry: A need for chemical engineering. *Chem. Eng. Process. Process Intensif.* **104**, 120–132 (2016).

135. Tao, S., Yang, M., Chen, H., Zhao, S. & Chen, G. Continuous Synthesis of Ag/AgCl/ZnO Composites Using Flow Chemistry and Photocatalytic Application. *Ind. Eng. Chem. Res.* **57**, 3263–3273 (2018).

136. Sui, J., Yan, J., Liu, D., Wang, K. & Luo, G. Continuous Synthesis of Nanocrystals via Flow Chemistry Technology. *Small* **16**, 1–23 (2020).